Thomas Govaert

Analysis and prediction of the influence of high frequency combustion instabilities on heat transfer in a sub-scale LOX/H2 rocket thrust chamber

TU Delft

DLR Deutsches Zentrum für Luft- und Raumfahrt

Master Thesis

Analysis and prediction of the influence of high frequency combustion instabilities on heat transfer in a sub-scale LOX/H2 rocket thrust chamber

by

Thomas Govaert

Thesis work was completed at the German Aerospace Center, Institute of Space Propulsion in partial fulfilment of the requirements for the degree of Master of Science in Aerospace Engineering at the Delft University of Technology.

To be defended publicly on Thursday June 27, 2019 at 09:00 AM.

Supervisors:
Ir. B.T.C. Zandbergen (TU Delft)
Dr. J. Hardi (DLR)
Ir. W. Armbruster (DLR)

Thesis committee:
Dr. G.A. Bohlin (TU Delft)
Ir. B.T.C. Zandbergen (TU Delft)
Prof. Dr. E.K.A. Gill (TU Delft)
Ir. W. Armbruster (DLR)

DLR document number: DLR-LA-RAK-HF-RP-101
An electronic version of this thesis is available at http://repository.tudelft.nl/

Cover page: Launch of Ariane 5, credit: Arianespace

TU Delft

DLR Deutsches Zentrum für Luft- und Raumfahrt

Preface

This thesis has been completed as part of the requirements for obtaining a Master of Science degree in Aerospace Engineering at the Delft University of Technology. In this report the main results and findings of the research completed are summarised, while having the opportunity to contribute to the existing body of knowledge of the scientific community.

This report will be especially relevant for researchers and rocket engineers interested in calculating heat fluxes in rocket engines and predicting their changes due to the presence of high frequency combustion instabilities.

I would like to personally thank my supervisors Ir. Wolfgang Armbruster for always being available with invaluable insight and advice, Dr. Justin Hardi for being able to supervise and help from his unique position of experienced rocket engineer, and Ir. Barry Zandbergen for his critical and elaborate revision, invaluable inputs on my work and to ensure academic value of the thesis work.

Finally, I would also like to express thanks to my colleagues and personal friends who were with me in the office, having been of help whenever practical, theoretical or personal problems arose.

List of Figures

List of Tables

List of Symbols and Abbreviations

Symbol	Meaning	Unit
A	Amplitude of acoustic pressure oscillations	bar
$A_{inj_{H_2}}$	Hydrogen injector cross sectional area	m^2
$A_{inj_{O_2}}$	Oxygen injector cross sectional area	m^2
c_p	Specific heat	J/(kg·K)
dh	Change in specific enthalpy	J/kg
D_c	Combustion chamber diameter	m
err	Absolute error	-
$err_{\%}$	Relative error	%
$f_{m,n,p}$	Eigenmode frequency	Hz
h	Specific enthalpy	J/kg
H	Enthalpy	J
h_c	Heat transfer coefficient	W/(K m^2)
h_{H_2}	Specific enthalpy of injected hydrogen	J/kg
h_{in}	Specific enthalpy of coolant water at inlet	J/kg
h_{out}	Specific enthalpy of coolant water at outlet	J/kg
h_{O_2}	Specific enthalpy of injected oxygen	J/kg
H_x	Enthalpy of element x	J
J	Momentum flux ratio	-
$J_n(x)$	Bessel function of the first kind	-
k	Gas thermal conductivity	W/K
L_c	Combustion chamber length	m
L/D	LOX core length normalised with D_{inj}	-
m	Radial overtone number	-
m_x	Mass of element x	-
Ma	Mach number of combustion gases	-
Mw	Molecular weight	g/mol
$\dot{m}$	Mass rate	kg/s
$\dot{m}_{inj}$	Total mass rate of injected propellants	kg/s
$\dot{m}_{inj_{H_2}}$	Mass rate of injected oxygen	kg/s
$\dot{m}_{inj_{O_2}}$	Mass rate of injected hydrogen	kg/s
n	Tangential overtone number	-
p	Pressure	bar
P_c	Chamber pressure	bar
P_{in}	Coolant water inlet pressure	bar
P_{out}	Coolant water outlet pressure	bar
Pr	Prandtl number	-
p'	Acoustic pressure	bar
p'_{RMS}	RMS of the acoustic pressure	bar
$p'_{\%}$	Relative acoustic pressure	%
q	Longitudinal overtone number	-
$\dot{Q}$	Heat flow rate	W
$\dot{Q}_c$	Convective heat flow	W/m^2
$\dot{Q}_{diff}$	Change in integrated heat flux	W
$\dot{q}_{initial}$	Initial heat flux in heat flux profile	W/m^2
$\dot{Q}_{int}$	Integrated heat flux	W
$\dot{Q}_{pred}$	Integrated heat flux predicted	W
r	Recovery factor	-
r_θ	Radial component of radial coordinate system	-
S	Surface area	m^2
t	Time	s
T	Temperature	K
$T_{ambient}$	Ambient temperature	K

Symbol	Meaning	Unit
T_x	Temperature of mass element x	K
T_{gw}	Gas temperature at the wall	K
T_{g0}	Hot gas medium temperature	K
T_{H_2}	Inlet temperature of hydrogen	K
T_{in}	Coolant water inlet temperature	K
T_{out}	Coolant water outlet temperature	K
T_{O_2}	Inlet temperature of oxygen	K
T_w	Combustor wall temperature	K
T_∞	Free stream temperature	K
V	Local gas velocity	m/s
V_c	Speed of sound	m/s
V_{H_2}	Hydrogen injection velocity	m/s
V_{O_2}	Oxygen injection velocity	m/s
V'	Acoustic velocities	m/s
x_{H_2}	Mole fraction of H_2	-
x_{H_2O}	Mole fraction of H_2O	-
α_{mn}	Roots of n$^t h$ order Bessel function divided by pi	-
γ	Specific heat ratio	-
δ	Angular offset	rad
ϵ	Emissivity	-
θ	Angular component of radial coordinate system	rad
κ	Thermal conductivity	W/(m·K)
μ_{am}	Dynamic viscosity of gas evaluated at T_{am}	m^2/s
μ_{dyn}	Dynamic viscosity of gas	Pa·s
μ_{kin}	Kinematic viscosity of gas	m^2/s
μ_0	Kinematic viscosity of gas at combustion temperature	m^2/s
ρ	Local gas density	kg/m^3
ρ_{am}	Gas density evaluated at T_{am}	kg/m^3
ρ_{g0}	Gas density at combustion temperature	kg/m^3
ρ_{H_2}	Hydrogen injection density	kg/m^3
ρ_{O_2}	Oxygen injection density	kg/m^3
ρ'	Free stream gas density	kg/m^3
ϕ_{ij}	Coefficient for mixed viscosity	-
ω	Angular frequency	Rad/s

Abbreviation	Meaning
BKD	Brennkammer D (english: combustion chamber D)
BKH	Brennkammer H (english: combustion chamber H)
CEA	NASA's Chemical Equilibrium with Applications
CFD	Computational Fluid Dynamics
DLR	Deutsches Zentrum für Luft- und Raumfahrt
FEM	Finite Element Method
HF	High frequency
HG	Hot combustion gases
L	Longitudinal Acoustic Mode
LF	Low frequency
H2	Hydrogen
LOX	Liquid oxygen
NASA	National Aeronautics and Space Administration
NIST	National Institute of Standards and Technology
PSD	Power Spectral Density
R	Radial Acoustic Mode
ROF	Ratio of oxidiser to fuel
ROF$_{stoichiometric}$	Stoiciometric ratio of oxidiser to fuel
T	Tangential Acoustic Mode

Contents

Abstract

The German Aerospace Centre (DLR) has in the past years been performing test runs with their experimental sub-scale combustion chambers to measure and investigate the effects of unstable combustion. Some of these investigations are focused on the heat flux to the chamber walls, changes in which can cause a significant shift in chamber wall strength and even melting, and can thus lead to structural failures. As a continuation of research regarding this phenomenon, the DLR combustion chamber version D (BKD) is used to investigate changes in heat flux, and its test data have been made available for this research. Using the test data, finding a relation between measured steady state heat flux and controlled chamber conditions became feasible, and changes in heat flux related to combustion instabilities can be identified. However, although these changes in heat flux are often observed and are described in literature as a known effect of combustion instabilities, there are currently no validated explanations as to why these effects take place. In an effort to provide this explanation, the results of a previously completed investigation regarding the DLR combustion chamber version H (BKH) are evaluated, as they allowed determination of a relation between combustion length and magnitudes of acoustic pressure oscillations. In this research, the results obtained for combustion length are converted to a model regarding varying heat flux profiles and modified as to implement them for BKD. Finally, the model predicted increases in heat flux during time periods when increases are observed experimentally, showing agreement with the experimental data. Besides this, a conversion in the model allowed reconstruction of a localised heat flux profile, which showed an increase in local heat flux near the injector face plate. This matches effects described in literature and observed in the experimental set-up after a test run with combustion instabilities. With this validation of the model, the theory developed and tested in this thesis work could prove a significant advancement in the understanding of effects of combustion chamber instabilities and their impact on the engine integrity and performance.

1 Introduction

This thesis work is completed at the German Aerospace Center (DLR) in cooperation with the Delft University of Technology (TUDelft) and focusses on high frequency combustion instabilities on sub-scale rocket engines. In particular, an attempt is made at explaining the often reported increase in heat flux to the combustor walls during periods of unstable combustion. This explanation is based on experimental results reported for the DLR experimental combustion chamber version H (BKH), which suggest a change in flame structure due to the presence of acoustic pressure oscillations in the combustor. To apply these observations to this research, the change in flame structure is extrapolated to a change in axial heat flux distribution along the chamber length. With this methodology, predicted changes in heat flux can be compared with experimentally determined heat fluxes in the DLR experimental combustion chamber version D (BKD). This experimental comparison serves the purpose of validating results of BKH investigations and to be the first to provide a validated explanation for changing heat fluxes during periods of high frequency combustion instabilities.

1.1 Relevance of Work

During early liquid rocket engine developments, the excitement of combustion instabilities in the combustion chamber was one of the main reasons for engine failure. Combustion instabilities are generally defined in literature as pressure oscillations in the combustion chamber of which the magnitude reaches amplitudes of more than 5% of the chamber pressure [1–3]. Pressure oscillations of lower magnitude are generally accepted as their effects on mechanical and thermal loads will be minimal and thus within design margins. Another interesting property of combustion instabilities is that, although chamber pressure oscillations are always present, during stable combustion the frequency spectrum will be essentially continuous with some minor peaks, while for unstable combustion the oscillations have large concentrations of vibrational energy at certain frequencies. For thermo-acoustic instabilities, these frequencies correspond to acoustic chamber Eigenfrequencies which are related to Eigenmodes [1]. Due to the lack of understanding of these instabilities, the only known solution to combustion instabilities was to change the geometrical parameters in the chamber and iterate this procedure until the instabilities were no longer encountered for the needed operating conditions [4, 5]. Past 1940, the US space programme recognised the importance of better understanding this phenomenon, as increased pressure loading, fatigue due to cyclic loads and especially increased thermal loads seriously endanger the engine and rocket structure. For this reason, the US space effort was focused on performing over 2000 engine tests under Wernher von Braun to find stable engine configurations for the Saturn V rocket [6, 7]. As a result of these iterative tests, a stable engine configuration was derived, although in most cases still no deeper understanding of causes of combustion instabilities was generated [8]. This large scale test campaign was the first of its kind and introduced the space community to a new field of research. This field is still not fully understood and, due to the cost heavy nature of full-scale combustion chamber tests, limited to a few specialised institutes such as the DLR Institute of Space Propulsion in Lampoldshausen, Germany [9].

A continued investigation into combustion instabilities with different chamber geometries and propellant combinations was made by the National Aeronautics and Space Administration (NASA) [10–12] and other institutions such as Rocketdyne that was responsible for the F-1 engine that flew on the Saturn V rocket [2], Pennsylvania State University [13] and Princeton University [4] in the US. These investigations resulted in a deeper understanding of general combustion instabilities while focusing on finding out what causes them and also making some first attempts at characterising the effects of combustion instabilities on engine performance. Although some causes have been successfully identified such as coupling of Eigenmodes and some effects have been defined such as changes in heat transfer to the combustor walls, there has been no successful investigation regarding the causes of these effects. Besides the American effort, there has also been a European effort such as that of the DLR Institute of Space Propulsion, Toulouse University and Cerfacs to numerically simulate combustion behaviour [14, 15] and to try to simulate the internal flame dynamics and how it reacts to imposed instabilities. Besides numerical solving, also test campaigns have been performed by the DLR Institute of Space Propulsion [16–20] as part of an experimental investigation of combustion instabilities. The aim of these experiments is generating more knowledge and to increase predictive capabilities regarding causes and effects of these instabilities while centred around a series of experimental sub-scale combustion chambers operating under conditions similar to upper stage rocket engines such as the European Vinci engine and power levels similar to smaller upper stage engines such as the Aestus engine [19, 21]. One of these chambers,

BKD was originally designed to investigate the effects of heat transfer using regenerative cooling [19], although its configuration also allowed for obtaining data regarding the total heat flow to the combustion chamber walls and its increase due to instabilities. The research performed in this thesis work is based on this combustion chamber and is an attempt at being the first to validate proposed causes of observed effects in heat transfer during combustion instabilities.

1.2 Research Plan

To focus this research into what is relevant, a clear research goal is stated. Besides, this goal is elaborated and translated into a research question which will be answered in this thesis work. Finally, the research question is split into multiple sub-questions, to facilitate answering and to further narrow down the research into what is relevant.

The goal of this research project is to enable prediction of heat flux changes based on magnitudes of high frequency combustion instabilities.

Elaborating on the research goal, it should be stressed that it is not part of the main objective to make quantitative heat flux predictions, rather their change with respect to unstable time periods relative to stable time periods with the same chamber inputs. These chamber inputs are defined in Section 3.1, being chamber pressure, reactants inlet temperature and oxidiser to fuel ratio, while the quantitative values of these inputs are available as measurement data. This goal consists of two parts: first being able to define or predict what heat flow would be present in the form of an integrated heat flux over the chamber area during stable combustion and secondly being able to predict a relative change in integrated heat flux dependent on the magnitude of instabilities as defined later. The degree of accuracy necessary to achieve meaningful results for this steady state heat flow prediction is deemed around 5%, based on preliminary results and sensor accuracies, meaning any error should be less than 5%. In case the degree of accuracy is lower, it will become hard to differentiate between mispredictions in heat flow and genuine deviations in the experimental data. The degree of accuracy necessary for meaningful results of integrated heat flux change is hard to define, as this type of research has not been completed before and this would be the first research in which heat flux changes are explained in an experimentally validated model. For this reason, any valid indication of heat flow changes with this model is considered acceptable. It should be mentioned that no numerical computational fluid dynamics solving is done, as this would be too computationally heavy to solve for all cases considered while results might still not help achieving the research goal. The combustion instabilities considered for this research are high frequency transverse pressure oscillations as further explained and defined in Section 2. It is important to stress this, since different instability modes have different forcing effects on the gas in the chamber [19]. Lastly, it should be noted that although effects described in this thesis work most likely also apply to different injector types such as Pintle or impinging injectors due to improved mixing, the results of this analysis are obtained for combustion chambers with shear coaxial injection while no experimental data is available with different injector types. For this reason, the described effects cannot be validated for other injector types. Different combustion chamber elements such as film cooling are not considered, as this data is not available.

The main research question that can be posed to achieve the proposed research goal is as follows:

How can a change in integrated heat flux due to combustion instabilities be explained?

Answering this question means completing the project objective, although this cannot be done in a simple and straightforward manner, considering the scope of this question. For this reason, some sub-questions can be considered while effectively splitting up the main question into segments which can be answered separately.

1. How can changes in integrated heat flux due to combustion instabilities be determined?

- How can integrated heat flux, as expected in stable combustion, be predicted for given input conditions when the measured integrated heat flux is unstable?
- How generally applicable can an integrated heat flux prediction model for steady conditions be made?
- How accurate are the predicted stable and measured integrated heat flux?

2. How can changes in integrated heat flux due to combustion instabilities be explained?

- How can phenomena that effect heat flux in combustion chambers be modelled in an empirical way?
- When modelled, how does this model correspond with the measured data?
- Can this model be based on theories developed through BKH?

3. How can a model be validated for a more general case?

- How do the predicted heat flux changes compare to reported observations in literature?
- How do the predicted heat flux changes compare to experimentally determined changes in heat flux in BKD?

1.3 Thesis Outline

The structure of this thesis work is organised in a manner which follows the thought process of the work completed. The first step in this research project is a background study, ensuring a knowledge basis that helps answering the research question and sub-questions. An elaboration on required background is shown in Section 2, presenting an introduction in combustion instability theory, heat fluxes in rocket combustors, a more focused elaboration on the 1T instability mode and a presentation of the results regarding BKH on combustion instabilities and its effects on the flame. In Section 3, the experimental set-up is elaborated on, as to create a deeper understanding of the methods applied for this research and its limitations. In Section 4, the first research question is tackled. Here, it is explained how a prediction for integrated heat flux at stable operating conditions is made when the measurements take place during unstable conditions. With this prediction for representative integrated heat flux and the observed experimental heat flux, an estimate is made for change in heat flux during periods of unstable combustion. Connected to this, in Section 5 the second research question is tackled. Here, a model is derived from the BKH results that can predict the change in heat flux due to unstable combustion, independent from experimental data of BKD. In Section 6, both a sensitivity analysis is completed on the made assumptions throughout the whole project, as to obtain a view on the significance of any results. Next, the last research question is answered in Section 7, as the models are combined to obtain the experimental results that form the conclusion of this thesis work. Finally a conclusion is presented in Section 8 and recommendations for future work are presented in Section 9, to enable continuation of this work. These recommendations are given a separate chapter, as to keep a clear overview.

2 Background

In this section a background is given on elements relevant and necessary to the research performed for this master thesis. First of all, in Section 2.1 a definition of combustion instabilities is made, in particular high frequency combustion instabilities, as this phenomenon is central to the research performed. Next, the principle of heat flux to the combustor walls, its theoretical estimation and its known relation with combustion instabilities is elaborated on in Section 2.2, being complementary to knowledge on combustion instabilities themselves. When the broader basis is established, the 1T instability mode, being a particular mode of high frequency combustion instabilities that has been identified in the experimental set-up is elaborated in Section 2.3. Lastly, based on understanding and identification of the 1T mode, an analogy is made between this research and other research regarding effects this 1T mode has on combustion processes in Section 2.4, being the basis for a first model regarding prediction of heat fluxes during combustion instabilities.

2.1 High Frequency Combustion Instabilities

Combustion in liquid rocket engines is typically a turbulent process with large Reynolds numbers of Re $> 10^5$, with turbulent flow defined as having Re $> 10^4$. Related to this, pressure fluctuations occur due to local differences in oxidiser to fuel ratio or varying gas densities within the flow [1, 3, 22]. These oscillations are almost always present and thus as long as their magnitude remains below 5% of the static chamber pressure, the combustion is generally considered to be smooth. When the amplitudes grow larger, there is said to be rough combustion and when the oscillatory energy of the gases is focused on one or more specific frequencies, there are combustion instabilities. Different ranges of these frequencies are related to the different causes of the pressure fluctuations. The different types, their causes and frequency ranges are presented in Table 1, of which the high frequency combustion instabilities are considered in this research. Although chugging is generally considered to be understood and can be mitigated by increasing the injection pressure drop, the high frequency combustion instabilities are still not fully understood and are thus hard to be predicted. Although these frequency range definitions seem straightforward, the processes behind these combustion instabilities are not and even today a thorough understanding of this phenomena is still not achieved. [1, 6, 23]

Table 1: Different types of combustion instability. [1]

Denotation	Frequency Range (Hz)	Often related to
Low frequency (chugging)	10-400	The propellant feed system or the dynamics of the vehicle assembly
Intermediate frequency (buzzing)	400-1000	Mechanical vibration of the engine assembly or flow instabilities
High frequency (screeching)	1000+	The combustion process (pressure waves) and chamber acoustics

At the start of liquid-propellant rocket engine development, combustion instabilities were still an unfamiliar concept, considering the relative novelty of this field of science. Many unexpected engine failures can be traced back to this lack of knowledge, while inability to predict combustion instability behaviour ensured the requirement for extensive testing and subsequent engine modifications before an engine could be determined reliable enough for its wanted purpose. The main practical problems related to combustion instabilities are that it can introduce high vibrational loads of different frequencies to the engine and rocket structure, the mechanical loads on the chamber structure are increased significantly through a periodically increased chamber pressure (in the test case considered for this research the chamber pressure is increased by up to 40 % of the stable operational chamber pressure) and increased heat loads can be imposed on the structure. Especially the increased heat loads are often responsible for engine failure, as they can cause a local or overall reduction in material strength and material melting in the walls or injector plates as was reported during testing of RD-0110 engines for the Soyuz and Molniya launch vehicles [13]. In addition, wall melting can cause exposure of the cooling channels, which in turn causes failure of the entire cooling system through a snowball effect. These issues can cause serious damage to any rocket or engine structure and often lead to mission failure, causing one third of liquid rocket engine

failures in the early Russian space effort (1957-1969) [23]. For these reasons, the presence of combustion instabilities in flight-optimised rocket engines is unwanted.

In an early effort to gain deeper understanding of combustion instabilities and to broaden capabilities to predict and prevent instabilities, was the test campaign preceding the American Apollo missions. In this test campaign, over 2000 engine tests were performed specifically to investigate combustion instabilities under Wernher von Braun for the F1 rocket engine that flew the Apollo astronauts to the Moon, as depicted in Figure 1a. [5, 7, 24]

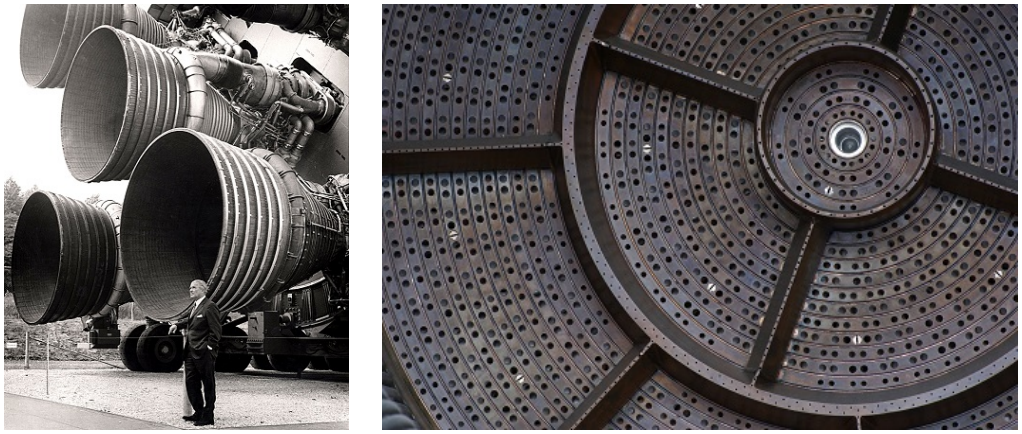

(a) F1 engines. [5]

(b) F1 injector plate baffles. [25]

Figure 1: F1 rocket engine.

With this extensive experimental research, some important lessons were learnt. The first lesson is that different instability modes can be identified based on their centre frequency, while each mode has different mechanisms and causes as mentioned before. Secondly, some pragmatic remedies to the instabilities were identified, such as adding baffles to the injector face plate, illustrated in Figure 1b and adding damping cavities around the main combustor that can dampen pressure oscillations with specific frequencies. Lastly, it was found that combustion instabilities can be excited externally, besides their self-excitation during combustion. This allowed for systematic investigations in combustors with different geometries and is still being applied today as a method of combustion chamber design validation. [17]

Closer to what is currently state of the art, a deeper, although still incomplete understanding has been achieved regarding combustion instabilities. First of all, the existence of acoustic fields in the chamber has been identified through testing of combustion chambers with strategically placed acoustic pressure sensors [19,26,27] and numerical simulations [14,15]. These acoustic fields represent the different high frequency pressure waves present in the hot gases during combustion and are part of the chamber acoustics, also known as chamber modes. These chamber modes can be theoretically modelled as standing waves in a cylindrical chamber, through which their corresponding mode frequencies can be roughly estimated and subsequently identified during experimental tests. The equation used for estimating these frequencies is given as Equation 1, where V_c is the speed of sound in the gas mixture, m, n and q represent respectively the radial, tangential and longitudinal modes, D_c and L_c are the combustion chamber diameter and length as illustrated in Figure 18, α_{mn} are roots of the n^{th} order Bessel function of the first kind divided by pi and Ma is the Mach number in the gas mixture. Gas parameters needed for this equation can be calculated for different stages of combustion with programs such as NASA's Chemical Equilibrium with Applications (CEA) program [28] or calculated using advanced Computational Fluid Dynamics (CFD) solutions. For clarity, the Bessel functions of the first kind, denoted by $J_n(x)$, are defined as the solutions to the Bessel differential equation given as Equation 2 [29].

$$f_{m,n,q} = \frac{V_c}{2}\sqrt{\left(\frac{2\alpha_{mn}}{D_c}\right)^2 (1 - Ma^2) + \left(\frac{q}{L_c}\right)^2 (1 - Ma^2)^2} \tag{1}$$

$$x^2 \frac{d^2y}{dx^2} + x\frac{dy}{dx} + \left(x^2 - n^2\right) y = 0 \tag{2}$$

Values for m, n and q are positive integers and correspond to the different modes that can not only be purely longitudinal (L), radial (R) or tangential (T), but also any combination of these (TR, TL, LR), while each mode has multiple overtones possible (1T mode, 2T mode, ...) as illustrated in Figure 2. For example, if m and n are 1 and q is 0, the described mode is the LR mode. Based on this information, Equation 1 and with known geometry of the main chamber cylinder, the Eigenfrequencies of all modes can be approximately calculated [19]. These estimations can then be compared to a pressure spectrogram and so the acoustic modes that are present can be identified.

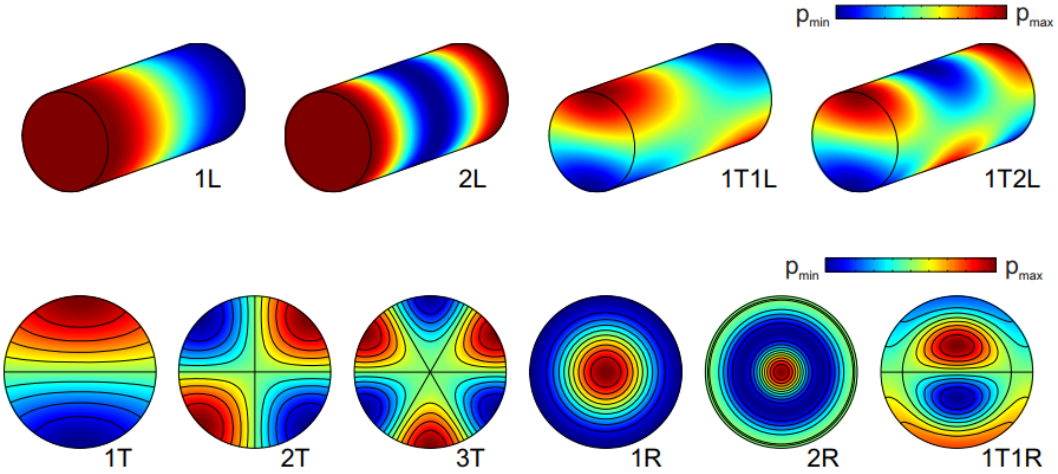

Figure 2: Acoustic modes in a cylinder. [19, 24]

Lastly, also the Eigenmodes of the injector elements can be of relevance, as frequencies related to these have been observed in pressure spectrograms while there have been suggestions that these injector element eigenfrequencies can have an effect on the excitement of combustion instabilities [17, 20]. This is the case when chamber Eigenfrequencies coincide with acoustic Eigenfrequencies of the injectors. This coupling mechanism is known as injection-coupled instabilities and has been the focus of recent investigations although predictive capabilities regarding this phenomenon are not yet reliable due to difficulties in theoretically predicting the injector Eigenfrequencies [10, 17, 20]. Besides approximate methods using acoustic theory, it has also become possible in recent years to perform numerical solving using some Finite Element Methods (FEM), often giving more accurate results [14, 15, 30]. However, although this method can be more reliable and offers more possibilities (for example calculation of Eigenmodes in more complex geometries), it requires expertise in simulations and extensive computational processing. This method is not applied in this research as it is not part of the research goal outlined for this thesis work. Lastly, there are currently no methods known to predict the amplitude of pressure oscillations during combustion instabilities, although there are new tools that can estimate whether a load point is stable or unstable [31] while also the frequencies can be estimated using methods presented above.

2.2 Heat Flux to the Chamber Walls

As this master thesis work is regarding changes in heat flux to the combustor walls with high frequency combustion instabilities, it is crucial to have at least a basic understanding of heat fluxes. In this section, an elaboration is made on the theoretical estimation of convective heat fluxes and on the experimental measurement of heat flux in the combustor. In the theoretical predictions radiative heat fluxes are assumed negligible, as the radiative heat fluxes can amount to no more than 5% of total heat flux for smaller combustors such as BKD, due to the relatively large surface area to volume ratio of thin cylinders [1]. Whether this assumption is valid can be evaluated when the calculated values are compared with experimental data and show consistent underprediction or not. Lastly, in literature it has been described how combustion instabilities can have an effect on heat flux to the combustor walls, this is also elaborated.

2.2.1 Theoretical Heat Flux Calculation

In order to calculate the theoretical convective heat flow $\dot{q}_c$ from the hot combustion gases to the combustor walls, Equation 3 can be used. In this equation a convective heat transfer coefficient, h_c, is defined which is dependent on the hot gas properties and can be estimated using fluid and gas heat transfer theory. To obtain the heat transfer per unit wall surface area S in the chamber, the heat transfer coefficient is multiplied by the difference in hot gas medium temperature, T_{g0} and the wall temperature of the chamber, T_w.

$$\dot{Q}_c = h_c \cdot (T_{g0} - T_w) \cdot S \tag{3}$$

In order to calculate the heat transfer coefficient, some theoretical equations exist which can be applied in different contexts and geometries [1, 3, 32]. The equation applying to the cylindrical combustor walls is given as Equation 4, although a different equation would apply to calculate the theoretical convective heat flux to the nozzle wall [1]. In this equation, ρ is the local gas density, v is the local gas velocity, D_c is the chamber diameter, Pr is the Prandtl number, κ is the thermal conductivity of the gas and μ_{dyn} is the dynamic viscosity. Note that the coefficient 0.0225 is recommended for use in the cylinderical section of combustion chambers, while for nozzles with thin boundary layers a value of 0.026 has been experimentally determined [33].

$$h_c = 0.0225 \cdot \frac{(\rho v)^{0.8}}{D_c^{0.2}} Pr^{0.33} \frac{\kappa}{{\mu_{dyn}}^{0.8}} \tag{4}$$

What is most interesting about Equation 4 is its general applicability, meaning it does not apply to one combustor only or one test condition and could thus be applied on all test runs without preceding calibration. The main downside of this purely theoretical equation however is that, due to the turbulent and complex nature of combustion, the theoretical equation is oversimplifying. For example, it does not take into account any effects due to a thermal boundary layer near the combustor walls and thus does not accurately represent experimental conditions [1, 3].

2.2.2 Bartz Heat Flux Prediction

As a response to the lack of agreement between experimental values and theoretical values, Bartz combined the two into a semi-empirical relation to obtain an equation that remains generally applicable, but would better predict measurements [1]. One of the resulting equations, proposed by Bartz as a simple alternative to more complex computations is Equation 5, as given for a gas flow in a cylindrical chamber [33].

$$h_c = \frac{0.0225}{D_c^{0.2}} \cdot \left(\frac{c_p {\mu_{dyn}}^{0.2}}{Pr^{0.6}} \right) \cdot (\rho' v)^{0.8} \cdot \left(\frac{\rho_{am}}{\rho'} \right) \cdot \left(\frac{\mu_{am}}{\mu_0} \right)^{0.2} \tag{5}$$

Here, ρ' is the free stream gas density, c_p is the specific heat of the hot gas at constant pressure, the subscript 0 represents the parameter as evaluated at combustion or stagnation temperature and the subscript am represents the parameter as evaluated at arithmatic mean gas temperature, meaning the average value of hot gas temperature and hot gas at the chamber wall. This difference in temperature between hot gases in the bulk flow and at the chamber wall indicates that this Bartz equation takes into account effects due to the thermal boundary layer, unlike the purely theoretical equation. The principle of a thermal boundary layer is illustrated in Figure 3, where temperature experiences a decrease close to the chamber wall. As no measurements are present of gas conditions after injection in the bulk or in the wall, these have to be estimated.

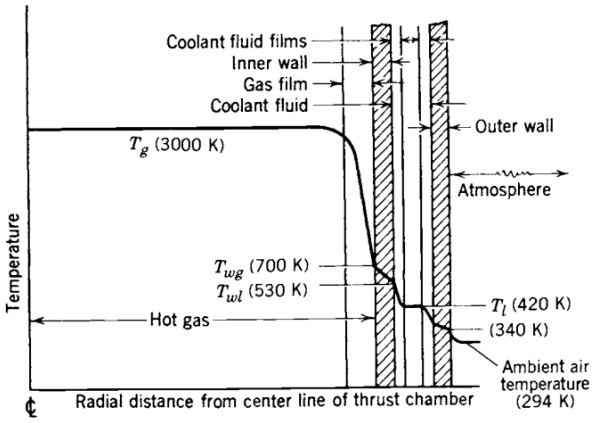

Figure 3: Thermal boundary layer effects. [1]

2.2.3 Experimental Heat Flux Calculation

In order to experimentally determine the heat flux into the combustor walls, a method making use of the enthalpy properties of chamber coolant (in pyhsics: calorimetric method) is the most used way of calculating the heat flux at each point in time. This works with combustion chambers that are cooled using a liquid cooling circuit, in which the liquid properties are measured at outlet and inlet of the cooling circuit.

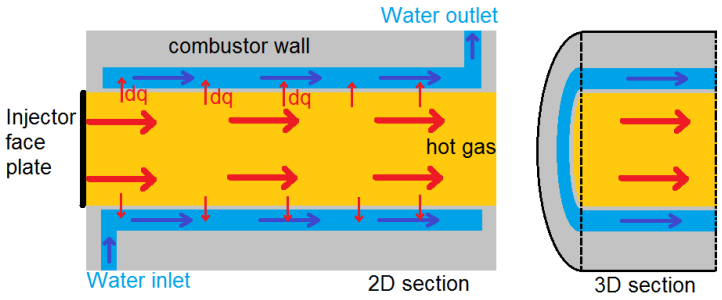

Figure 4: Calorimetric measurement set-up.

As depicted in Figure 4, the coolant water is pumped into a cylindrical section of a combustor. Measurements of water temperature T, water pressure P and mass flow rate $\dot{m}$ at the entrance and exit allow for calculation of its specific enthalpy h through the National Institute of Standards and Technology (NIST) REFPROP program [34]. Total enthalpy H can be calculated at both points through Equation 6 and thus also the change in enthalpy while water travels over the length of the cooled section as Equation 7. This measuring principle, when combined with a known mass flow rate of the coolant water allows for equating change in water enthalpy over each unit length of the combustor to the local heat flux dq into the combustor walls. Integrating these local heat fluxes over the total combustor length and thus its entire interior surface area results in the instantaneous mean heat flow, equal to the integrated heat flux $\dot{Q}_{int}$, as demonstrated in Equation 8. This integrated heat flux is in fact the total heat flow into the chamber walls for that section. In order to equal the heat flux into the chamber walls to the change in enthalpy of the water however, it is assumed that the chamber walls are sufficiently (over)cooled so that no heat is lost to the outside world through radiation or convection from the outer chamber wall to the outside world. This method can be applied with one cooling circuit to obtain the integrated heat flux, which is a heat flow, over the entire combustion chamber, giving information about the mean heat flux during combustion [19]. However, it can also be applied discretely through implementing many distinct cooled cylindrical sections which together make up the combustor walls, allowing measurements of a discretised but local heat flux per section [11, 12].

$$H_x = h(T_x, P_x) \cdot m_x \tag{6}$$

$$dH = m \cdot (h(T_2, P_2) - h(T_1, P_2)) \tag{7}$$

$$\dot{Q}_{int} = \frac{dH_{tot}}{dt} = \dot{m} \cdot (h(T_2, P_2) - h(T_1, P_1))) \tag{8}$$

Besides this method, there are others available. For example, with the inverse method, it is possible to estimate the temperature gradient in the combustor walls using multiple thermocouples closely spaced but inserted at different depths in the walls. With this temperature gradient, a known difference in thermocouple depth and knowing the thermal conductivity of the wall material, allows for calculating the heat flux at that location in the wall. This method allows for accurate calculation of the heat fluxes, but also allows for easier discretisation of heat fluxes as distributed over the chamber length as there is no practical limit as to how many thermocouples can be inserted. However, this experimental set-up was not present during the BKD test campaign of which the data are used in this research and thus this method is not pursued.

2.2.4 Known Effects of Combustion Instabilities

In literature, different effects of combustion instabilities on measured heat fluxes into the combustor walls have been mentioned, although not always being consistent. The reader should note the difference between localised heat fluxes and integrated heat fluxes, while not all relevant literature specifies which is described. In order to stress the importance of this differentiation, first a short elaboration is given.

As described in Section 2.2.3, integrated heat fluxes are effectively the integrated heat flux over the chamber length into the chamber walls, returning a mean heat flow value over the entire combustor cylindrical surface area. When an increase in integrated heat flux is described, this does not mean the heat fluxes are raised in all locations in the chamber or that anything is known about the heat flux profile throughout the chamber length, rather it could be that there is an increase in one section of the chamber that is large enough to raise the average heat flux to the observed value. Localised heat fluxes on the other hand are heat fluxes over a small axial segment of the chamber, while not considering heat fluxes over any other section of the chamber. This means that the overall heat flow is not necessarily affected by much even when the localised heat fluxes are raised by a large amount.

As an example, an investigation done by Harrje indicates an increased heat flux of factor 3 for longitudinal instability modes and factor 4 for transverse instability modes, although not distinguishing between localised or integrated heat flux [4]. There is also mention of a non-linearity in flux increase with respect to combustion instability magnitudes. This means that, although an instability with larger amplitude will cause a higher increase in heat flux, the ratio of heat flux increase to instability magnitude will be lower than for small amplitude combustion instabilities [4].

Also Sutton reported that different effects exist depending what instability modes are present, the transverse modes being the most destructive [1]. However, in this report no direct increases in observed heat flux are reported, rather an increase in heat transfer rates is reported of 4 to 10 times the stable heat transfer rate. It is also mentioned that destructive effects on the combustor such as metal melting and wall burn-throughs are sometimes observed within less than 1 second of combustion instability initiation, meaning a small lag in time can appear. An illustration of observed metal melting is shown in Figure 5, where the green flame indicates the presence of copper in the combustion process, likely coming from the copper shell on the inner combustor wall or the injector face plate [35].

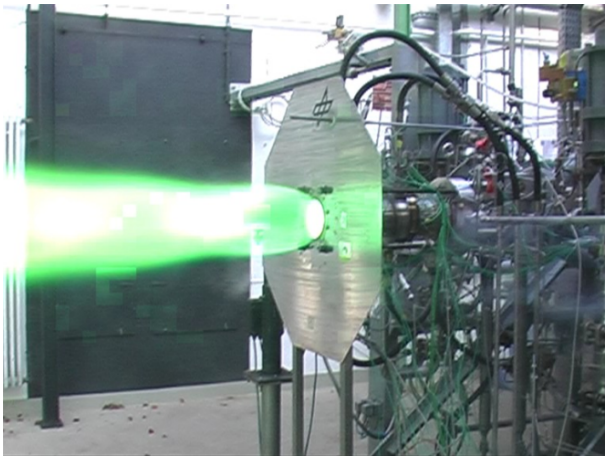

Figure 5: Green flame indicating copper in the combustion process. [35]

Different investigations resulted in different conclusions, where Dranovsky found heat flux increases up to a factor 6 for high frequency combustion instabilities [23]. In this case, the research is focused on the heat flux near a pressure transducer close to the injector face plate, thus not speaking about the integrated heat flux. It becomes more clear that this increase involves the localised heat flux near the injector face plate.

This localised increase of heat flux is confirmed by direct experimental results shown in research of Hulka [11]. These results are presented in Figure 6 and it can be seen that large increases in local heat flux occur near the injector face plate, up to a factor of 8. The overall integrated heat flux also increases, but not by this large factor, being closer to a 40% increase. It can be noted that heat flux near the end of the combustion increases only by a small amount, probably due to thermal boundary layer destruction.

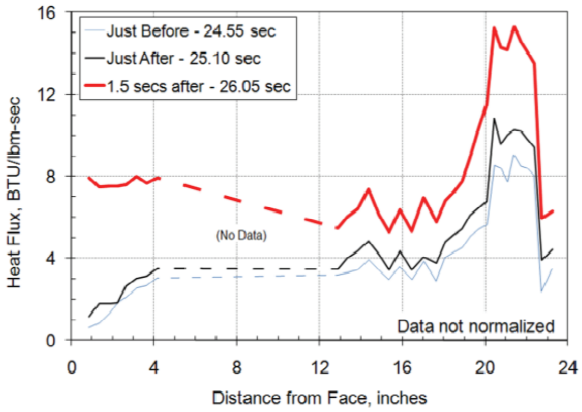

Figure 6: Experimentally determined change in heat flux profile with HF instabilities. [11]

Confirming the experimental data of Hulka and the reported observations of Dranovsky, it has been observed that for some experimental combustion chambers of the DLR in Lampoldshausen, significant damage has been inflicted at or close to the injector face plate related to an excess of generated heat. This damage comes in the form of a molten injector plate or partially molten injector baffles as shown in Figure 7. Usually the injector faceplate is not designed for handling heat fluxes, as the injection of cold propellants combined with a delayed combustion cause heat loads to be much smaller near the injector plate with respect to the cylindrical chamber after complete combustion. This phenomenon can be seen in experimental results shown in Figure 6. Since for these experimental runs the rest of the combustor walls are relatively undamaged and show no significant signs of melting, also this is a strong indicator for a localised increase in heat flux near the injector face plate in the event of high frequency combustion instabilities. There is currently no validated explanation for these localised increases in heat flux.

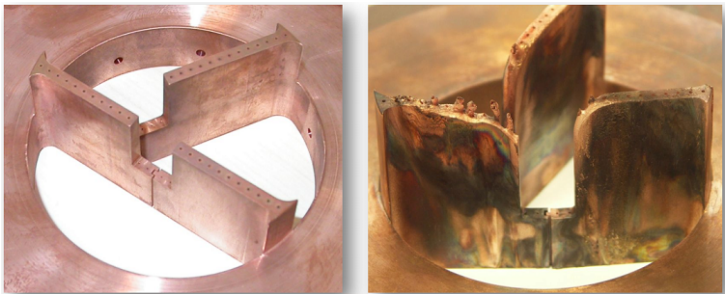

Figure 7: Damaged injector baffle after HF combustion instabilities. [35]

Finally, very little information is available on mechanisms that could explain these increases in heat flux (both local and integrated), ranging from theories regarding destruction of thermal boundary layers to theories regarding increased convective heat flux due to large transverse velocities over the combustor walls to theories regarding increased LOX core break-up and early mixing and thus increased heat release near the injector face plate of the combustor [36, 37]. There has been previous research concerning the thermal boundary layer destruction, although the results of this research showed that predicted increases in heat flux were orders of magnitude smaller than experimentally observed increases in heat flux and thus destruction of the thermal boundary layer could not be validated as one of the main causes of observed changes in heat flux [37]. It should be noted that this research was tested in pulse combustors however, the results of which might differ from rocket engine combustors due to the difference in scale of the pressure oscillations (BKD: 30bar, pulse combustors 0.23 bar) and the difference in oscillation frequencies (BKD: around 10kHz, pulse combustors 45-200Hz). [38–40]

2.3 1T Instability Mode

As will be elaborated in Section 5.1.2, the transverse modes are those observed in BKD. Besides, in rocket combustors, the transverse acoustic modes have been identified as being the most destructive, known to cause the largest increases in heat transfer [4]. Compared to longitudinal modes which have been observed to cause an increase in heat flux of factor 3, the tangential modes have been observed to cause an increase of factor 4 [4]. Note that structural weakening and melting due to increased heat transfer is the main cause for engine destruction due to the presence of combustion instabilities [23]. For this reason, it is considered of importance to elaborate on the most common version of the transverse mode: the 1T mode, being the first transverse mode.

2.3.1 1T Pressure Fields

First of all, the 1T mode is a purely transverse mode, meaning the pressure oscillations can be fully described by a time dependent pressure distribution of a cross section of the combustion chamber. This pressure distribution, also known as pressure field, is given as Equation 9 [19]. In this equation, J_1 is a first order Bessel function, α_{01} is the 1T wavenumber associated with the chamber and determined experimentally for BKD [19], r_θ is the radial coordinate in the applied polar coordinate system, D_c is the chamber diameter, θ is the angular coordinate, ω is the angular frequency of the wave that is equal to the Eigenfrequency of the mode, t is the time at which the pressure field is evaluated and δ is the angular offset at zero time of the pressure field with respect to the chosen axis system.

$$p'(\theta, r_\theta, t) = J_1\left(\frac{2\pi\alpha_{01}r_\theta}{D_c}\right) \cdot (M \cdot cos(\theta + \omega t + \delta) + N \cdot cos(\theta - \omega t - \delta)) \tag{9}$$

The values of N and M in this equation are determined based on the peak amplitudes in the acoustic pressure field, although in our case it is easier to normalise this equation and scale the resulting pressure field with the measured amplitudes rather than determine them through derivation. In the normalised case, to determine values of M and N it is easiest to interpret the pressure field as the sum of two rotating elements. When N is zero the pressure field will have one rotating element, meaning the field itself will

be a rotating field of constant magnitude as described by Equation 10. When N and M are both equal, the pressure field will consist of two counter-rotating elements which interfere with each other to create a standing non-rotating pressure field as described by Equation 11. Finally, to obtain the correct pressure amplitudes, both equations must be scaled with $A(t)/J_1(\pi\alpha_{01})$ which is the time dependent amplitude of the pressure oscillations divided by a first order Bessel function [19]. Note that in both equations the angular offset of the pressure field, δ, is neglected since the coordinate system can be chosen arbitrarily and is thus chosen to coincide with the initial orientation of the pressure field.

$$p'(\theta, r_\theta, t) = \frac{A(t)}{J_1(\pi\alpha_{01})} J_1\left(\frac{2\pi\alpha_{01} r_\theta}{D_c}\right) \cdot cos(\theta + \omega t) \tag{10}$$

$$p'(\theta, r_\theta, t) = \frac{A(t)}{J_1(\pi\alpha_{01})} J_1\left(\frac{2\pi\alpha_{01} r_\theta}{D_c}\right) \cdot cos(\theta) cos(\omega t) \tag{11}$$

The standing and rotating 1T pressure fields have been constructed and are visualised in Figures 8 and 9. [19]

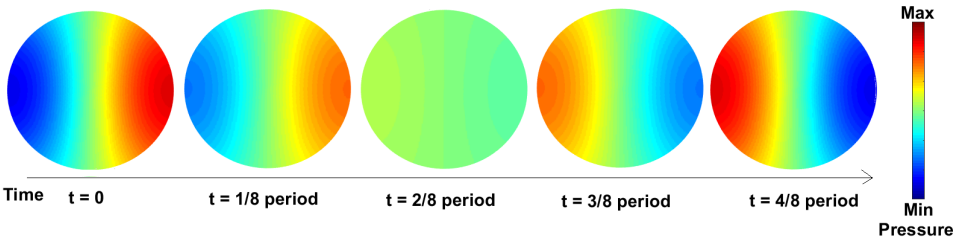

Figure 8: Changing pressure field over time for a standing wave.

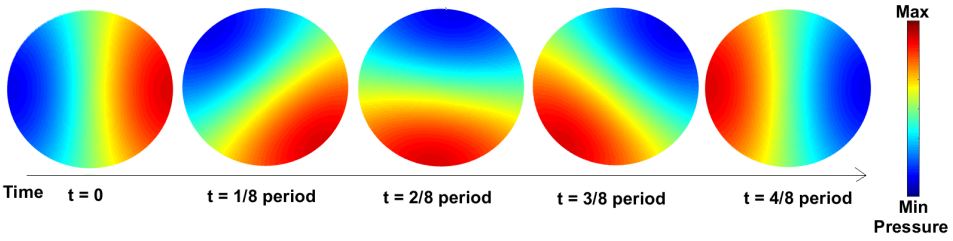

Figure 9: Changing pressure field over time for a rotating wave.

2.3.2 1T Transverse Velocity Fields

Induced by the pressure distribution in the gases across a chamber cross section, the gases will flow from one side of the cross section to the other. These transverse velocities have different magnitudes and a phase shift of $\frac{\pi}{2}$ with respect to the gradient of the pressure field. These fields are considered of importance, while although the pressure fields represent the combustion instabilities in their most fundamental form, the velocity fields represent the momentum of the gases as induced by these combustion instabilities. It is not the pressure distributions, but the movements of the gas that have a direct effect on the injected liquid oxygen (LOX) core by disturbing the core and thus potentially inducing earlier jet break-up and propellant combustion. Although transverse flows of the hot gases are unknown to have a direct effect on the measured heat flux in combustor walls, an early LOX core break-up and earlier completed combustion causes an earlier achieved final hot gas temperature and with that a larger integrated heat flux in the chamber walls. To investigate the transverse velocities and velocity fields corresponding to pressure fields, a more theoretical approach is adopted. In mathematical notation, the velocity field corresponding to a pressure field can be derived from Euler's equation written as Equation 12 and represented as Equation 13. [19, 41]

$$\rho \frac{\delta V(\theta, r_\theta, t)}{\delta t} = -\nabla p'(\theta, r_\theta, t) \tag{12}$$

$$V(\theta, r_\theta, t) = -\frac{1}{\rho} \int \nabla p'(\theta, r_\theta, t) dt \tag{13}$$

To find solutions for the velocity field, the radial and angular components can be derived analytically to find a velocity vector at each point in the cross section. The amplitude of each vector would be the absolute magnitude of the transverse velocity. The formulation of the velocity field for standing waves is given in Equations 14, 15 and 16. Derivations for these analytical solutions are given in Appendix B.

$$V_\theta(\theta, r_\theta, t) = \frac{A(t)}{r_\theta 2\pi f \rho} \cdot \frac{1}{J_1(\pi \alpha_{01})} \cdot J_1\left(\frac{2\pi \alpha_{01} r_\theta}{D_c}\right) \cdot sin(\theta) sin(\omega t) \tag{14}$$

$$V_{r_\theta}(\theta, r_\theta, t) = -\frac{A(t)}{2\pi f \rho} \cdot \frac{1}{J_1(\pi \alpha_{01})} \cdot \frac{dJ_1\left(\frac{2\pi \alpha_{01} r_\theta}{D_c}\right)}{dr_\theta} \cdot cos(\theta) sin(\omega t) \tag{15}$$

$$V(\theta, r_\theta, t) = \sqrt{V_{r_\theta}(\theta, r_\theta, t)^2 + V_\theta(\theta, r_\theta, t)^2} \tag{16}$$

The formulation of velocity fields for rotating waves is given in Equations 17, 18 and 19.

$$V_\theta(\theta, r_\theta, t) = \frac{A(t)}{r_\theta 2\pi f \rho} \cdot \frac{1}{J_1(\pi \alpha_{01})} \cdot J_1\left(\frac{2\pi \alpha_{01} r_\theta}{D_c}\right) \cdot cos(\theta + \omega t) \tag{17}$$

$$V_{r_\theta}(\theta, r_\theta, t) = -\frac{A(t)}{2\pi f \rho} \cdot \frac{1}{J_1(\pi \alpha_{01})} \cdot \frac{dJ_1\left(\frac{2\pi \alpha_{01} r_\theta}{D_c}\right)}{dr_\theta} \cdot sin(\theta + \omega t) \tag{18}$$

$$V(\theta, r_\theta, t) = \sqrt{V_{r_\theta}(\theta, r_\theta, t)^2 + V_\theta(\theta, r_\theta, t)^2} \tag{19}$$

The resulting velocity fields are presented in Figures 10 for standing waves and 11 for rotating waves, where some velocity vectors are indicated as arrows in the velocity field.

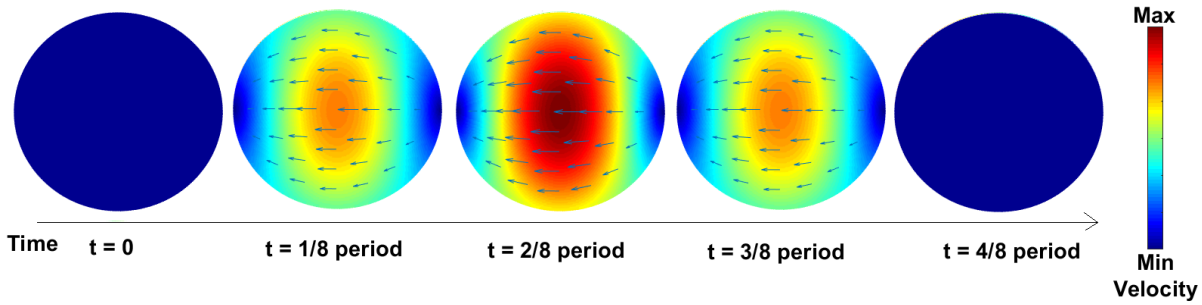

Figure 10: Changing transverse velocity field over time for a standing wave.

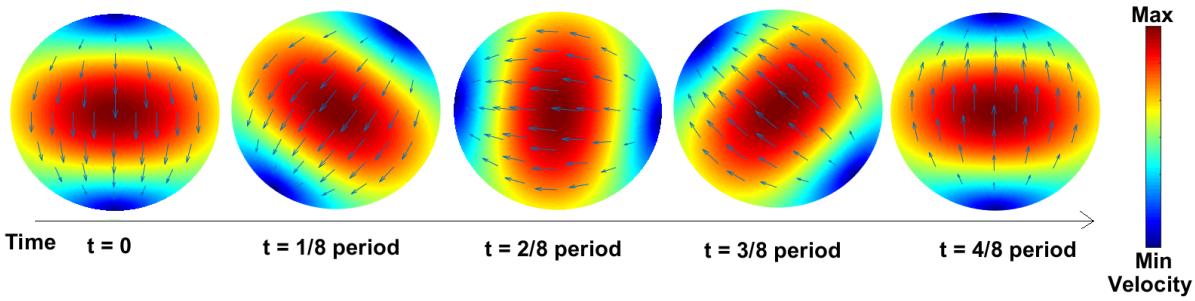

Figure 11: Changing transverse velocity field over time for a rotating wave.

2.3.3 Standing versus Rotating waves in BKD

In order to determine which pressure fields apply to the BKD test runs, an analysis has been performed that compares acoustic pressure data to find a relation between 1T state (spinning/rotating versus standing) and its amplitude and frequency [26]. In this research, the easiest parameters to compare are acoustic pressure amplitudes and the wave state and thus frequency is not further looked at. The combined analysis is presented in Figure 12.

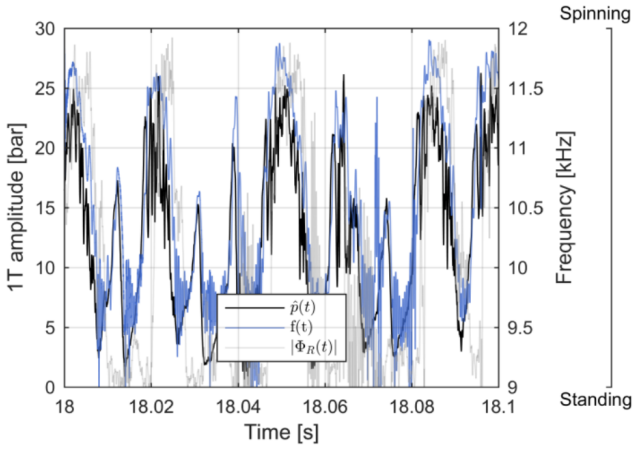

Figure 12: Analysis on rotating versus standing 1T modes in BKD. [26]

In this graph the grey line indicates the wave state of either spinning or standing and the black line indicates amplitude of the 1T mode pressure oscillations. It can be observed that the blue line follows the black line closely, although sometimes with a small time lag of less than 5ms. This observation indicates that when acoustic pressure oscillations have relatively high magnitudes, there is a high chance for spinning waves to be present, while the opposite is true for acoustic pressure oscillations with relatively low magnitudes. Although a more thorough analysis could result in an experimental relation, it is chosen to continue with a more rough but simpler approximation by defining threshold amplitudes between spinning and standing waves. The chosen thresholds are that 1T amplitudes lower than 10 bar consistently correspond to standing waves, while 1T amplitudes larger than 15 bar consistently correspond to rotating waves This approximation can be used in this research to identify the relevant pressure fields and transverse velocity fields. A recommendation for future work is that this phenomenon is investigated more in depth to establish a clear and validated set of criteria that would allow for determination of the wave type and its transition.

2.4 1T Instability Mode Investigation in BKH

In order to better understand the 1T instability mode and possible effects on the combustion process, a combustion chamber designated BKH was designed and tested by the DLR Institute of Space Propulsion. Although no further investigations are made in this research regarding BKH and no new results are created regarding phenomena observed in BKH, it is deemed that results from earlier investigations are of importance for this investigation and thus elaborated on below. In this section, the performed investigations are summarised, along with these results. Unique to this design is that it includes an optical access into the chamber and a sirene wheel with the function of a resonator to externally excite the chambers acoustic modes through inducing pressure oscillations. What is most interesting and what makes this research relevant however, is that the experimental rocket combustor uses the same propellant combination as BKD of LOX and H2, injected through five shear coaxial injection elements without recess. For this reason, results from the BKH investigation are expected to also apply to BKD, although the difference in momentum flux ratio will have an effect on break-up characteristics of the injected LOX that will have to be taken into account. Lastly, it should be noted that BKD chamber pressures remain in the range which allows LOX to remain supercritical, while for BKH this is not always the case and must be taken into account in further investigations. [16–18, 42, 43]

2.4.1 Design of BKH

The BKH combustor has a chamber volume that is 240mm long, 200mm high and 50mm wide, not including the nozzles. This shape has been adopted to have precise and defined chamber acoustic modes (only transverse and longitudinal modes), with a known orientation. In cylindrical chambers, the nodal line of the 1T mode is not constant can change in time in the form of a rotating wave [16]. The chamber pressure ranges from 40bar to 60bar and the LOX injector diameter is 3.5mm, being close to the BKD LOX injector diameter of 3.6. To allow for optical access into the combustion process, a window is integrated into the side of the combustor wall as shown in Figure 13. This optical access allows for shadowgraph imaging and OH* imaging which can be used for determination of flame properties such as the length of an intact LOX core as measured from the injection face plate, during both stable and unstable combustion. [18, 43]

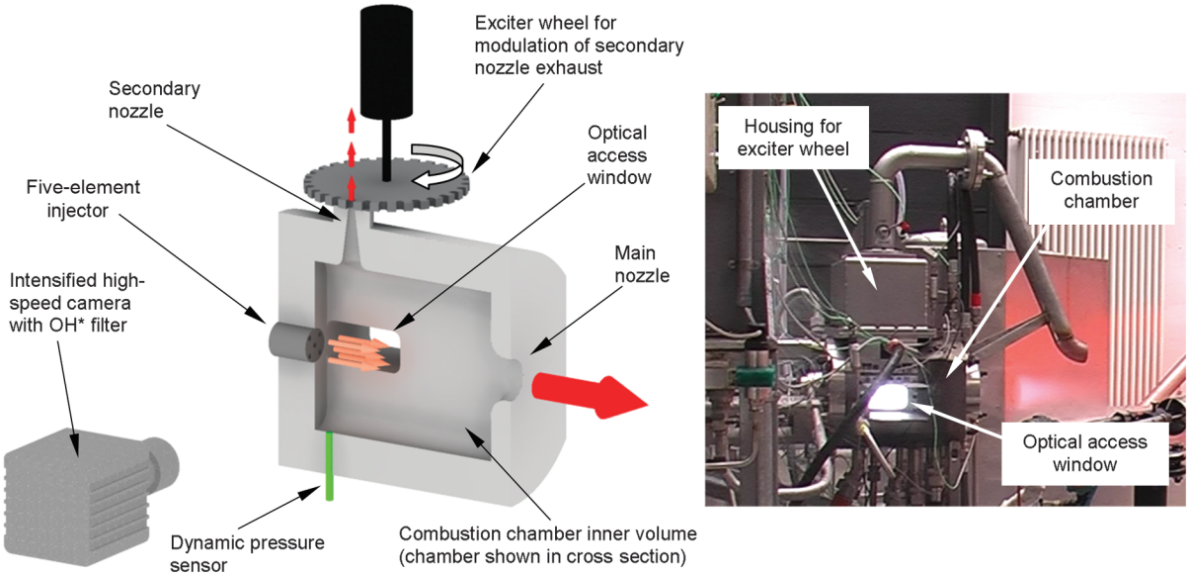

Figure 13: Conceptual illustration of BKH and a photograph taken during operation. [17]

The resonator or exciter wheel, also indicated in Figure 13, goes together with and is placed on a secondary nozzle exhaust and allows for modulation of a secondary exhaust flow [17]. The modulation is dependent on the angular velocity at which the wheel spins, so that wheel notches open and close the nozzle with a certain frequency, being the excitation frequency. Allowing this periodic nozzle flow will induce transverse pressure oscillations in the chamber and when its frequency matches an acoustic

mode of the chamber, the amplitude of these excitations will resonate and grow in amplitude until the combustion can be considered unstable. This principle is called induced or externally excited combustion instabilities and can be observed in the experimental data of BKH tests as illustrated in Figure 14. [18]

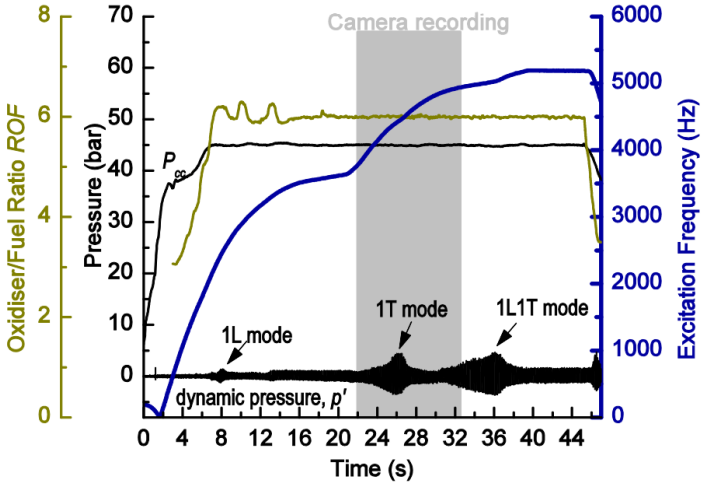

Figure 14: Test sequence of BKH. [18]

2.4.2 BKH Results

Through shadowgraphing the combustion process it was possible in previous research to distinguish the length at which the injected LOX core has fully broken up and the LOX combusts with the injected hydrogen [17]. For this LOX core analysis, only the center injector is considered as this represents a flight-engine more closely due to the injected propellants being fully surrounded by other jets. This LOX core length is a good indication for 'combustion length', being the distance the gases travel in the chamber before they are fully mixed and reach full combustion temperatures. A full explanation on methods applied for identifying this core length can be found in [44].

Repeated experiments and frame-by-frame LOX core length identification allowed for relating this LOX core length to the magnitude of pressure oscillations at an excited 1T mode frequency of the chamber. Interestingly, the effect of these pressure oscillations was found to be relatively strong, where an increased pressure oscillation magnitude causes a decreased LOX core length, as shown in Figures 15 and 16. In these figures the LOX core length is normalised with respect to the injector diameter, which for BKH is 3.5mm. [18, 43]

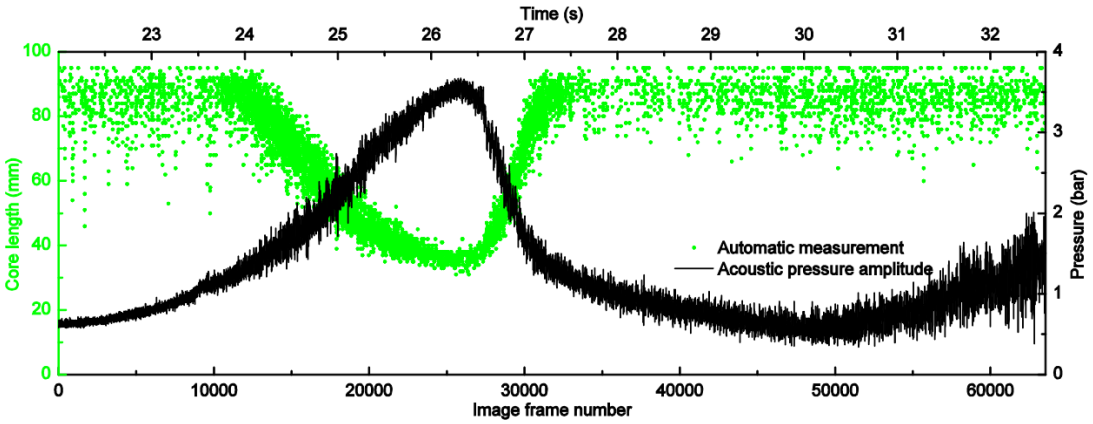

Figure 15: LOX core length measurements with measured acoustic pressure amplitudes. [18]

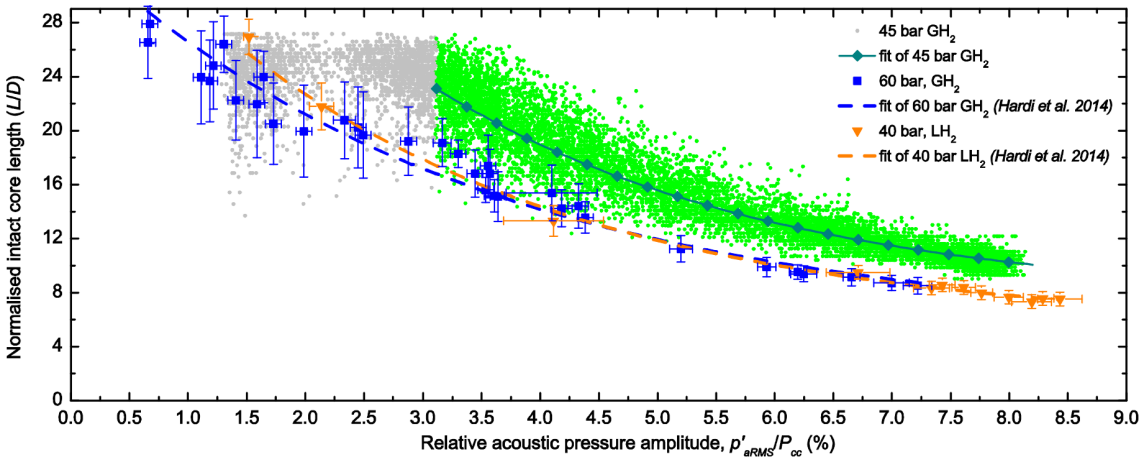

Figure 16: LOX core length measurements over measured acoustic pressure amplitudes. [18]

This reduction in LOX core length has been investigated and quantified and a relation between relative acoustic pressure amplitudes, $\frac{p'_{\%}}{P_c}$ further designated $p'_{\%}$ for clarity, and the normalised LOX core length $\frac{L}{D}$ has been established for a range of operating conditions. This semi-empirical relationship has been reported as Equation 20, while the coefficients a, b and c have been determined based on fitting with experimental data. [16–18]

$$\frac{L}{D}_{BKH} = a - b \cdot c^{p'_{\%}} \tag{20}$$

However, test runs with different operating conditions have shown to return different coefficients and thus no single relation applies to a combustion chamber. Results from all relevant BKH test runs along with their operating conditions are listed in Table 2 and will be implemented in this research with a modification as to apply to BKD in Section 5.1 where they are also visually represented in Figure 36. While BKH momentum flux ratios are around 6 and those of BKD range between 5 and 50, mostly remaining in the lower ranges, the relationships are expected to hold for BKD. Although this is currently the best estimate for shortened LOX cores for BKD, it is recommended that when methods become available to estimate the LOX core shortening for BKD which can be verified to BKD data, they are implemented instead. Note that the hydrogen is injected under supercritical conditions, just as for BKD, although a differentiation is to be made between the injected hydrogen based on their injection temperatures. The principle behind this differentiation is explained in Section 2.5, but in some test runs (1-7), the hydrogen has gaslike properties due to its relatively high temperature, while in others (8-11) the hydrogen has liquidlike properties. Between these runs it is expected that the found results regarding instabilities show differences in LOX core length relations. It is chosen not to differentiate between injection velocities as injection velocities are known to have only small effects on combustion lengths compared to injection temperatures, thus the found relation is kept as simple as possible [45]. [16–18]

A limit to this research is the positioning of the optical access window, where a LOX core with L/D more than 28 occurs out of the field-of-view of the optical equipment and will thus not be recorded in a correct way. This can be seen in the experimental data points presented and indicated in grey in Figure 15, as all data is cut off at magnitudes of L/D being more than 28, while they also seem to be converging to a slightly lower value when relative acoustic pressure amplitudes reach magnitudes below 3. This does not necessarily correspond to the maximum LOX core length. Because of this limit however, it is hard to approximate LOX core lengths during stable combustion with an experimental relation.

To find a solution to this limit in experimental results, other literature has been looked at which describes the break-up of LOX cores in combustors [36, 46]. This resulted in a model which predicts the L/D at stable combustion and implements that value as a cut-off point in the exponential function that calculates the L/D for larger acoustic pressure amplitudes. At this point effects due to acoustic pressure oscillations no longer add to the effects of already existing turbulence. As an example, the L/D corresponding to zero relative acoustic pressure amplitudes will be identical to those at relative acoustic pressure amplitudes

Table 2: List of relevant BKH test runs and their LOX core length fits. [36]

Test	1	2	3	4	5	6	7
T_{H2}(K)	288	302	306	305	296	299	300
Hydrogen state	Gaslike	Gaslike	Gaslike	Gaslike	Gaslike	Gaslike	Gaslike
P_c(bar)	60	59	48	48	42	51	45
Coefficient a	6	6.3	5	5	6	3	6
Coefficient b	-29.55	-30.08	-44.01	-45.05	-40	-33.27	-43.68
Coefficient c	0.7	0.65	0.65	0.65	0.76	0.79	0.74
R^2 value of fit	0.907	0.833	0.937	0.974	0.505	0.895	0.911

Test	8	9	10
T_{H2}(K)	62-75	64	71
Hydrogen state	Liquidlike	Liquidlike	Liquidlike
P_c(bar)	44	41	40
Coefficient a	5.29	6.5	7.98
Coefficient b	-34.97	-40	-41.31
Coefficient c	0.71	0.69	0.67
R^2 value of fit	0.898	0.37	0.783

of 1 or 1.5 % of the chamber pressure, but will start decreasing with the exponential curve found for BKH when the relative acoustic pressures reach higher amplitudes.

This LOX core length investigation is interesting for the BKD investigation due to its analogue with a heat flux profile through the chamber, where the local heat flux increases in magnitude with increased mixing and thus combustion of the injected gases. Before reaching a final, more or less constant local heat flux magnitude, a sinusoidal local heat flux profile is expected where increasing distance from the injector face plate corresponds to a higher local heat flux. The distance at which this final value is reached is thought to be directly related to the LOX core length, as a fully mixed and combusted gas will not generate any extra heat, rather in this stage it is expected to convect a constant heat flux to the walls.

2.5 Supercritical Conditions

To describe supercritical conditions, first the critical point of a substance must be elaborated upon. This is the point for any substance, where the liquid and vapour phases flow into each other with no distinct phase change. Beyond the critical point, the substance is denoted a 'supercritical fluid' as it is no longer a gas nor a liquid. Practically, this means that, as the pressure approaches the critical point, the energy required to vaporise and the surface tension both decrease to zero as indicated in Figure 17 for oxygen, showing a phase diagram overlayed with the specific heat capacity at each point. As can be seen in Figure 17, also the heat capacity of the fluid shows extreme variation. These changes in fluid characteristics can have large effects on rocket propellants if injected under such conditions, changing jet break-up and mixing mechanisms. [16]

For hydrogen and oxygen, the critical point is defined as shown in Table 3. In BKH and BKD and other modern rocket engines, hydrogen is injected in a supercritical state with pressures and temperatures being larger than those at the critical point [16]. For oxygen, the injection temperature is often slightly below the critical temperature, as is the case for BKD as shown in Table 4. However, in this case, the extreme chamber temperatures quickly raise the oxygen temperature above its critical point and thus ensure a supercritical oxygen which will mix with the already supercritical oxygen as indicated in Figure 17. This injection method is denoted 'transcritical injection' [16].

Table 3: Supercritical point for hydrogen and oxygen. [16, 34]

Parameter	Oxygen	Hydrogen
Critical temperature	154.59K	32.97K
Critical pressure	50.43bar	12.93bar

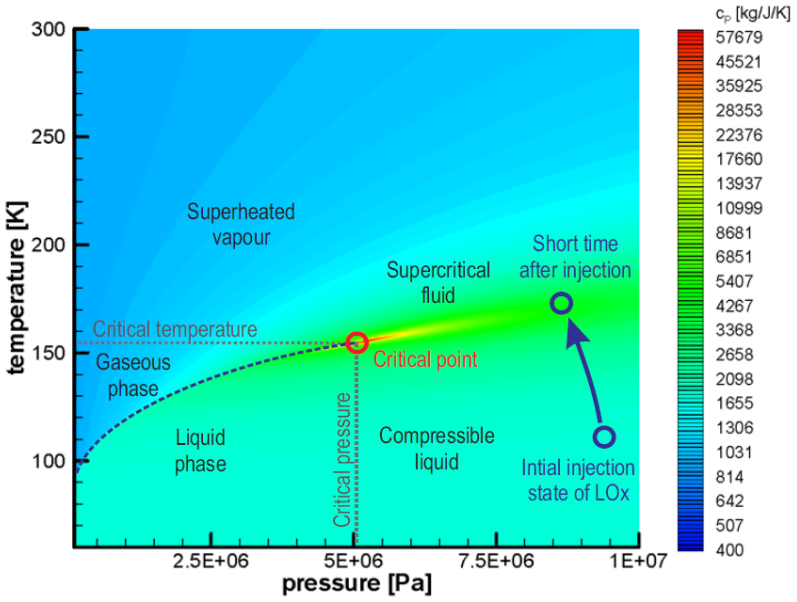

Figure 17: Phase diagram of oxygen, indicating the sub- and supercritical regions. [16, 47]

However, although the chamber pressure for the given BKD test runs is consistently above 50bar, meaning the injected oxygen is in a supercritical state, the same is not always true for BKH. For BKH, some test runs are operating with chamber pressures below 50bar, meaning after injection the LOX jet will not necessarily be in a supercritical state regardless of its temperature. For this reason, it is considered necessary to make a differentiation between test cases based on their chamber pressures being above and under the critical pressure, before making a comparison between these two experimental set-ups.

Lastly, although there is no distinct phase change in a supercritical fluid, there are still significant changes in density with varying temperature, especially near the critical temperature. For this reason, BKD test cases were made with temperatures both relatively close to the critical temperature (ranging around 45K for most of the test runs) and temperatures ranging significantly higher than the critical temperature (ranging around 95K for most of the test runs) to investigate both types. As the injected hydrogen will have significantly different density properties, the test cases with the lower temperatures are denoted to have hydrogen with 'liquidlike' properties due to its relatively high density and those with the higher temperature ranges as 'gaslike' due to its relatively low density, although neither are liquid nor gas. For the rest of this report, the gaslike cases are indicated with 'G' and their test number, while the liquidlike cases are denoted 'L' with their test number.

3 Experimental Setup

In order to understand the research performed for this master thesis work, a short description of the experimental rocket engine used has been made. In this rocket engine two segments are considered of importance, being the combustion chamber and its injector face plate which includes the injector elements. Also measurement of the chamber conditions is considered as experimental measurements made with this rocket engine are the basis for this research. Measurements consist of experimentally determined integrated heat fluxes, measurements of the operating conditions and acoustic pressure measurements. This combustor experienced self excited combustion instabilities and thus the obtained measurements are valuable for this investigation regarding effects of heat fluxes by combustion instabilities. Lastly, the accuracy of the experimentally determined integrated heat flux values is calculated, as to gain a clear view of the limits of this research.

3.1 The Combustion Chamber BKD

First of all, the combustion chamber or combustor, known as 'Brennkammer D' was designed, built and operated by the DLR in Lampoldshausen. This sub-scale engine operates under conditions similar to upper stage rocket engines such as the European Vinci engine, ensuring relevance of this research, while its results can be used for development of existing and new rocket engines [19]. The conditions under which this test engine has been operated are graphically presented in Appendix C, being the chamber pressure, Pcc, ratio of oxidiser to fuel mass flow (ROF) defined by Equation 21 where $\dot{m}_{inj_{O_2}}$ and $\dot{m}_{inj_{H_2}}$ are respectively the oxygen and hydrogen mass flows into the engine, the hydrogen injection temperature T_{H_2} and the oxygen injection temperature T_{O_2} both measured in the injector head, as varied throughout each test run. As both propellants will achieve chamber pressure shortly before entering the combustion chamber, this pressure will be assumed when calculating injected propellant properties.

$$ROF = \frac{\dot{m}_{inj_{O_2}}}{\dot{m}_{inj_{H_2}}} \tag{21}$$

A descriptive illustration of BKD is given in Figure 18, in which it can be seen that the main cylinder segment has been designed with thick walls. This design is not optimised for flight, but allows the chamber to undergo and survive large pressures with a margin for unstable pressure oscillations which would destroy a flight-optimised combustion chamber. Besides the thick walls, the main cylinder section and the nozzle are water cooled, through separated water cycles. This separation means that integrated heat fluxes experimentally determined for this research are not including the nozzle segment, rather only the cylindrical main segment. For stable conditions, the heat flux to the injector faceplate is assumed negligible, although heat fluxes into the measurement ring are included in the integrated heat flux.

Originally BKD was designed to investigate the principles of regenerative cooling using hydrogen fuel as coolant [19]. However, this purpose was changed after the initial investigation was completed and the coolant was replaced by water while the hydrogen fuel was no longer pre-heated in a regenerative cycle. This water coolant allowed the chamber to be over-cooled and thus for it to survive more extreme test conditions, but also for calculation of heat fluxes to the combustor walls using cooling water enthalpy method explained in Section 2.2.3. The cooling cycle of the cylinder is indicated in the figure, where it can be seen that water enters the cycle from the injector face plate, runs over the length of the combustor walls and leaves the circuit at the end of the cylindrical segment that is connected with the nozzle segment. Because of this set-up, a discretised and thus localised heat flux measurement becomes impossible, while only an overall or integrated heat flux over the chamber walls can be determined experimentally. As indicated in Figure 18, the cooled section of the combustor walls has a length of 0.22m, while the diameter of this section is 0.08m. The convergent section of the chamber which leads to the nozzle is not of importance for this research, as the main theory of flame shortening as found for BKH does not apply to this section. This because all gases are estimated to be already combusted long before reaching the convergent section as completed combustion occurs around 0.1m from the injector face plate during stable combustion, the distance of which only decreases with disturbed combustion. Furthermore, BKD has a maximum chamber pressure load point of 80bar and an optimal ROF of 6, which correspond to combustion temperatures around 3600K, a thrust of 24kN and a total thermochemical power output of 90MW. These operating conditions are similar to upper stage engines such as the European Vinci

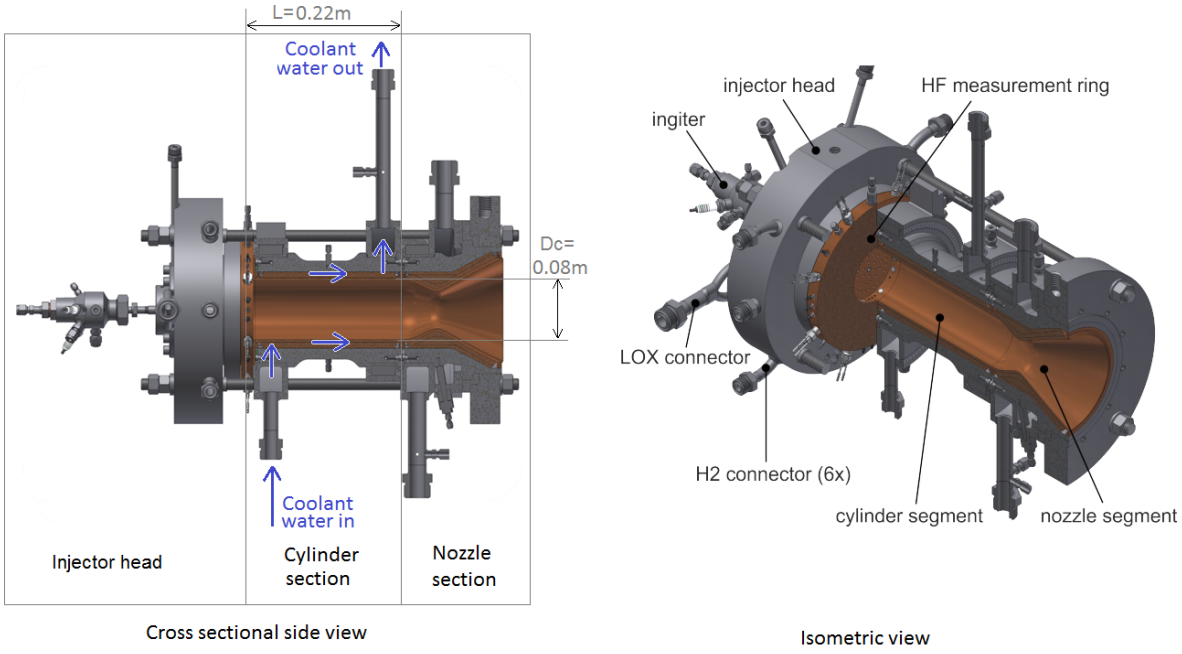

Figure 18: Lay-out of BKD. [19]

engine, while thrust and power output can be compared to smaller upper stage engines such as the Aestus engine [21].

There have been many investigations centred on this combustion chamber, resulting in a simplification of much of the work necessary for this research. One result of these investigations is the definition of the Eigenmodes present in BKD, along with their Eigenfrequencies through consolidation of theory and experimental measurements. A PSD along with the identified BKD modes is presented in Figure 19, as found during stable combustion with ROF = 4 and P_c = 60bar. Here, the 1L, 2L, 1T, 2T, 3T and 4T pure modes are indicated, along with the 1T1L, 1T2L and 1T3L combined modes.

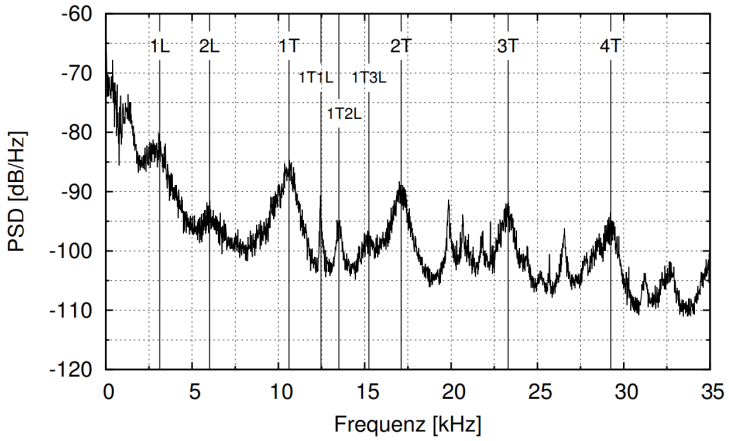

Figure 19: PSD during stable operation of BKD. [19]

The transverse modes are identified through filtering the measured raw acoustic pressure signals around found frequency peaks in the PSD and analysing the phase and amplitudes of different measurements as illustrated for the 1T mode in Figure 20, with acoustic pressure sensors located along the periphery of the chamber at identical axial distance as described in Section 3.3. However, due to this positioning the measured signals for the longitudinal and radial modes are expected to be indistinguishable when plotted in a similar fashion. For this reason the Eigenfrequencies corresponding to these modes are differentiated from each other through calculating the approximate theoretical Eigenfrequencies using

Equation 1. In this calculation, the chamber geometry is simplified as a simple cylinder with dimensions given in Figure 18 and combustion gases are taken with properties at completed combustion as an approximation. The Eigenfrequencies of the L and R modes are significantly different due to the geometry of the chamber and thus the approximate calculation is at least sufficient for differentiation between these modes, after which their respective peaks in the PSD can be identified and used as more precise measures for Eigenfrequencies.

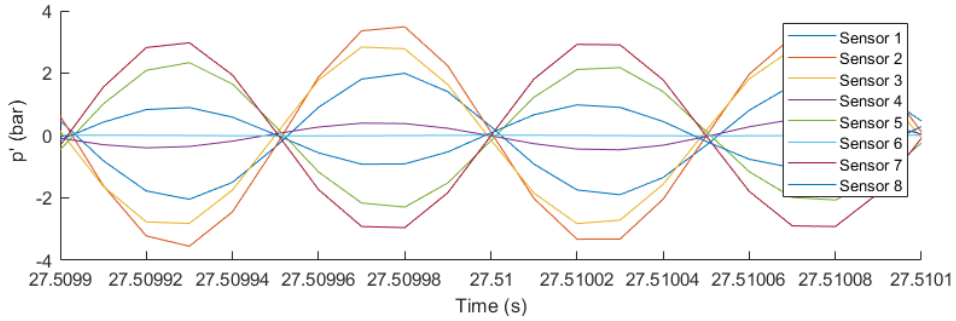

Figure 20: Phase and amplitude analysis of BKD acoustic pressure measurements during 1T standing wave mode.

Furthermore, as elaborated in Section 2.3, the 1T mode is known to be the most common and most destructive mode and is thus investigated more in depth. In BKD investigations, it has been found that over the relevant operating conditions the Eigenfrequency of the 1T mode falls between 9000 and 12000 Hz as defined through theoretical estimates and experimental analysis in previous investigations and through numerical simulations of the combustion chamber [15, 19, 48]. When investigating the measured acoustic pressure oscillations more closely using the Matlab pwelch function, it was found that in most of the test runs performed, this 1T frequency range contains the majority of the oscillatory energy during combustion instabilities. The measured acoustic pressure for one run as well as the obtained power spectral density (PSD) of a time segment with combustion instabilities is shown in Figure 21 to demonstrate the presence of this 1T frequency. In this specific case, the frequency range of 9-12kHz corresponding to the 1T mode contains 82% of all energy in the acoustic range (+2500Hz) of the PSD. The second largest energy 'peak' between 21-24kHz contains only 8% of the total energy and the 2T mode between 16-18kHz only 0.4%. For this reason and for the rest of this research, the 1T acoustic mode is focused on when considering the experimental data.

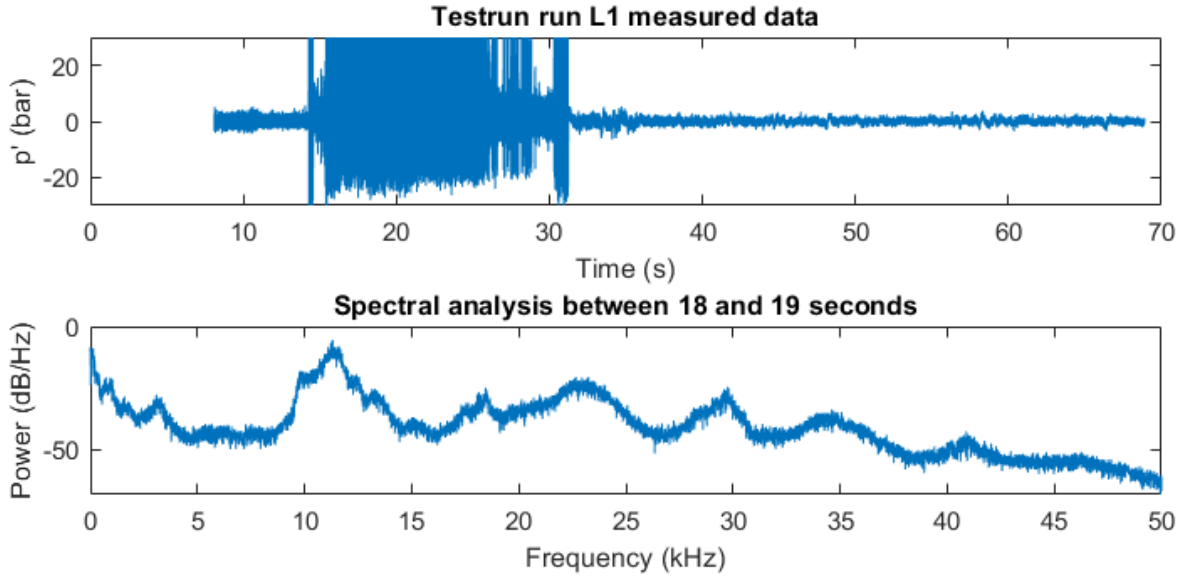

Figure 21: Spectral investigation to identify main acoustic mode.

3.2 The Injectors

The injectors used in BKD are of a shear coaxial configuration and are capable of operating with different propellant combinations, although relevant propellants consist of supercritical hydrogen (H2) with both gaslike and liquidlike properties as fuel and liquid oxygen (LOX) as oxidiser. In total there are 42 injector elements, as positioned on the injector face plate in three concentric rings, of which the geometries are illustrated in Figure 41. The outer ring contains 24 injector elements, the middle ring 12 and the inner ring 6 injector elements. In each injector element, the O2 is injected through the center tube with diameter of 3.6mm, while the H2 is injected through the surrounding tube with inner diameter of 4mm and outer diameter of 4.5mm. Throughout operation of the combustor, the mass flow of both reactants can be adjusted to change the chamber pressure and ROF and achieve varying operating conditions.

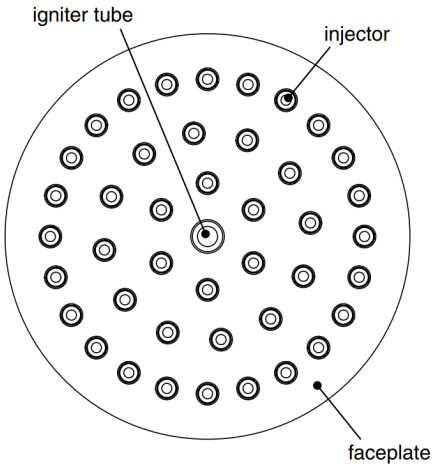

Figure 22: Injector placement in BKD injector face plate. [19]

3.3 Test Measurements

Measurements made during test runs can be divided in two classes: high frequency (HF) measurements at 100kHz and measurements made at a lower frequency (LF) of 100Hz (also 1000Hz measurements were present, although not used for this investigation). Although more sensors were present, only one HF sensor type is relevant for this research, being that used to measure the acoustic pressures in the chamber. These acoustic pressures are a measure of the magnitude and phase of oscillations of the chamber pressure around a mean value and can be used to identify and determine the properties of combustion instabilities as further elaborated in Section 2.1. The sampling rates of 100 kHz allow for creation of spectrograms and instantaneous power spectral density (PSD) estimates up to 50kHz, limited by the Nyquist criterion to be half of the sampling rate in order to correctly reconstruct the signal from a discrete measurement. This limit is deemed sufficient as it includes high frequency acoustical Eigenfrequencies of the chamber and injector geometries as investigated and defined in previous investigations and thus allows the investigation of high frequency combustion instabilities in the combustor [15, 19, 48]. Placement of these HF acoustic pressure sensors is illustrated in Figure 23, being 8 sensors equally spaced in a ring around the combustor. This ring, designated the HF measurement ring is located in between the injector face plate and the main cylinder section, as shown in Figure 18.

Other measurements such as that of the chamber pressure, ROF, injection temperatures and others require much lower sampling frequencies, as the processes involving these have slower response times, as illustrated in Figure 24. One notable measurement is the chamber wall temperature measurement. This measures the chamber wall temperature and is located halfway down the combustion chamber. At this point combustion is known to be completed for almost all cases and thus it can be used to attempt calculating heat fluxes with for example the Bartz equation. All experimental measurements and their properties including the measurement errors are summarised and indicated in Table 4.

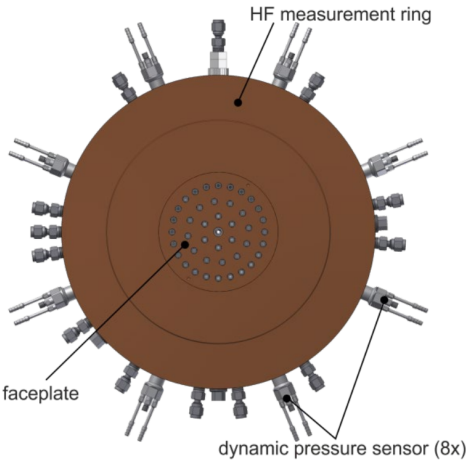

Figure 23: Sensor ring lay-out as installed at the injector face plate BKD. [19]

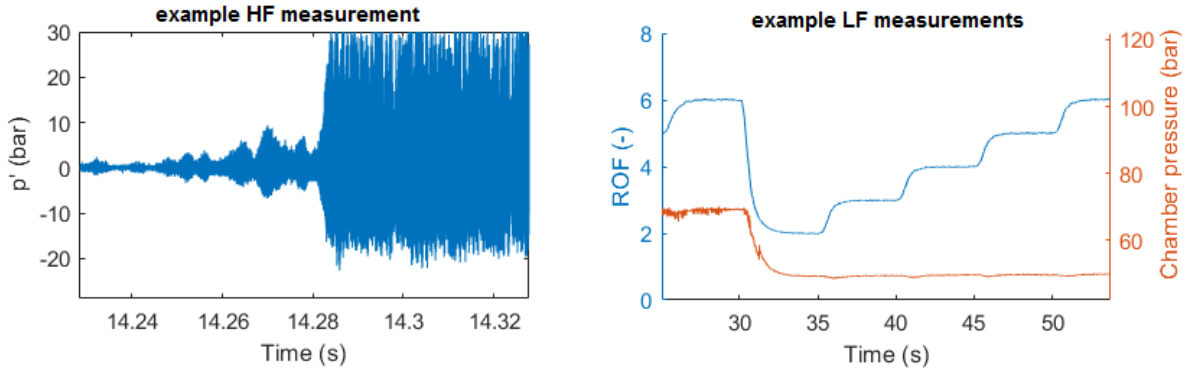

Figure 24: Illustrated difference in response times of HF signals sampled at 100kHz and LF signals at 100Hz.

Table 4: Experiment sensor data used for this research. [16, 19]

Data	Measured range during test runs	Total measurement error	Sampling Frequency
Test duration	60 to 104 s	-	-
Dynamic pressure	-30 to 30 bar	± 0.054 bar (stable) ± 0.092 bar (unstable)	100000 Hz
Chamber pressure	50 to 82 bar	1 %	100 Hz
ROF	2 to 7	5 %	100 Hz
LOX inlet temperature	108 to 118 K	±1 K	100 Hz
H2 inlet temperature	40 to 135 K	±1 K	100 Hz
LOX mass flow	2.6 to 5.7 kg/s	3 %	100 Hz
H2 mass flow	0.6 to 2.2 kg/s	3 %	100 Hz
Chamber wall temperature	370 to 526 K	±1 K	100 Hz
Coolant water inlet temperature	291 to 305 K	±2 K	100 Hz
Coolant water outlet temperature	318 to 368 K	±2 K	100 Hz
Coolant water inlet pressure	57 to 82 bar	1 %	100 Hz
Coolant water outlet pressure	35 to 53 bar	1 %	100 Hz
Coolant water mass flow	7.0 to 7.7 kg/s	0.5 %	100 Hz

Finally, an overview with all available experimental test runs, along with plots of their sensor data is presented in Appendix C. Here, not only the operating conditions are given, but also the acoustic pressure

data, the experimentally determined integrated heat flux measurements and the predictions for stable integrated heat flux that have been determined as explained in Section 4.2. It should be noted that all experimentally determined integrated heat fluxes are normalised to facilitate comparison between different test runs and to identify relative increases and decreases.

3.4 Example Calculation of Integrated Heat Flux

In this section, a numerical example of the experimentally determined integrated heat flux based on measured coolant water properties is given, as to enable external verification of obtained values and methodology. Note that the methodology is elaborated in Section 2.2.3 and will not be repeated here. First, the measurement data which will be used for this example calculation is defined in Table 5. This data represents BKD during operation and calculated values are representative for the test cases considered, considering all parameters fall within their range as defined in Table 15.

Table 5: Example measured water coolant values.

Parameter	Value	Unit
T_{in}	300	K
T_{out}	350	K
$\dot{m}$	7	kg/s

Parameter	Value	Unit
P_{in}	80	bar
P_{out}	40	bar

Next, using REFPROP the specific enthalpy of the coolant water at both inlet and outlet is calculated. The resulting values are presented in Table 6.

Table 6: Example water coolant values calculated with REFPROP.

Parameter	Value	Unit
h_{in}	$1.2064{\cdot}10^5$	J/kg

Parameter	Value	Unit
h_{out}	$3.2497{\cdot}10^5$	J/kg

These values can be implemented in Equation 8 and the resulting integrated heat flux is calculated to be 1430 kW. This is the main result of the integrated heat flux calculation. Methods used to obtain these values have been implemented into automated algorithms which allow calculation of the mentioned parameters for large datasets. Lastly, given in Appendix C are normalised integrated heat fluxes for all test runs, together with nondimensionalised trends of the required measurements. These trends allow inspection of response of calculated integrated heat flux with respect to changes in measurements.

3.5 Accuracy of Experimentally Determined Integrated Heat Flux

In this section, the accuracy of the experimental heat fluxes is determined, based on known accuracies of the sensors and the observed ranges of measurements. This is necessary in order to obtain an idea of the accuracy of the experimental data used as a basis for this research.

With the method explained in Section 2.2.3, the integrated heat flux to the chamber walls can be calculated using only the coolant water temperature measurements and the coolant mass flow measurements. From the coolant water temperature, the enthalpy can be calculated at entrance and exit, while their difference is known as the change in specific enthalpy of the water. Finally, their multiplication with the mass flow of the coolant water returns the total change in enthalpy and thus the total energy absorbed by the water. This energy is equal to the heat flux from the hot gases to the chamber walls for conditions specified in Section 2.2.3 and restated as Equation 22, which apply to BKD.

$$\dot{Q}_{int} = dH_{tot} = \dot{m} \cdot (h(T_{out}, P_{out}) - h(T_{in}, P_{in})) = \dot{m} \cdot dh \tag{22}$$

The first step in calculating the accuracy of the found integrated heat flux values, is to define the accrurracy of the used measurements. As given in Table 15, the accuracy of the water temperature, water pressure and water mass flow measurements are known to be respectively $\pm$2K, $\pm$1% and $\pm$0.5%, the measured range for inlet water temperature is 291-305K, the outlet water temperature range is 318-368K,

the inlet pressure range is 57-82bar, the outlet pressure range is 35-53 bar and the mass flow range is 7.0-7.7kg/s.

Secondly, the individual accuracies of each component in Equation 22 have to be found. As the accuracy for the mass flow is already known, the only remaining parameter is the specific enthalpy. The enthalpy is calculated by Refprop, while no analytical formula that combines both input parameters into enthalpy values is found. This makes calculation of the statistical error impossible, because of which instead a calculation to determine its maximum deviation is used. To do this, the errors in input parameters are taken as their maximum values and the corresponding error in enthalpy is calculated, which varies for different input conditions. For the rest of this work, these maximum deviations are taken as the accuracy of the enthalpy calculation with respective water inlet and outlet temperatures and pressures.

As an example calculation, if the inlet temperature is its minimum value of 291K, its respective maximum detected value, caused by a maximum sensor error, is 293K. For the inlet pressure, its respective minimum value is 57bar, with its respective maximum detected value being 57.57bar. Letting Refprop calculate respectively the correct enthalpy, enthalpy with errors in temperature and enthalpy with errors in pressure, returns respectively 80303 J/kg, 88637 J/kg and 80356 J/kg. These miscalculations correspond to an enthalpy error of 0.066% due to pressure inaccuracies and an error of 10.379% due to temperature inaccuracies. The same procedure is done for the outlet enthalpy, returning a maximum error of respectively 0.016% and 4.372% for pressure and temperature inaccuracies. Due to the different orders of magnitudes the errors due to inaccuracy in pressure measurements are neglected to facilitate further error calculations. Lastly, with errors in specific enthalpy known for both inlet and outlet enthalpy, although being highly dependent on coolant water temperatures, the error in change in enthalpy can be calculated. As the change in enthalpy is a simple function given as Equation 23, a statistical error propagation can be done.

$$dh = (h(T_{out}, P_{out}) - h(T_{in}, P_{in})) \tag{23}$$

Statistical error propagation combines errors of different parameters, to find the error in the function output. This is done based on the shape of the function that combines them, meaning parameters that are multiplied or divided have different error propagation from parameters that are added or subtracted from each other. For the purpose of this research however, it is not deemed necessary to elaborate on the deeper mathematical meaning of the methods that combine these errors, rather they are just implemented. Combining errors of two parameters that are added or subtracted follows the form given in Equation 24 and multiplications follow the form given as Equation 25. In these equations, err is the absolute error in measurement, $\text{err}_{\%}$ is the relative error in measurement, while they can be interchanged through Equation 26, where x is the measured value.

$$err_{tot} = \sqrt{err_1^2 + err_2^2} \tag{24}$$

$$err_{\%_{tot}} = \sqrt{err_{\%,1}^2 + err_{\%,2}^2} \tag{25}$$

$$err = x \cdot \frac{err_{\%}}{100} \tag{26}$$

Applying these rules to Equation 23 to find the absolute error in change in heat flux is shown in Equation 27, which is converted to relative change in change in heat flux in Equation 28. Finally, to find the total error in integrated heat flux, the multiplication rule is applied and Equation 29 is obtained.

$$err_{dh} = \sqrt{err_{h_{out}}^2 + err_{h_{in}}^2} \tag{27}$$

$$err_{\%_{dh}} = err_{dh} \cdot \frac{dh}{100} \tag{28}$$

$$err_{\%,\dot{Q}_{int}} = \sqrt{err_{\%,dh}^2 + err_{\%,\dot{m}}^2} \tag{29}$$

The error in change in enthalpy and the integrated heat flux are both a function of inlet and outlet coolant water temperatures, these can be related to each other. To do this, first the error in integrated heat flux is calculated for all possible combinations of inlet and outlet water temperatures, their ranges being defined in Table 15. Next, the integrated heat flux values corresponding to each combination of temperatures, thus corresponding to a certain calculated relative error in integrated heat flux, is calculated. Note that the mass flow rate is kept as its maximum value of 7.7, to get the maximum absolute error. The resulting plot is given as Figure 25, with a fitted function given as Equation 30, where err is the maximum error of the results and $\dot{Q}_{int}$ is the integrated heat flux. The fitted function has an R^2 value of 1 and thus it describes the maximum error in experimentally determined integrated heat flux perfectly.

$$err = 8465.9 \cdot \dot{Q}_{int}^{-1.0050} + 0.0924 \tag{30}$$

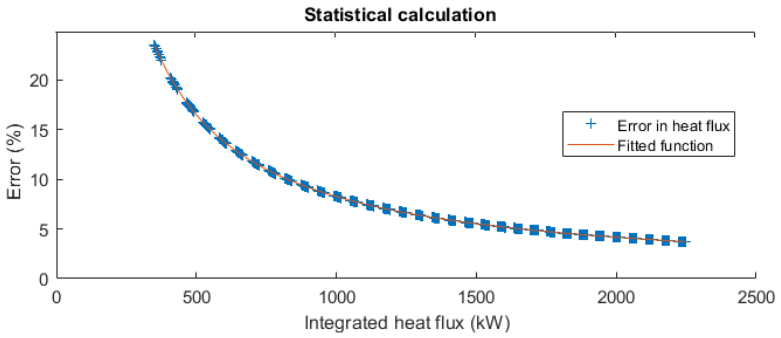

Figure 25: Maximum error versus calculated integrated heat flux magnitude.

To conclude, it can be stated that errors are larger for measurements of small heat fluxes (500kW) than for larger heat fluxes (2200kW). However, considering that for all load points of interest the experimental integrated heat flux remains above 1000kW, while instabilities are expected to increase this even more, the effective error is expected to remain below 10%. As literature reports heat flux increases which are much larger than 10% compared to the stable heat fluxes, this error is considered acceptable as it will not hinder the validation of any model. The largest source of this error is the temperature measurement and its indirect influence on the integrated heat flux through changes in enthalpy. If an analytical relation between temperature and enthalpy was known, a statistical analysis could also be performed for this factor, likely reducing the total error. If more accurate temperature measurements were available, for example with error of ±1K, the resulting curve decreases by a factor of two. An example of experimentally determined integrated heat flux curve, with an indicated potential inaccuracy, is given as Figure 26.

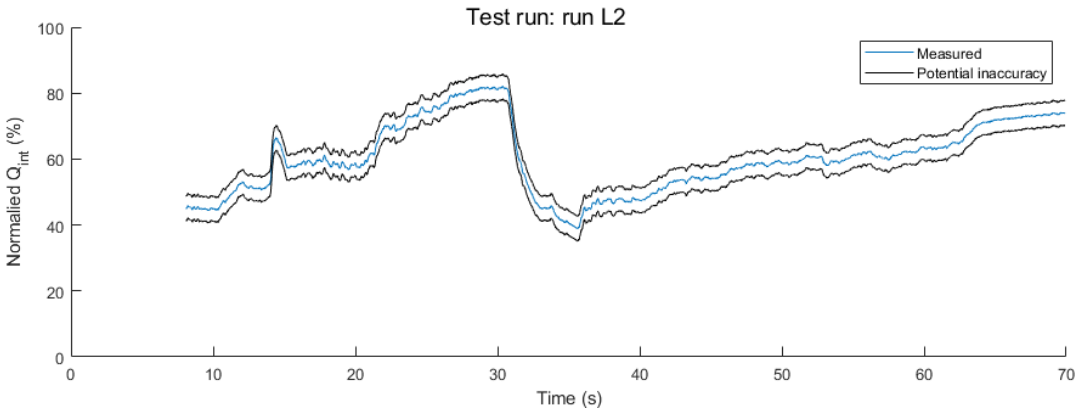

Figure 26: Experimentally determined integrated heat flux with range of potential inaccuracy.

4 Predicting Stable Integrated Heat Flux

In this thesis work, the ultimate goal is to understand and predict changes in heat flux with respect to occurrence and magnitudes of high frequency combustion instabilities. However, in order to enable observing a change in integrated heat flux and with it answer the first posed research question, first a norm should be defined with which the experimentally determined integrated heat fluxes can be compared. Predicting this norm in the form of stable heat flux is a difficult task in liquid propellant rocket engines. Even though cooling is one of the most important issues in combustion chamber design and extensive research has been performed for the past decades, accurate predictions are still rare. However, in this chapter, two attempts are made at defining this norm. The first attempt is through the widely adopted Bartz equation, elaborated in Section 4.1, being a semi-empirical relation that can be evaluated to achieve localised heat flux estimates based on measured and calculated gas parameters. The second attempt attempts to implement a new and fully empirical correlation to predict integrated heat fluxes, elaborated upon in Section 4.2. Finally, a short conclusion is made in Section 4.3.

4.1 Bartz Heat Transfer Prediction

In Section 2.2 it was elaborated how theoretical relations can be used to estimate the heat flux to the combustor walls during combustion. However, in order to implement the equations given, gas parameters must be evaluated and estimated that cannot or have not been measured in BKD during the test runs. In Section 4.1.1, these parameters are estimated and the Bartz equation is implemented. In Section 4.1.2, a heat flux profile is attempted to convert the localised heat flux values obtained using the Bartz equation to values for integrated heat flux, so that they can be compared with the experimentally determined integrated heat fluxes. Combining this theory, an example calculation is made in Section 4.1.3. Lastly, in Section 4.1.4 the resulting integrated heat flux values are compared with the experimentally determined integrated heat fluxes to analyse the accuracy and usefulness of the heat flux estimation using the Bartz equation.

4.1.1 Gas Parameter Estimation

As given in Section 2.2, the Bartz equation requires determination of a number of gas parameters that cannot always be measured during test runs. These are v, the local gas velocity, Pr is the Prandtl number, κ is the thermal conductivity of the gas, μ_{dyn} is the kinematic viscosity, $\rho^{'}$ is the free stream gas density, c_p is the specific heat of the hot gas at constant pressure, the subscript 0 represents the parameter as evaluated at combustion or stagnation temperature and the subscript am represents the parameter as evaluated at arithmatic mean gas temperature, meaning the average value of hot gas temperature and hot gas at the chamber wall. The equation by Bartz is again presented below as Equation 5.

$$h_c = \frac{0.0225}{D^{0.2}} \cdot \left(\frac{c_p \mu_{dyn}^{0.2}}{Pr^{0.6}} \right) \cdot (\rho v)^{0.8} \cdot \left(\frac{\rho_{am}}{\rho^{'}} \right) \cdot \left(\frac{\mu_{am}}{\mu_0} \right)^{0.2} \tag{5}$$

The estimation of gas parameters at combustion conditions can be achieved using the Chemical Equilibrium with Applications (CEA) program of NASA, which allows calculation of gas conditions at injection, after complete combustion is achieved and at nozzle conditions. As no complete mixing of oxidiser and fuel is present immediately at injection, the CEA calculated injection values are considered not useful, while nozzle conditions are not immediately relevant for this investigation. For this reason, parameters are calculated at completed combustion and under chemical equilibrium composition, which can be assumed due to the relative fast chemical reaction time of the LOX and H_2 propellant combination with respect to their residence time in the chamber. Besides, the combustion chamber is designed to allow for completed reaction of the propellants, being another reason to assume chemical equilibrium flow. Calculated parameters are summarised and are presented in Table 7, along with the program inputs.

As can be seen in Table 7, also the propellant inlet enthalpy is required. This is not available as a measurement, but can be calculated using REFPROP. For this calculation, only the temperature and pressure are required. For temperature, measurements in the propellant dome are available, while assuming pressure as the chamber pressure. This assumption is generally accepted, as the injected

Table 7: CEA calculated parameters and program inputs.

Output Parameters	Symbol	Unit
Hot gas density	ρ_{g0}	kg/m^3
Gas molecular weight	Mw	g/mol
Specific heat ratio	γ	-
Speed of sound	V_c	m/s
Mach number	Ma	-
Dynamic viscosity	μ_{dyn}	$kg/(m \cdot s)$
Prandtl number	Pr	-
Gas thermal conductivity	κ	$W/(m \cdot K)$
Free stream temperature	T_∞	K

Input Parameters	Symbol	Unit
Fuel inlet temperature	T_{H_2}	K
Oxidiser inlet temperature	T_{O_2}	K
Fuel inlet enthalpy	H_{H_2}	J/kg
Oxidiser inlet enthalpy	H_{O_2}	J/kg
Chamber pressure	P_c	bar
Oxidiser to fuel ratio	ROF	-

propellants will assume chamber pressure immediately after entering the chamber. In case the pressure is not equal to the chamber pressure, but to a the supply pressure for either of the propellants, the resulting enthalpy has been found to vary by no more than 0.66% for hydrogen and 0.91% for oxygen as tested for different conditions. As for the temperature, their initial temperature will still be close to their temperature as measured in the fuel and oxidiser dome as heat fluxes in the injector head are negligible and the flow of propellants can be considered adiabatic, because of which their temperature will remain almost constant from injector manifold to the injection.

It can be noticed that CEA only calculates hot gas parameters while assuming a uniform cross sectional profile of the gas. For this reason no information is known about gas conditions closer to the chamber walls, meaning no values for arithmetic mean temperature can be calculated. As no CEA values nor measurements are present, this temperature was estimated with a different method, as given in Equations Equation 31 and 32 [49]. The hot gas temperature at combustion is given as T_{g0} as obtained through CEA, the gas free stream temperature is given by T_∞ and the hot gas temperature at the wall is given as T_{gw}. γ and Ma, the specific heat ratio and mach number respectively, are evaluated at combustion temperature. The recovery factor, r, can be estimated for turbulent flows as $Pr^{1/3}$, representing stagnation of the flow close to the wall. Practically, the recovery factor reduces the temperature from stagnation or combustion temperature temperature, but allows the temperature to be higher than the free stream temperature.

$$T_\infty = T_{g0} \cdot (1 + \frac{\gamma - 1}{2} Ma^2)^{-1} \tag{31}$$

$$T_{gw} = T_\infty \cdot (1 + r\frac{\gamma - 1}{2} Ma^2) \tag{32}$$

Now that the arithmetic mean temperature can be calculated, the gas density and viscosity parameters can be estimated under these conditions. To calculate the density, isentropic gas relations are used as a first order estimation for gas properties at the same chamber cross section [49]. This is shown in Equation 33.

$$\rho_{am} = \rho_{g0} \cdot \left(\frac{T_{am}}{T_{g0}}\right)^{\frac{1}{\gamma - 1}} \tag{33}$$

As for the kinematic viscosity, CEA gives the kinematic viscosity of the combined combustion products, but only at combustion temperature and can thus not be further used to evaluate the viscosity of the combustion products at varying temperatures. Also no simple estimation can be made since the gas consists of more than one gas species and no pre-existing experimental relation for the combined gases can be found. However, for each of the gas components individually these experimental relations do exist for a limited range of temperature and pressure conditions and there have been investigations into how these individual components can be combined into a mixed gas viscosity [50, 51].

First of all, a short investigation is made with CEA to identify the different combustion products present in the hot gases, as to identify what components the mixed gas viscosity will consist of. It should be noted that the gas components will vary with varying ROF at injection, although the main difference is expected to be in the ratio of hydrogen and water as combustion products and not in the remaining gas

components. An example of found combustion products is given in Table 8. To limit the complexity of the viscosity approximation and due to the limited presence of combustion products other than hydrogen and water, it was chosen to approximate the combustion gases by considering only these two combustion products.

Table 8: Example combustion product fractions for ROF=3.

Injected reactants	Mole fraction
H_2 (hydrogen)	84.21%
O_2 (oxygen)	15.79%
Total	100 %
Combustion product	Mole fraction
H_2 (hydrogen)	61.78%
H_2O (water)	37.59%
H	0.54%
OH	0.09%
Total	100%

To automate the mole fraction estimation for water and hydrogen as combustion products using present experimental information, a simple estimation can be made as described by Equation 34 and Equation 35 which makes use of only the instantaneous ROF value. The full derivation of these equations can be found in Appendix A. These equations make use of the stoichiometric combustion ratio of hydrogen and oxygen, being 8 grams of oxidiser (oxygen) per gram fuel (hydrogen) which would theoretically cause complete combustion of all reactants. Considering no test runs involve a ROF equal or higher than the stoichiometric ratio, there will always be an excess of hydrogen that will not combust and will thus remain hydrogen, while all injected oxygen is assumed to combust to form water in the ideal case. In these equations x_{H_2O} and x_{H_2} are respectively the mole fractions of water and hydrogen as combustion products. To justify neglecting the other combustion products a comparison between CEA values and approximated fractions is presented in Table 9, showing a prediction error of maximum 11% although the error is much smaller for most cases. Whether these errors are too large will be determined after the first mixed viscosity calculation.

$$x_{H_2O} = \frac{ROF}{ROF_{stoichiometric}} = \frac{ROF}{8} \tag{34}$$

$$x_{H_2} = 1 - x_{H_2O} \tag{35}$$

Table 9: Combustion gas mole fraction approximation.

ROF value	Products	CEA mole fraction	Approximated mole fraction	Error
3	H_2 (hydrogen)	61.781%	62.50%	0.281%
	H_2O (water)	37.589%	37.50%	0.089%
	Remaining	0.630%	0%	0.630%
4	H_2 (hydrogen)	48.352%	50.00%	1.648%
	H_2O (water)	48.856%	50.00%	1.144%
	Remaining	2.792%	0%	2.792%
5	H_2 (hydrogen)	35.697%	37.50%	1.803%
	H_2O (water)	57.821%	62.50%	4.679%
	Remaining	6.682%	0%	6.682%
6	H_2 (hydrogen)	25.170%	25.00%	0.170%
	H_2O (water)	63.855%	75.00%	11.145%
	Remaining	10.975%	0%	10.975%

Now that a mole fraction can be quickly estimated for both major components in the combustion gases, their individual viscosity properties must be determined before they can be combined into a mixed viscosity. To do this, dynamic viscosity can be obtained using the REFPROP program of NIST for limited temperature and pressure ranges [34]. The pressure dependency of the dynamic viscosity is presented in Figure 27 for the range of pressures encountered in the test runs and is determined negligible as the change in dynamic viscosity is $< 1\%$ for water and $< 0.5\%$ for hydrogen over the entire considered pressure range. The temperature does have an effect, as presented in Figure 28 and must thus be included in the dynamic viscosity approximation per component. To do this, the relevant temperature range is limited to be above 600K for water as the dynamic viscosity profile stabilises after this point. The lower limit for hydrogen is limited by REFPROP to around 200K while the upper limit for both components is limited to around 1500K. Using these ranges, a function is fitted to both data sets, being respectively Equation 36 and Equation 37 for hydrogen and water, both having an R^2 value of 1. It is assumed that this fitted function can be extrapolated to temperature ranges relevant for combustion temperatures present in the test runs (2200K to 3650K).

$$\mu_{dyn_H}(T) = 3.822 \cdot 10^{-8} + 1.604 \cdot 10^{-7} \cdot T^{0.703} \tag{36}$$

$$\mu_{dyn_{H_2O}}(T) = -5.212 \cdot 10^{-6} + 4.714 \cdot 10^{-8} \cdot T - 4.317 \cdot 10^{-12} \cdot T^2 \tag{37}$$

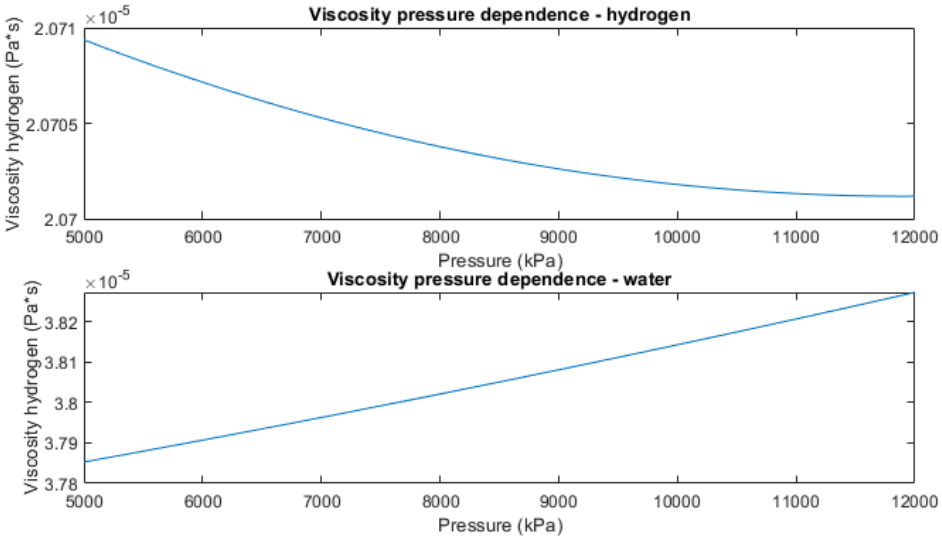

Figure 27: Pressure dependency of dynamic viscosity for H_2 and H_2O.

Now that the type and mole fractions of the components can be simply approximated, along with an approximation for their viscosity, they need to be combined into one viscosity for a mixed gas that can be calculated for different temperatures. In order to do this, some methods exist, of which one is selected that makes use of a coefficient presented in Equation 38 to allow calculating a weighted average based on mole fractions and molecular weights of components i and j, in this case hydrogen and water, as shown in Equation 39 [50,51]. In these equations, ϕ is a coefficient, μ_{dyn} is the dynamic viscosity, Mw are molar masses and x are mole fractions. Note that a similar equation for kinematic viscosities would be based on a volumetric averaging, rather than a mass averaging as performed here for the dynamic viscosity.

$$\phi_{ij} = \frac{\left(1 + \left(\frac{\mu_{dyn_i}}{\mu_{dyn_j}}\right)^{1/2} \cdot \left(\frac{Mw_j}{Mw_i}\right)^{1/4}\right)^2}{\frac{4}{\sqrt{2}} \cdot \left(1 + \frac{Mw_i}{Mw_j}\right)^{1/2}} \tag{38}$$

$$\mu_{dyn_{mix}} = \sum_i \frac{x_i \cdot \mu_{dyn_i}}{x_i + \sum_{j \neq i}(x_j \cdot \phi_{ij})} \tag{39}$$

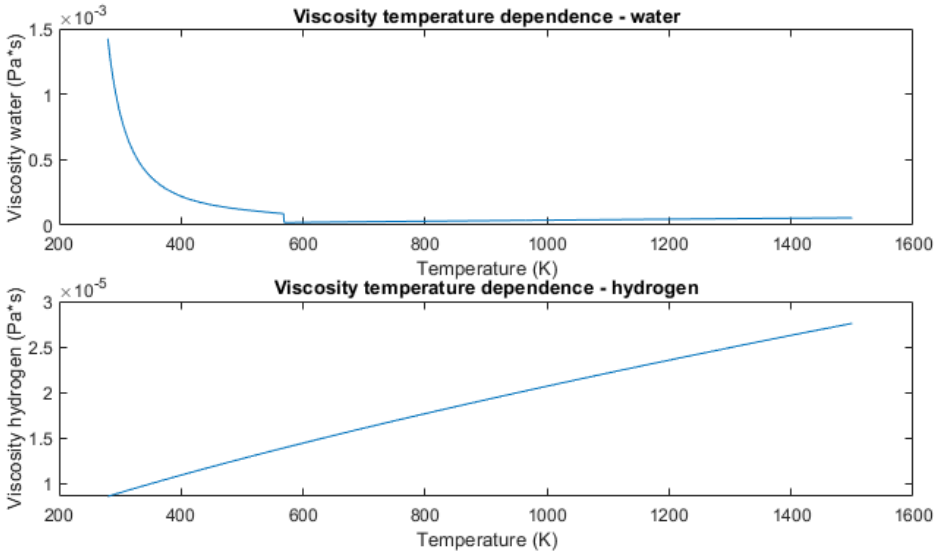

Figure 28: Temperature dependency of dynamic viscosity for H_2 and H_2O at pressure of 70bar.

Finally, the method can be verified by calculating estimated kinematic viscosities at combustion temperature and comparing with present CEA data. Verification points of interest are at high values of ROF, due to the relatively high error in mass fraction approximations as shown in Table 9, and at high temperature values due to the significant amount of extrapolation required of the fitting function for temperature dependency. The resulting prediction and CEA values calculated are presented in Figure 29, as calculated for one test run that contains both these critical verification points. Note that viscosity here is determined as kinematic viscosity, while the obtained estimated viscosity is converted using Equation 40 to enable comparison. The maximum error found is 3.4% and thus the method with all its simplifications is considered acceptable for all useful ranges.

$$\mu_{kin} = \frac{\mu_{dyn}}{\rho_{mix}} \tag{40}$$

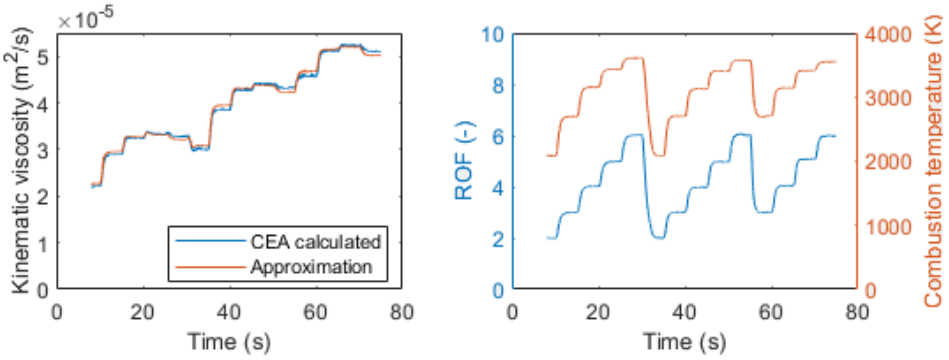

Figure 29: Verification of kinematic viscosity approximation.

Now, all other parameters necessary to calculate the convective heat transfer coefficient using the Bartz method can be obtained from CEA or calculated using approximations. This allows for calculation of local heat flux at the combustion chamber cylindrical section in which complete combustion has taken place. However, as integrated or overall heat flux values are the only experimental data available for comparison, a heat flux profile has to be implemented that simulates the flamelength over the length of the combustion chamber, so that the calculated local heat fluxes can be integrated for comparison.

4.1.2 Implementation of Heat Flux Profile

In order to simulate the incompleteness of combustion in the form of a combustion profile, a heat flux profile has to be generated that corresponds to given chamber conditions. The assumed profile shape is presented in Figure 30b and is based on known heat flux profiles from literature [11, 12, 14, 52–54], an example of which is presented in Figure 30a. In this heat flux profile, there are 4 main parameters to consider: the distance at which the heat flux starts rising, the distance at which the heat flux attains a constant value, the initial heat flux value and the final heat flux value. The rise in heat flux is assumed to follow a sinusoidal profile which is fully defined with the four previously mentioned parameters, resulting in a local heat flux profile as seen in Figure 30b. Since throughout literature the heat flux profile varies depending on the experimental set-up and a linear increase is deemed oversimplified, the chosen sinusoidal profile was found to match what is described in most literature, although other profiles could also be applied. Note that the peak in heat flux in the experimental curve starting at -0.1 m does not take place in the cylindrical section of the combustor, but in the nozzle section, and is thus not relevant or modelled in the assumed profile.

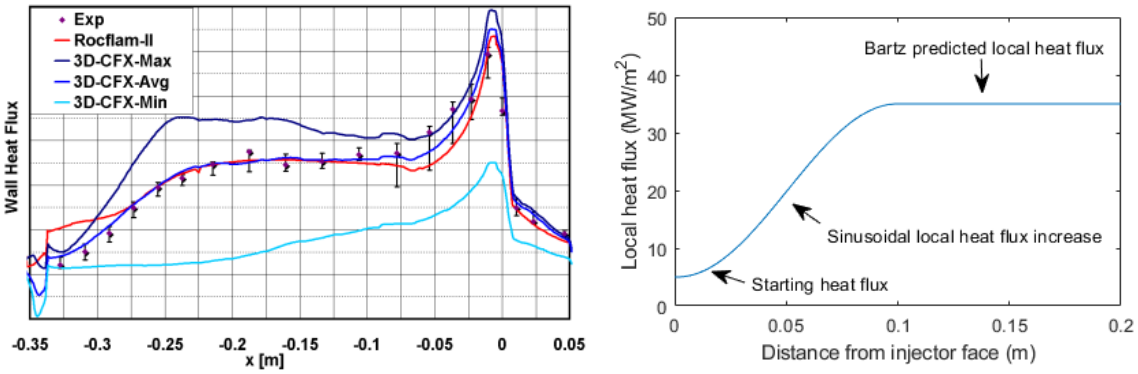

(a) Experimental heat flux profile. [54]

(b) Example of assumed heat flux profile

Figure 30: Experimental versus applied flame length in the Bartz approximation.

The distance at which the heat flux starts rising is assumed to be zero, as any delays seen in literature are small and are already implemented through the slow initial rising of the sinusoidal curve in the profile. The distance at which the local heat flux stops rising, is not a constant value and is much harder to implement. From CFD models it has been found that the distance at which final gas temperature is reached is between 80-120mm for BKD with ROF values between 4 to 6 and P_c of 80 and is varying with different factors such as ROF and propellant injection temperatures [15, 30].

In order to estimate this final flame length, some theory exists regarding LOX core break-up, which can be argued similar to the combustion length as at this point all reactants will be mixed and combusted. This topic is rather complex, as LOX core break-up of a coaxial shear injector is affected by many parameters such as injector dimensions and momentum flux ratios of the injected propellants [46]. However, simplifying the work in this research, an investigation has already been completed regarding this phenomena in BKH. Results included Equation 41, which is an experimental relation to determine LOX core during stable combustion, as nondimensionalised through dividing by the injector diameter. This equation applies for the experimental set-up of BKH, based on experimental data for BKH to determine the LOX core length during stable combustion. It is suggested that this equation requires recalibration for usage with differing test set-up, although no mention is made of limits in operating conditions [36, 55]. The resulting relation returned overall good matches with an average misprediction in L/D of 1.67 and maximum misprediction in L/D of 5 for BKH. In this equation, L/D is nondimentionalised LOX core length, while J represents the momentum flux ratio between both injected propellants.

$$\frac{L}{D} = 37 \cdot J^{-0.13} \tag{41}$$

The momentum flux ratio is defined as Equation 42, where ρ_{H_2} and ρ_{O_2} are respectively the densities of injected hydrogen and oxygen, and V_{H_2} and V_{O_2} are their respective injection velocities. The densities are determined using REFPROP for measured injection temperatures, as the temperature of the gases will not vary much between injection head and injection, and at chamber pressure as this pressure will quickly be assumed by the injected propellants after injection and will thus determine the relevant density. The injection velocity of the gases can be calculated using Equation 43, as shown for hydrogen although the same formula applies to oxygen. Here, $\dot{m}_{inj_{H_2}}$ is the total hydrogen mass flow, ρ_{H_2} is its density at injection, $A_{inj_{H_2}}$ is the hydrogen injector cross sectional area and there are 42 injection elements.

$$J = \frac{\rho_{H_2} \cdot V_{H_2}^2}{\rho_{O_2} \cdot V_{O_2}^2} \tag{42}$$

$$V_{H_2} = \frac{\dot{m}_{H_2}}{A_{inj_{H_2}} \cdot \rho_{H_2} \cdot 42} \tag{43}$$

Due to similar injector geometries in BKH and BKD and no mention is made of useful range of momentum flux ratio, it is assumed that this relation holds for BKD. Although there is no available data on the accuracy of this model, it is currently the best available model and thus a comparison with numerical solutions which showed good agreement is considered sufficient to verify this assumption. If other measures of stable LOX core length are available through another experimental set-up or validated model, it is recommended to use these instead. Next, the final heat flux value of the profile has to be estimated. The final heat flux value of the profile is taken as the output of the Bartz equation, representing the heat flux into the chamber walls at completed combustion. The starting value of the profile was found dependent on the injection temperature of the hydrogen, where lower injection temperatures give lower local heat flux values near the injection face plate before combustion [30]. This heat flux profile can then be integrated over the chamber length and circumference to determine the total heat flow.

The initial heat flux has been found in literature to vary between 0 MW/m^2 and 10 MW/m^2 for similar sub-scale combustion chambers [11,14,52]. The difference in initial heat flux within this range is expected to be related to the injection temperature of the hydrogen, thus an attempt is made at relating the two parameters. To do this however, a limited amount of data are available from test runs such as that some runs have an average hydrogen injection temperature of 45K (liquid injection) and others of 90K (gaseous injection), while no test runs with both temperature ranges exist. For this reason, a much simplified linear relation is assumed with some margins (40K is chosen as minimum temperature and 90K as maximum for the linear relation) and the initial heat flux is estimated with Equation 44. In this equation, $\dot{q}_{initial}$ is the local heat flux at the injector face place and given in J/m^2 and T_{H_2} is the hydrogen injection temperature given in K. Although this relation might not represent the real trend, since it is based on only interpolation between two points, a change in initial heat flux between 0 and 10MW/m^2 has been calculated to induce only a maximum change of 8% in calculated integrated heat flux. Although this change in integrated heat flux should bring the calculated integrated heat flux values closer to the experimentally determined heat flux values, the maximum induced error is thus also below 8%, although expected to be much lower.

$$\dot{q}_{initial} = \frac{10 \cdot 10^3}{90 - 40} \cdot (T_{H_2} - 40) \tag{44}$$

It should be noted that the initial heat flux value of the profile is taken as function of the hydrogen inlet temperature, while the inlet temperature of oxygen is not considered. Whether the oxygen inlet temperature has an effect is not relevant as this temperature is kept constant throughout all present test runs.

4.1.3 Bartz Example Calculation

Combining the elaborated theory, an example calculation is made so that the method and results can be verified externally. First, the load point which will be used for this example calculation is defined in Table 10. This load point represents BKD operating conditions and calculated values are representative for the test cases considered, considering all parameters fall within their range as defined in Table 15.

Table 10: Example measured values.

Parameter	Value	Unit
P_c	60	bar
T_{H2}	45	K
T_{O2}	116	K
T_w	460	K

Parameter	Value	Unit
ROF	6	-
$\dot{m}_{H2}$	0.73	kg/s
$\dot{m}_{O2}$	4.35	kg/s

These are all relevant parameters that could be obtained using test measurements. Next, the specific enthalpy values of the propellants are calculated using REFPROP. Resulting specific enthalpy values are presented in Table 11.

Table 11: Example values calculated with REFPROP.

Parameter	Value	Unit
h_{H_2}	$3.864{\cdot}10^5$	J/kg

Parameter	Value	Unit
h_{O_2}	$-8.597{\cdot}10^4$	J/kg

Next, as all input parameters are available, combusted gas properties can be calculated with CEA. This is performed and resulting values are presented in Table 12.

Table 12: Example values calculated with CEA.

Parameter	Value	Unit
ρ_{g0}	2.5194	kg/s
Mw	13.2340	g/mol
γ	1.1371	-
V_c	1594.1	m/s
Ma	0.2402	-

Parameter	Value	Unit
μ_{dyn}	$1.0758{\cdot}10^{-4}$	kg/(m· s)
Pr	0.5194	-
κ	2.11370	W/(m· K)
T_∞	3572.5	K

The remaining parameters as required for the Bartz equations need to be calculated with different methods, as presented in Section 4.1. The methods are not further explained, but implemented into automated algorithms which allow calculation of the mentioned parameters for large datasets. Resulting values as obtained with these algorithms are presented in Table 13 for verification of the calculations. Lastly, given in Appendix E are nondimensionalised trends calculated parameters for all test runs, together with nondimensionalised trends of the required measurements. These trends allow inspection of response of values calculated in this section with respect to changes in measured values.

Table 13: Example calculated values.

Parameter	Value	Unit
T_{g0}	3631.3	K
T_{am}	3625.6	K
ρ_{am}	2.4907	kg/m^3
x_{H_2O}	0.75	-
x_{H_2}	0.25	-
$\mu_{dyn_{H_2O}}$	$1.0895{\cdot}10^{-4}$	kg/(m· s)
$\mu_{dyn_{H_2}}$	$5.10549{\cdot}10^{-5}$	kg/(m· s)

Parameter	Value	Unit
$\mu_{dyn_{am}}$	$1.0549{\cdot}10^{-4}$	kg/(m· s)
L/D	29.5827	-
J	5.59	-
$\dot{q}_{initial}$	1	MW/m^2
h_c	11069.2926	W/(m^2·K)
$\dot{q}_c$	34.4532	MW/m^2
$\dot{Q}_{pred}$	1280	kW

4.1.4 Bartz Equation Results

Now that the Bartz equation can be implemented, with CEA calculated or approximated parameters and that the local heat flux profile can be estimated, a prediction can be made for the instantaneous integrated or overal heat flux. This is useful for this research, as there are data available from experiments and thus the Bartz approach can be verified. Two examples for test runs are presented in Figure 31, where it can be seen that the prediction using the Bartz equation returns reasonable results for the integrated heat flux over time. The time profiles show similar trends and magnitudes are not mispredicting by large factors, while resulting mean and maximum deviations of all test runs are presented in Table 14. However, the profiles are not predicting with the predetermined wanted accuracy range of 5% and can thus not directly be used for the purpose of this report: evaluating whether integrated heat flux changes with instabilities. For this reason it is interesting to evaluate what potential causes for the deviations are.

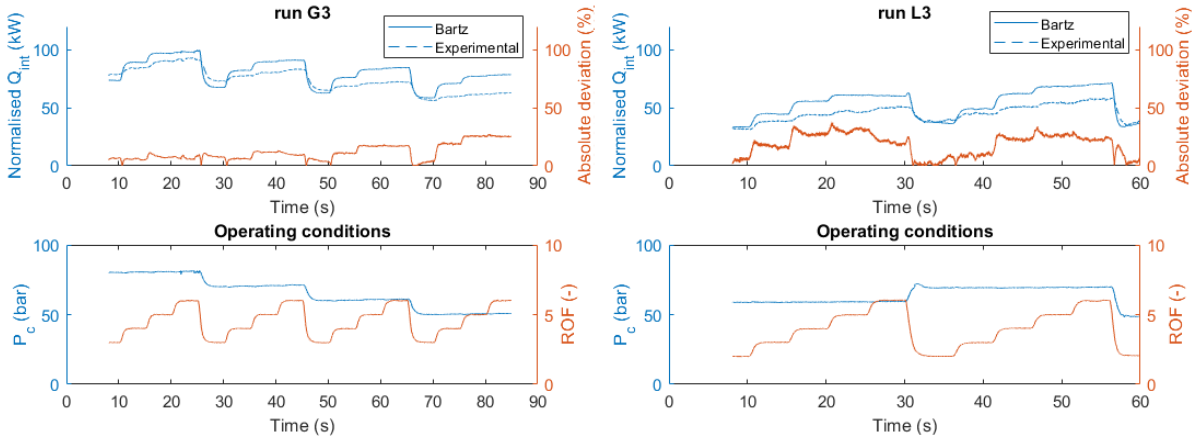

Figure 31: Verification of Bartz implementation with test data.

Table 14: Resulting deviations of Bartz equation implementation for all test runs.

Test run	Mean deviation	Max deviation
L1	8.7502 %	44.7247 %
L2	9.0521 %	37.653 %
L3	18.6396 %	37.3983 %
L4	13.1819 %	41.188 %

Test run	Mean deviation	Max deviation
G1	9.7172 %	25.7182 %
G2	10.0603 %	26.9543 %
G3	11.6085 %	27.4024 %
G4	11.5349 %	30.5439 %

It can be noted that the errors in the G3 run initially remain small, but show a rise towards the end of the run. This can be due to the test-setup experiencing effects due to extended test periods, although it is more likely related to the chamber pressure values which show a decreasing trend where the error becomes larger. To improve the relation it is recommended to update the relation for calculating the heat transfer coefficient by modifying the effect due to the chamber pressure as included in Equation 5 by Bartz. If this does not improve results, the test set-up could be the cause.

The general deviations of the L3 test run are much larger (mean: 18.6%) than those of the G3 run (mean 11.6%). The main difference between these two runs is the injection temperature of the hydrogen, which is thus likely the main reason for the increased deviation in predicted heat flux and measured heat flux. As the approximations made for calculating the initial local heat flux in the combustion chamber directly take into account injection temperature of the hydrogen, it is likely that this linear approximation does not suffice and a more intricate relation should be determined. Besides the initial local heat flux values however, also the combustion length takes into account the hydrogen temperature in the form of hydrogen density in the momentum flux ratio. Here it could also be that some modifications are required.

Furthermore, the general deviations show a slight overprediction with respect to the experimental data, but overall there are both over- and underpredictions. This could be an indication that the assumption that stable flame length is identical to the LOX core length is underpredicting the real flame length. If the real flame length would be longer, the predicted integrated heat flux would show a drop, perhaps bringing the predicted integrated heat flux closer or under the experimental values. As the overall heat flow is not underpredicted and does not show any consistent down-shifts with respect to the experimental values, the assumption that radiative heat fluxes can be neglected seems to be valid or at the very least would not improve results. For these reasons it is deemed unnecessary to implement further additions to take this into account.

As a conclusion to this attempt at implementing the Bartz equation to predict integrated heat fluxes in BKD and to improve the relation, next steps can be presented. First, it is recommended to include more hydrogen temperature effects into the prediction method. Note that this improvement was not made in this research, as no data or relation was available on this effect and thus the model would require more experimental correction factors and assumptions. Secondly, an attempt can be made at including a measure for radiative heat fluxes into the combustor walls into the overall integrated heat flux calculation, besides the convective heat flux predictions of the Bartz equation. Finally, as both improvements would require a significant amount of work and are not part of the research goals of this work, it has been decided not to attempt these improvements. Rather, it is chosen to attempt a new method that has already shown results in the internship preceding this work.

4.2 Experimental Heat Transfer Prediction

As an alternative to the method that utilises the Bartz equation, a method has been come up with during a short research internship as predecessor for this thesis work [24]. This method correlates the controlled parameters of the test run with measured integrated heat fluxes at time periods of known stable combustion and uses this relation to predict integrated heat flux for given test conditions. This principle is explained in Section 4.2.1. Ultimately this prediction can be extended to time periods of unstable combustion and to identify whether expected and measured integrated heat flux deviate, indicating an effect due to combustion instabilities. However, while this method showed promising results and allowed for initial analysis regarding integrated heat flux deviations, work on it was limited due to the time constraints of the research internship. For this reason, work on this method was continued, first of all by implementing a new data selection method to exclude instabilities from experimental data as explained in Section 4.2.2. Also, transients in operating conditions are excluded from the data sets in the new data pre-selection methods, as explained in Section 4.2.3, since effects during operating condition transients are not relevant for this research and this pre-selection is expected to improve results. Finally, a method accuracy analysis is performed in Section 4.2.4 to evaluate the usefulness of this method.

4.2.1 Work Performed During Internship

The method developed during the internship correlated the controlled chamber conditions of ROF, chamber pressure and hydrogen inlet temperature with the experimental integrated heat flux data. It does this through a function in the shape of Equation 45, with coefficients a, b_1, b_2, b_3, b_4 and c. The shape of this function, to be a power function, was determined based on the shape assumed by Bartz as it is deemed most fitting with some experimental analysis [33] with limited input parameters. The number and type of parameters included in this equation is determined through an iterative process in which coefficients were added or removed [24]. The coefficients themselves are solved for using a fitting algorithm that minimises the difference between the fitting function and experimental data. This function is thus an empirical relation and not a theoretical one. Finally, with optimised coefficients, the heat flux can be predicted as given by $\dot{Q}_{pred}$.

$$\dot{Q}_{pred} = a \cdot P_c^{b1} \cdot ROF^{b2} \cdot T_{H_2}^{b3} + T_{H_2} \cdot b_4 + c \tag{45}$$

During the internship, only a rough instability analysis was performed on the experimental data in an effort to exclude this data from the correlating process. In this part, an envelope of the acoustic pressure data was used as a measure for acoustic pressure oscillation amplitudes at each time stamp. This envelope was sampled to match the HF acoustic pressure data to the LF integrated heat flux and operating condition measurements and compared with the static pressure data to see if that time sample could be considered stable according to the definition given in Section 2.1, being that the amplitude of acoustic pressure oscillations remains below 5% of static pressure. If it did not, the time sample was removed from all datasets before correlating.

4.2.2 Exclusion of Instability Periods

However, through manual inspection of the experimental heat flux data, it was found that heat flux data showed a delayed response to all chamber conditions of on average 0.5 seconds. For this reason, it was deemed necessary to extend the removed time sample to 0.5 seconds before and after the detected instability, assuming a similar delay applies to any effects instabilities might cause. An example of this instability detection method is presented in Figure 32.

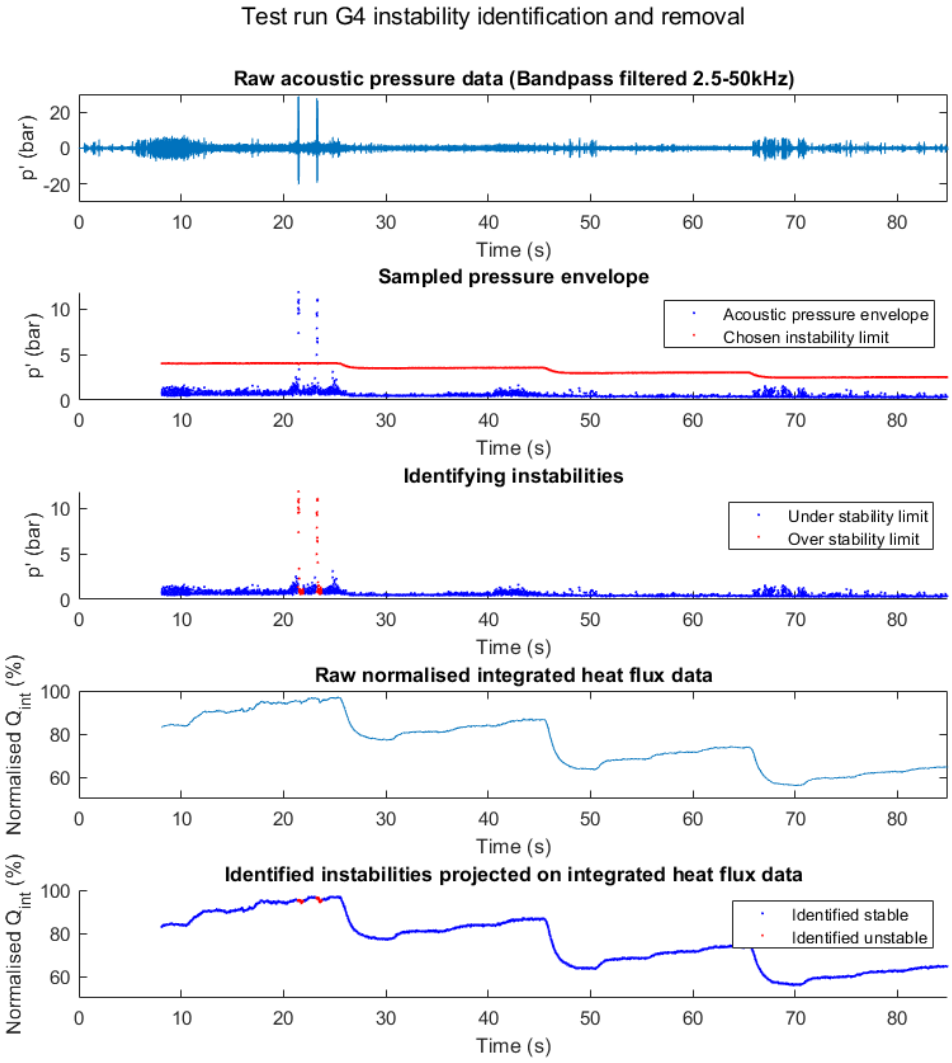

Figure 32: Example of combustion instability detection.

In this process, the magnitude of the instabilities, A, has been defined as the Root Mean Square (RMS) of the acoustic pressure oscillations, p'_{RMS} multiplied by $\sqrt{2}$. This can be done, as the acoustic pressure signal is mostly sinusoidal. This method was preferred over an envelope function, as it was found that the slow response of these functions would cause the function to return amplitudes at time periods before and after combustion instabilities where there are no more pressure oscillations. Whenever in this report the magnitude of the instabilities is referred to, this method was applied.

$$A = p'_{RMS} \cdot \sqrt{2} \tag{46}$$

4.2.3 Exclusion of Transients in Operating Conditions

Also a transient analysis was included in the data preparation, in which transient chamber conditions are identified and removed from the time samples. The advantage of this is that transient conditions might not follow the same relation as the steady conditions due to retention of heat and chamber heat capacity, which are thus not useful for trying to predict steady integrated heat fluxes. For this reason and for the remainder of this research, the time periods with transients in operating conditions are not considered, although it could be considered an expansion of this work to update the experimental equation with more parameters so that also periods with transient operating conditions can be included. For now, the research is focused on periods of steady combustion, meaning operating conditions and thus integrated heat fluxes are not changing within each considered time frame. In order to do this, specifically ROF and chamber pressure data are analysed to identify relatively sudden changes in states. The threshold for what is considered a 'sudden change' is determined iteratively, being a ROF change of more than 0.03 and a chamber pressure change of more than 0.15 bar as averaged over the next 0.1 seconds of each time period and relative to the average value of the previous 0.1 seconds. This thresholding results in a transient detection as presented in Figure 33.

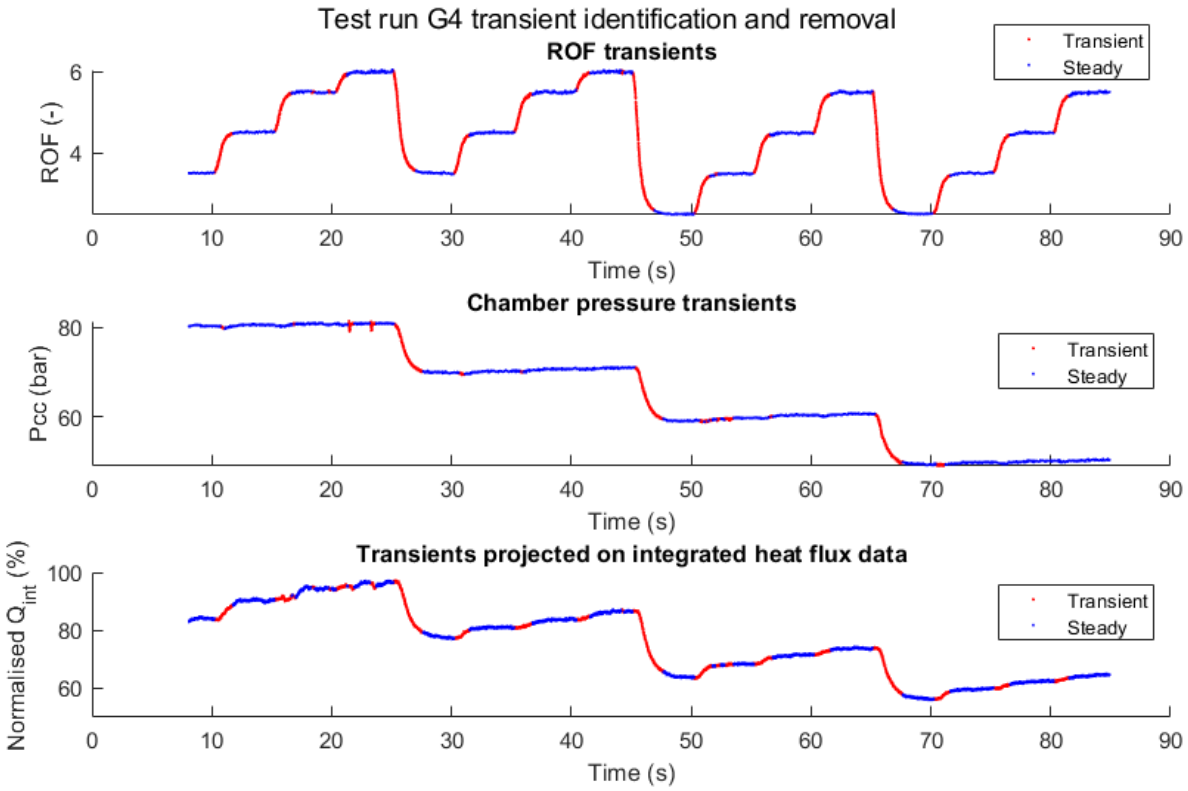

Figure 33: Example of ROF and chamber pressure transient condition detection.

4.2.4 Results of Improved Experimental Correlation Method

Finally, both instability and transient detection methods are combined so that both are removed from the experimental data before a correlation is found. A result of total identified useful experimental data is given in Figure 34.

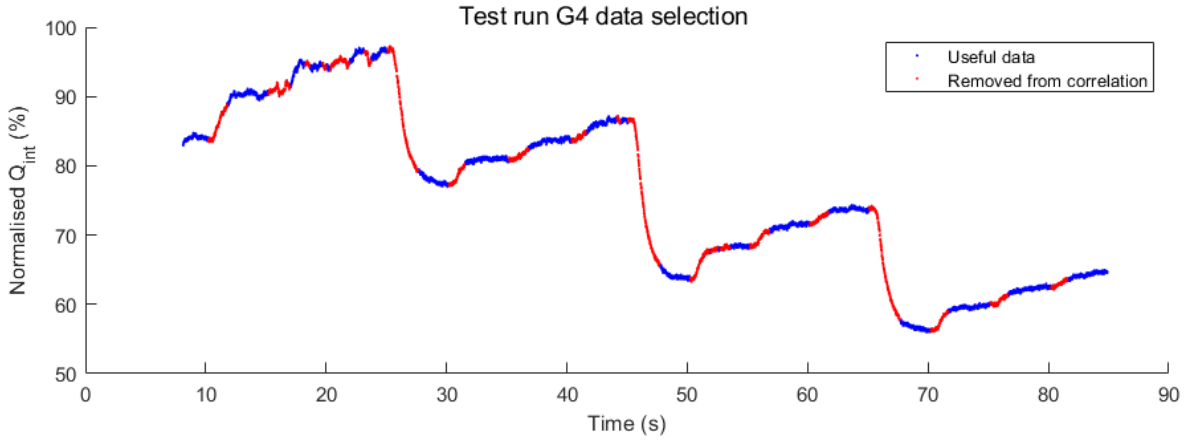

Figure 34: Example of resulting useful data detection.

In order to analyse the usefulness of a data fit, it can be evaluated in different ways: the mean deviation from the data it was fitted to, the mean deviation from all data in a test run it should be able to predict can be used, the R^2 of the fit with respect to the data it was fitted to and the Residual Standard Error (RSE) of the fit with respect to the data it was fitted to. Note that the R^2 and RSE are calculated with respect to the data it was fitted to, as transient operating conditions are not of interest in this research and as almost all maximum deviations are present in transient operating conditions or during combustion instabilities. These mentioned measures are presented in Table 15, where it can be noticed that the overall deviation measured with the fitting data for all cases is below 5%, which is the imposed accuracy as defined in the research goal. An example of a resulting prediction is shown in Figure 35.

Table 15: Analysis of fit accuracy.

Test run	Mean deviation from fitting data (%)	Mean deviation from all data (%)	R^2 value of fit	RSE value of fit	Percent of data used for fitting (%)
L1	1.817	9.937	0.954	25.232	58.750
L2	2.827	3.589	0.939	53.474	68.511
L3	1.495	1.662	0.985	43.049	71.023
L4	3.826	4.144	0.889	64.032	67.171
G1	1.723	1.609	0.972	18.946	65.703
G2	2.429	4.787	0.949	78.283	66.694
G3	2.073	2.034	0.938	54.748	62.943
G4	0.874	0.830	0.995	17.794	68.685

Note that constants of the found relations are not given as not to tempt them from being implemented in other analyses. This, as they are not generally applicable and as they have no physical meaning besides allowing the best fit between operating conditions and the specific test run for BKD. The same method could be applied to other chambers, but will likely return very different values for these coefficients. Resulting integrated heat flux predictions however, can be found in Appendix C, showing relevant results for this research.

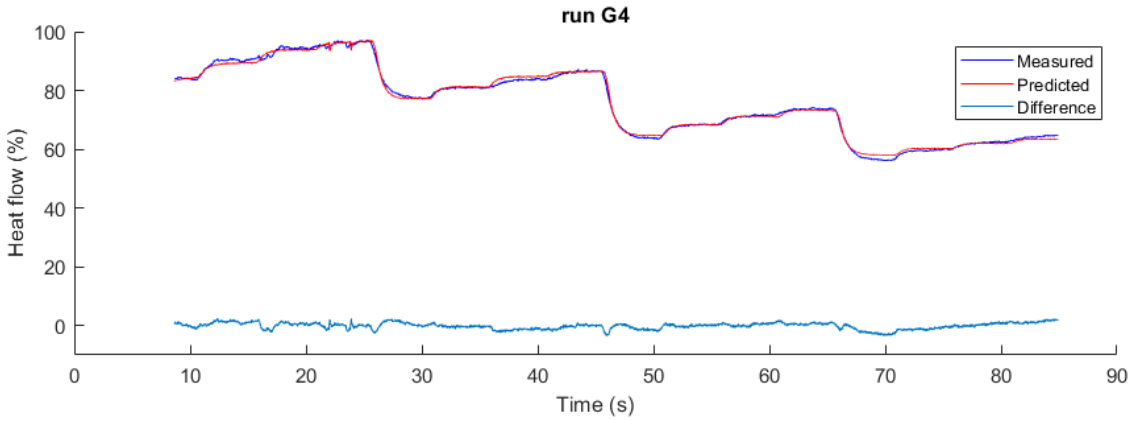

Figure 35: Example result of experimental relation.

4.3 Conclusion on Stable Integrated Heat Flux Prediction

To conclude this section, it can be said that the Bartz equation was successfully implemented in a model that includes an assumed heat flux profile throughout the length of the combustion chamber. However, as the resulting accuracy of the prediction was below the imposed accuracy limit of 5% deviation from experimental data, this method was not continued with.

As a second attempt, a new method was constructed which combines the operating conditions in one simple relation which is fitted to match the experimentally determined integrated heat fluxes. When recalibrated for each experimental test run, it was possible to achieve a mean deviation for each test run which remains below 4% and thus fulfils the wanted accuracy requirement. This method will be used for the rest of this work, as its extrapolation to periods of unstable combustion allows for detecting deviations in heat fluxes due to combustion instabilities. This answers the first research question as stated in subsection 1.2.

5 Predicting Change in Integrated Heat Flux

In this section, the second research question, which asks how changes in integrated heat flux due to combustion instabilities can be explained, is answered. In order to establish a first model that can explain and predict what is being observed in the BKD experiments, it is chosen to start from existing and published theories and to develop a model based on this independent theoretical basis [17]. Finally, this theoretical model will be compared with observations from BKD in order to validate the model and derive an explanation for the observed effects. This methodology allows for development of an unbiased theory regarding increase or change in heat flux and can thus be accepted as a more scientific and reliable approach.

5.1 Interpretation of BKH Results

Experimental relations were determined for BKH for test runs with different but constant operating conditions that determine the effect of shrinking L/D with increasing acoustic pressure amplitudes. These results are presented in Table 2, as elaborated on in Section 2.4.2. These experimental relations are plotted in Figure 36 and although the operating conditions under which they are determined vary, the found relations do not differ by large amounts from each other. It should be noted, however, that BKH has test runs with both sub-and supercritical LOX injection conditions, being respectively those runs with chamber pressures below and those above 50bar as elaborated on in Section 2.5. Considering all injection in BKD happens supercritical, it is chosen to make a differentiation as shown in Figure 36 where only those with chamber pressures above 50bar are considered applicable to BKD.

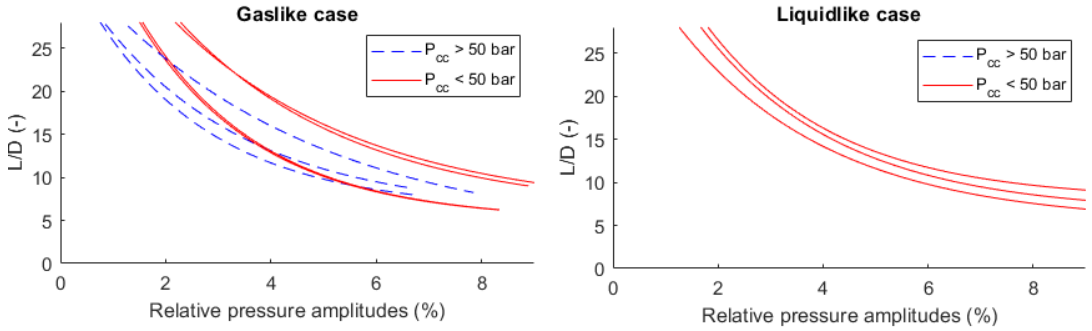

Figure 36: BKH experimentally determined relations.

This returns a number of possible relations that can be used for the gaslike runs, but no run for the liquidlike case. For the gaslike case, the function with highest R^2 value, test 1, is selected from Table 2 given as Equation 47 and used for all gaslike test runs of BKD as the variation between available fit functions is minimal. However, since the variation among the liquidlike curves is minimal, an arbitrary relation with a good fit, test 8, is chosen and will be implemented for all the liquidlike cases of BKD. This relation is presented as Equation 48. Although this is an approximation that is necessary due to the lack of available test runs, due to the general trend being similar between all functions, the relations are expected to still be able to predict the general trend in LOX core length and thus the local heat flux profile throughout the chamber. Note that if more BKH test cases were available, it would be possible to select a relation for each range of operating conditions.

$$\frac{L}{D}_{BKH} = 29.55 \cdot 0.7^{p'_{\%}} + 6 \tag{47}$$

$$\frac{L}{D}_{BKH} = 34.97 \cdot 0.71^{p'_{\%}} + 5.29 \tag{48}$$

As both equations are normalised, they could in the ideal case be directly applied to other combustors with similar properties. However, new insights have been obtained which suggest that the actual cause of a changing $\frac{L}{D}$ is not directly the acoustic pressure amplitudes, rather the transverse gas velocities over the injector plate [43]. These transverse velocities cause the flame to deform and aid in the mixing and break-up of the LOX core.

In this case, the relationship determined for BKH that uses $p'_{\%}$ as the only input parameter cannot be directly applied to BKD, as the same relative acoustic pressures do not necessarily correspond to the same transverse velocities over the injectors due to differences in chamber geometry. The solution to this insight is to investigate the ratio of the RMS transverse velocities in BKH with respect to BKD, corresponding to the same $p'_{\%}$ and scaling Equations 47 and 48 with this factor, into a new relation, presented as equations 49 to 51. However, in order to be able to apply these relations, the transverse velocities of both BKH and BKD over relevant injectors have to be known.

$$\frac{L}{D}_{BKH} = f_{BKH}\left(p'_{\%}\right) \tag{49}$$

$$\frac{L}{D}_{universal} = f_{BKH}\left(p'_{\%} \cdot \frac{V'\left(p'_{\%}\right)}{V'_{BKH}\left(p'_{\%}\right)}\right) \tag{50}$$

$$\frac{L}{D}_{BKD} = f_{BKH}\left(p'_{\%} \cdot \frac{V'_{BKD}\left(p'_{\%}\right)}{V'_{BKH}\left(p'_{\%}\right)}\right) \tag{51}$$

5.1.1 BKH Transverse Velocities

In order to calculate the transverse velocities over BKH, a simple 2D standing wave formula can be used, given as Equation 52. In this equation, V'_{BKH} is the Root Mean Squared (RMS) of the transverse velocity of the gas over one pressure wave period, V_c is the speed of sound in the gas, ρ is the gas density and p' is the acoustic pressure amplitude. The 2D formula is applied due to the purely standing transverse pressure waves being present in the rectangular chamber geometry of BKH which does not allow for rotating waves, as verified with CFD solutions and experimental acoustic pressure measurements [17]. Secondly, no further derivation is necessary, as the placement of the injector of which the LOX core length is measured is central in the chamber, meaning the amplitude of the transverse velocities in the gas at the injector will be the maximum amplitude in the chamber. Both statements are illustrated in Figure 37. [18]

$$V'_{BKH} = \frac{1}{V_c \cdot \rho} p' \cdot \frac{1}{\sqrt{2}} \tag{52}$$

In Equation 52, both V_c and ρ can be calculated using the NASA's CEA program for any combination of operating conditions, as was also utilised in Section 2.2.2 to calculate gas parameters in BKD for implementation in the Bartz equation. However, since Equation 51 is used to calculate the L/D values at BKD operating conditions, no interest is given to the transverse velocities that would occur under BKH operating conditions. For this reason, both ρ and V_c parameters are calculated for the BKH injector locations and chamber modes, but using BKD operating conditions for ROF and chamber pressures. Depending on the operating conditions, typical values for ρ at BKH injector central injector location are between 1.6 and 3.6 kg/m^3, and for V_c between 1600 and 1850m/s depending on the chamber pressure and ROF. The transverse velocities are plotted as a function of acoustic pressure amplitudes for a range of representative operating conditions indicated in the plot, as shown in Figure 38. There is some variation with varying operating conditions, although transverse velocities remain in the same order of magnitude for corresponding acoustic pressures. The transverse velocities are kept as variables which are recalculated for each combination of operating conditions and vary throughout all test runs, while also dependent on the acoustic pressure amplitudes.

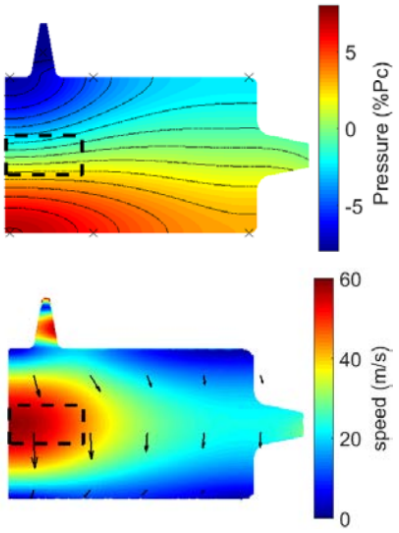

Figure 37: Pressure field and acoustic velocity field in BKH, note the secondary nozzle extention at the top of the chamber and the window of optical access being indicated with the dotted line. [18]

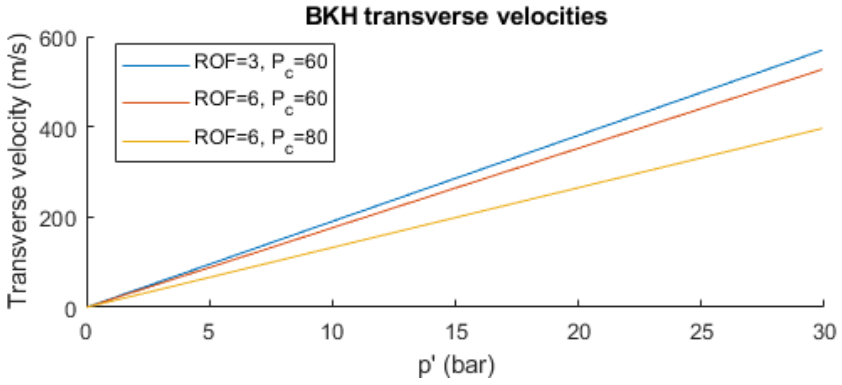

Figure 38: Transverse velocities expected at central injector location in BKH under representative BKD operating conditions.

5.1.2 BKD Transverse Velocities

To calculate the effective transverse velocities acting on BKD, a couple of things must be taken into account. First, since the cylindrical geometry of the combustor allows for rotating waves it has to be identified whether the combustor experiences a standing or rotating wave during the 1T mode. Secondly, the relevant injectors must be identified, as the differences in placement in the injector plate will cause different injectors to experience different velocities.

The differentiation between standing and rotating waves can be based on previous analyses of BKD as described in Section 2.3.3, where an acoustic pressure amplitude larger than 15 bar is consistently found to be rotating and pressure amplitudes below 10 bar to be standing. However, since the experimental data required to verify this statement was available, a short analysis was done by plotting data from the acoustic pressure sensors in the sensor ring. These sensors consist of a set of 8 sensors, equally spaced over the circumference of the measurement ring as described in Section 3.3. Sensor data are loaded for one test run with known 1T mode instability and are plotted for a short time period with identified large amplitude (>15 bar) 1T instability and for a short time period with identified small amplitude (<10 bar) 1T instability, as shown in respectively Figures 39 and 40.

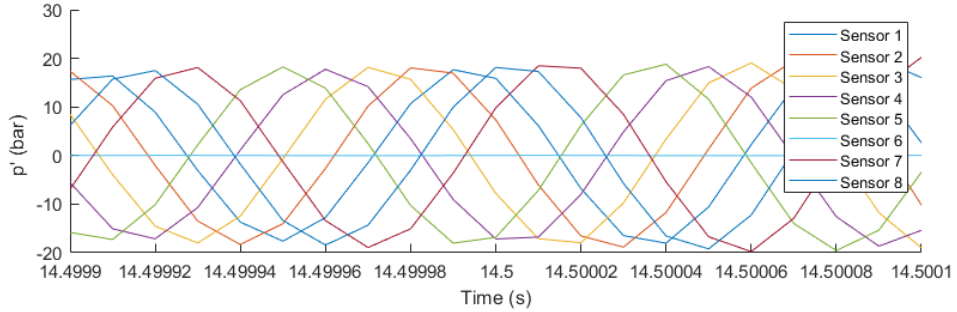

Figure 39: Overlayed acoustic pressure measurements of 1T instability, rotating wave.

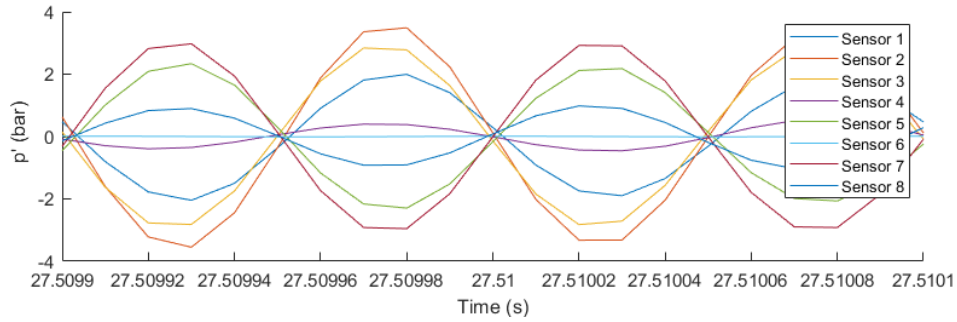

Figure 40: Overlayed acoustic pressure measurements of 1T instability, standing wave.

Note that data of sensor 6 is constant and zero due to sensor failure causing false data readings. However, it can be seen that for the large amplitude oscillations, the 7 remaining sensors all show pressure oscillations of equal magnitude, with each having a phase shift directly related to their positioning on the measurement ring. This indicates a fully non-standing and purely rotating pressure wave. The time period with small amplitudes shows waves of varying magnitude, while sensors placed opposite each other indicate identical but mirrored pressure signals. This indicates a pure standing 1T pressure wave. For this reason, for multiple chosen samples including the presented case, the analysis presented in Section 2.3.3 holds also for the considered experiments. All further transverse velocity calculations with BKD will be performed while assuming a pressure amplitude threshold of 10 bar, being the lower limit for rotating and upper limit for standing waves. A sensitivity analysis regarding this limit is performed in Section 6.3.

Next, the relevant injector elements are identified. As this investigation is regarding heat flux to the chamber walls, the injectors and LOX cores of interest can be defined as those having the most effect on the chamber walls. For two main reasons, these are identified to be the injectors located on the outer injector circle, closest to the walls, as indicated in blue in Figure 41. First of all, this choice is made due to their direct proximity to the wall, while gases being injected through these injectors are more likely to convect heat to the walls. Secondly, since these LOX cores are expected to be longer than the inner ones due to lower local transverse velocities, they are expected to provide at least some level of shielding of the wall from the inner LOX core combustion, decreasing any effects the inner flames might have on the integrated heat flux to the walls. Other injectors indicated in red and yellow are thus not considered for the rest of this research.

To defend the choice for differentiating between injectors closest and those furthest from the walls, numerical solutions of the BKD combustion process have already shown that disturbed LOX cores and flames vary significantly in length depending on their distance from the center of the injector plate, as shown in Figure 42. In this figure, a cross sectional sideview of the chamber is shown, through 4 injectors while the flame of 2 more is visible. Other active injectors are present here although not illustrated. This flame length difference however, means one cannot assume that implementing the average transverse velocity over all injectors to find the LOX core length will return a LOX core length representative of the heat flux profile experienced throughout the chamber length.

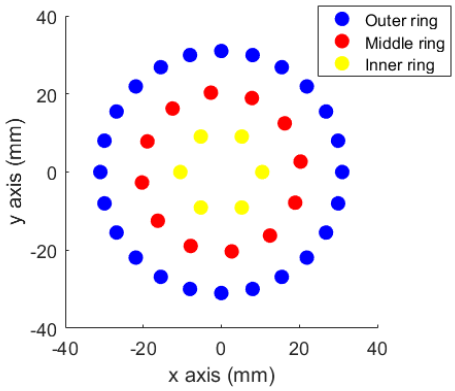

Figure 41: Injector positions on the BKD injector plate.

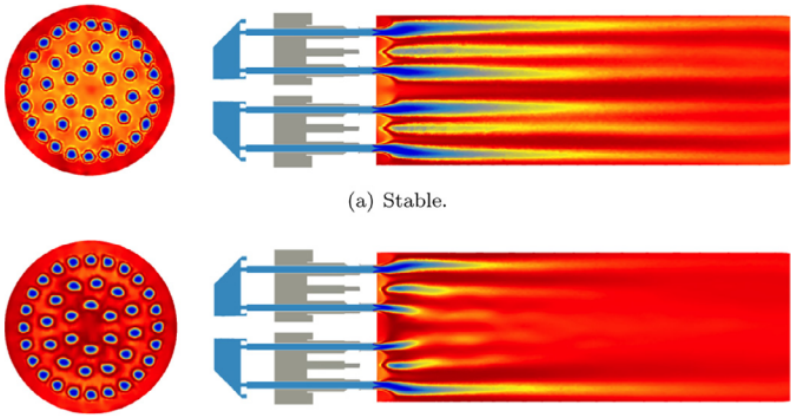

(a) Stable.

(b) Unstable.

Figure 42: Numerically simulated difference in flame structure depending on injector distance from centre of injector plate. [14]

Finally, as a last step to complete the calculation of BKD transverse velocities to be implemented in Equation 51, the transverse velocities at all injector locations can be determined by implementing the velocity field equations described in Section 2.3.2. For comparison with the transverse velocities calculated in BKH, the transverse velocities are plotted as a function of acoustic pressure amplitudes with a chamber pressure of 60bar and ROF of 6. Results are shown in Figure 43. Also the mean chamber velocity is indicated, as to demonstrate the significance and order of magnitude of the transverse velocities with respect to undisturbed gas flows. Note that the jump in velocity at 10bar acoustic pressures is related to the switch from standing to rotating wave models. The effects of defining this threshold at 10bar will be discussed when heat flux profiles are implemented. With the same methodology, transverse velocities can be calculated for each combination of operating conditions as varying throughout test runs, which is done for next steps in this research.

With both transverse velocities in BKH and BKD known, the LOX core length can be estimated for BKD using Equation 51, while results of BKD flame lengths are compared with the numerical solutions for validation. It can be seen that similar flame lengths are returned, thus being a first validation of the model as shown in Figure 44.

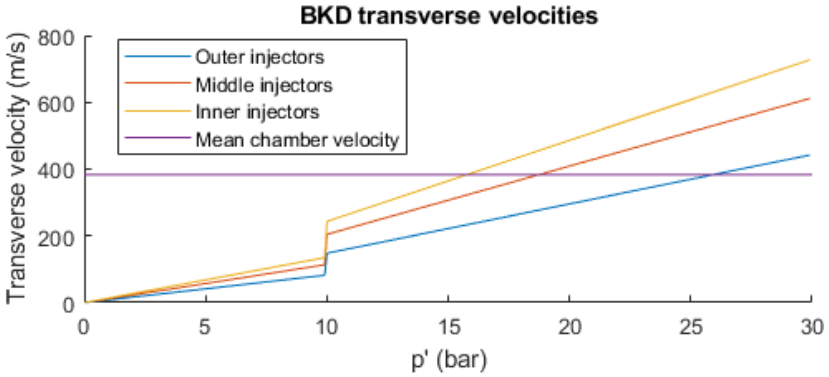

Figure 43: Transverse velocities expected at different injector locations in BKD under representative BKD operating conditions.

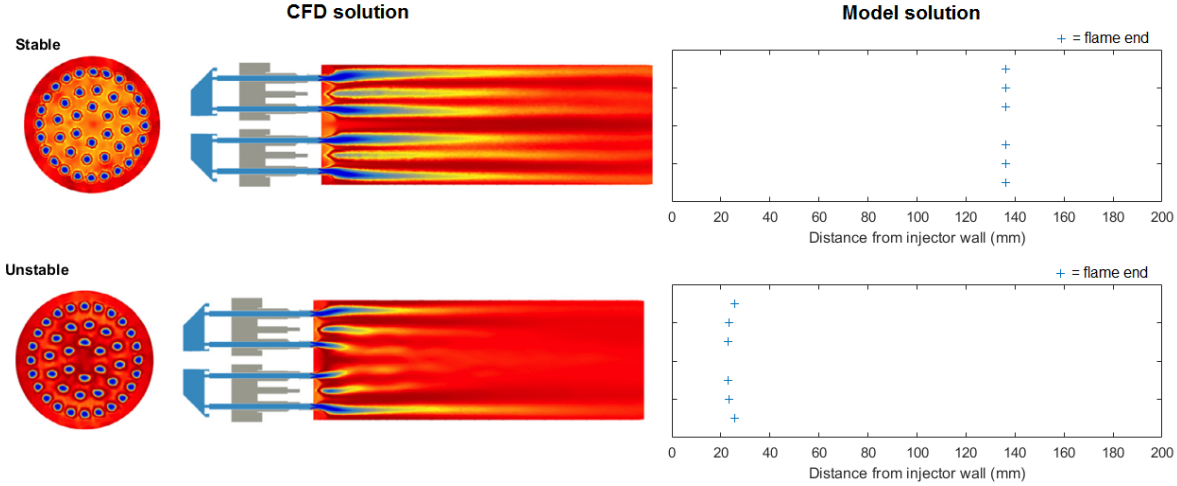

Figure 44: Validation of converted BKH flame length model. [14]

5.2 Implementation of BKH Analysis

In order to implement the results and translation of the BKH research to the BKD combustor for this research, a conversion must be made from LOX core length to integrated heat flux and its relative change with different magnitudes of combustion instabilities. In order to do this, a heat flux profile must be assumed that corresponds to the degree of combustion completion at each point over the chamber length, which in turn can be related back to the length of the intact LOX cores.

5.2.1 From LOX Core Length to Heat Flux

In order to use these LOX core length estimations for this research regarding heat flux to the combustor walls, a conversion must be made. For this, it is assumed that the LOX core length is representative of the point at which it can be said that complete combustion has been achieved, in other words where all gases have been mixed and combusted. This has been verified through numerical analysis performed by Schulze, where oxygen mass fractions are simulated and compared to simulated gas temperatures [15]. The results of these simulations are presented for a number of arbitrary load cases, where bottom half of the flame structure is shown in oxygen mass fractions and the top in flame temperature, presented in Figure 45.

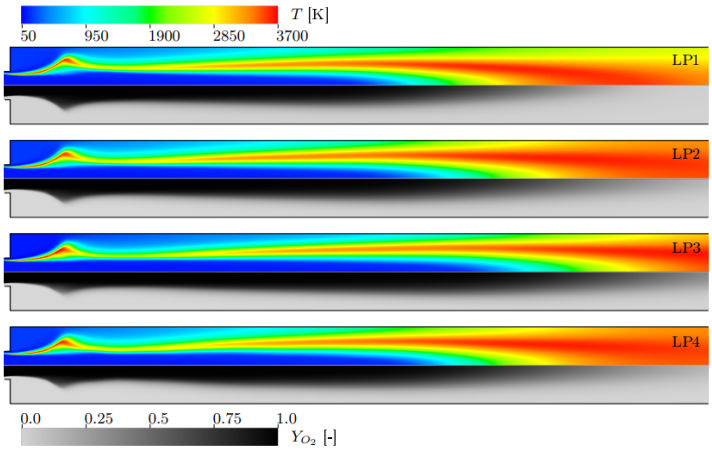

Figure 45: LOX mass fraction (bottom half) compared to gas temperature (top half) for typical load points.

Following from this and referring to Section 4.1.2 in which a heat flux profile was already assumed in order to implement the Bartz equation, a sinusoidal heat flux profile can be implemented over the chamber length, where a steady and constant heat flux value is achieved at the same location along the chamber length at which complete combustion has been achieved. This principle is illustrated in Figure 46 for clarity.

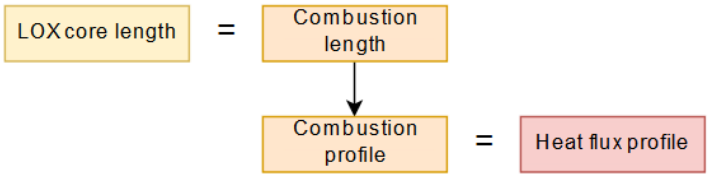

Figure 46: LOX core length to heat flux profile diagram.

In order to complete the profile, only the start value of the local heat flux and the end value are unknown. However, as it is deemed more interesting to investigate relative increases instead of absolute values, the values of these start and end local fluxes are kept as constants and are taken as representative mean values discovered during the Bartz equation investigation in Section 4.1.2. The lower value was found in literature to vary between 0 and $10 MW/m^2$, and the higher values is taken as $35 MW/m^2$ as an average value found using the Bartz equation at completed combustion [12, 52]. The lower local heat flux value is kept as a range due to uncertainty regarding its actual magnitude. To verify this choice of start and end conditions of the heat flux profile, the model is tested for multiple values within the range of start heat fluxes to evaluate whether any values in this range return values in agreement with observations from literature or BKD experimentally determined integrated heat fluxes.

Profiles corresponding to different amplitudes of acoustic pressures are modelled as described and presented in Figure 47. In this example, the acoustic velocities are calculated at ROF of 5 and chamber pressure of 60 bar, being representative of a BKD test run. Note that the profile at acoustic pressures of 0 to about 2 bar show little variation. As explained in Section 2.4.2, this is due to the cut-off point at which effects due to acoustic pressure oscillations no longer add to the effects of already existing turbulence [17, 46].

It can be seen in Figure 47 that the applied model predicts an earlier completed combustion for relatively high acoustic pressures compared to relatively low acoustic pressures, meaning a steeper increase in local heat flux. However, it is necessary to convert these results to something more directly comparable to BKD test results, meaning the local heat flux profiles should be integrated to obtain the overal or 'integrated' heat flux. This is done and results are presented in Figure 48, depicting a relative increase in integrated heat flux with respect to the 0 bar case. It can be noted that the steeper increase in local heat flux corresponds to an overall increase in integrated heat flux with larger acoustic pressure amplitudes.

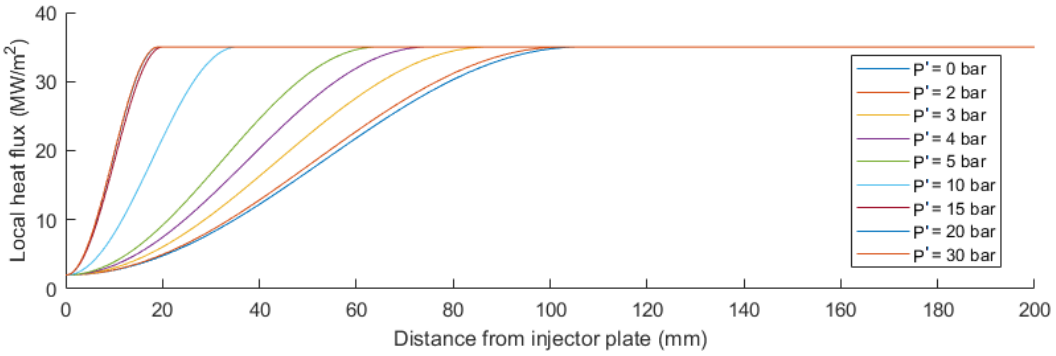

Figure 47: Varying heat flux profiles through BKD combustor at varying acoustic pressure amplitudes.

In this plot it can also be seen how the binary switch between rotating and standing pressure waves for determining relevant acoustic velocities over the injector face plate is implemented, as described in Section 5.1.2. Because no easy solution is available to model the transition between rotational and standing waves, because the best available analysis as shown in Section 2.3.3 shows a more or less instantaneous jump and because results are not expected to improve much through implementing an improved model of this sort, the heat flux curve is left to be non-continuous when switching from standing to rotating waves. Besides, this non-continuity is not expected to cause problems due to the nature of the experimental data where no smooth increases in acoustic pressure amplitudes occur, rather there are extremely quick jumps (in less than 0.002 seconds) between instabilities of different magnitudes. If the threshold is changed from 10bar to 15 bar, only the integrated heat flux within this 10-15bar region will change while showing an increase of maximum 5%.

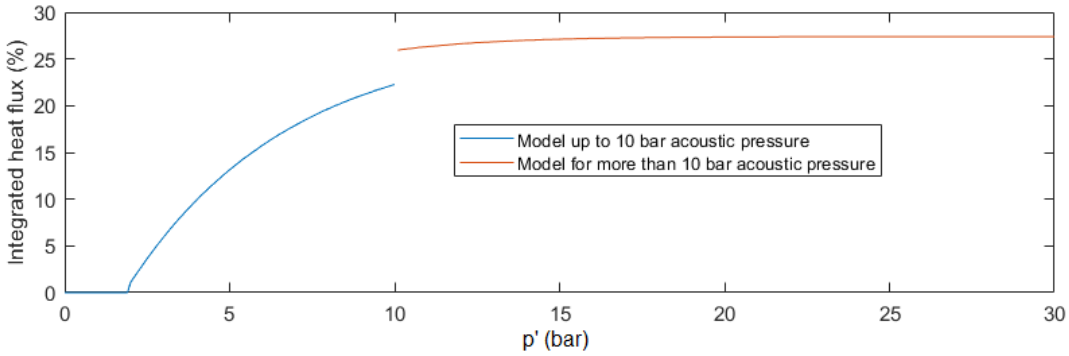

Figure 48: Change in integrated heat flux with varying acoustic pressure amplitudes, chamber pressure of 70bar.

Lastly, as a first verification step of the model, it can be compared with literature presented in Section 2.2.4 which often described how local heat fluxes show large increases of factor 5 to 10 of the steady case near the injector face plate. To extract the local increases in heat flux, the different heat flux profiles corresponding to different instability magnitudes in Figure 47 can be compared to the 0 bar case to find a relative axially distributed increase. Results for the 30 bar instability case are presented in Figure 49 and show an increase up to a factor of 8 near the injector face plate. This is a good match with literature [1,4,11,12,23]. Thus, through the proposed model it has been proven that the integrated heat flux measurements observed in BKD with an increase of 40% are not necessarily in contrast with what has been described in other research and that both results can be reconciled. For this reason, the model can not only be deemed verified with these investigations, but also the described localised heat flux increases in literature can be reconciled with the observed integrated heat flux increases in BKD through implementation of the flame shortening theory of the proposed model. To the authors knowledge, this is the first successful approach that can predict an increase in heat flux due to combustion instabilities.

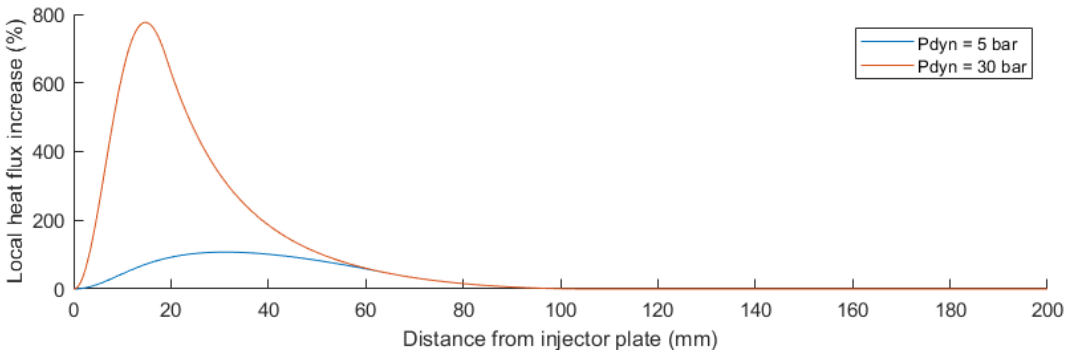

Figure 49: Localised increases in heat flux with respect to the 0 bar instability case.

5.3 Conclusion on Changing Integrated Heat Flux Prediction

To conclude this section, it was found that a previous investigation regarding BKH was extremely useful as it gave experimental relations regarding LOX core length with respect to magnitudes of combustion instabilities. These relations were adapted and modified to fit the injector conditions of BKD into a new model. In this model, LOX core length was used to approximate a combustion profile, which was equated to the heat flux profile.

Adapting a second relation that was experimentally determined for BKH to predict LOX core lengths during stable combustion. Implementing the same methods to determine the heat flux profile from the LOX core length as before, it became possible to find the relative change of heat flux profile between stable and unstable combustion. Integrating these profiles also allowed for obtaining the relative change in integrated heat fluxes.

As a nuance it should be stated that accuracy for these models is hard to determine due to the many approximations that have been made which cannot be verified individually. However, whether this model is accurate enough, will be determined when validating the model with experimental results and with literature in Section 6. Besides, these models are largely based on experimental results from BKH and can thus only be reliably implemented for combustion chambers with similar experimental set-ups regarding the injectors. This means, there must be a similar injector diameter, the propellants are injected in a shear coaxial configuration and for similar injection conditions.

6 Model Sensitivity Analysis

In this section, the major assumptions made in this research are summarised again and their effects on results are defined in a sensitivity analysis. Note that also smaller assumptions are made in some parts of the research, but due to their minor effects they are not restated here. This analysis is performed for the three major sections in this work, starting with experimentally obtained data and how it has been applied. Next, the stable predictions for integrated heat flux are analysed. Lastly, the prediction for changes in heat flux with high frequency combustion instabilities is analysed. Although this chapter does not explicitly answer one of the research questions, it is implicit to the last research question which asks if the model can be validated for a more general case. Here it is stated what limitations there are to the model and thus how general it can be applied. Besides. it is deemed necessary to perform this sensitivity analysis to ensure the scientific value of this work.

The elaboration per assumption has a fixed structure, as to provide clarity. First, the assumption is stated in bold. Second, its implications and a short explanation are given in the same paragraph. Next, a measure of its potential effects and a justification are given. Lastly, in some cases a further implication can be mentionej.

6.1 Assumptions in Experimentally Determined Integrated Heat Flux

A sensitivity analysis regarding the experimentally determined data of integrated heat flux and other measurements are summarised and discussed in this section. This analysis serves the purpose of determining the sensitivity of the used data with respect to inaccuracies in measurements or its interpretation for utilisation in this thesis work. Below, two major assumptions are identified and listed along with their potential effects.

- **The coolant water absorbs all heat that is transferred from the hot gases to the combustor walls.**
  This assumption implies that no heat is transferred from the combustor walls to the injector plate or to the nozzle section which are connected to the main combustor wall.

  The heat flux to the wall is calculated for the combustor segment as a whole, as a measure for integrated heat flux, as explained in Section 2.2.3. For this reason, losses to the nozzle segment and the injector faceplate are included in this integrated heat flux measurement, while no practical measure for these localised losses can be easily estimated. However, in other research which implemented multiple segmented water cooled sections that combine into one combustor segment, a measure for heat flux to different sections of the walls could be found [12]. In these sections, it is found that no significant difference in measured heat flux can be observed between sections close to the injector plate and sections located at the injector plate, nor for those near the nozzle segment. An example is depicted in Figure 6, which shows at least one measurement close to the injector plate which shows the same value as the measurement at the injector faceplate, the same is true for the measurements near the nozzle, as the two closest measurements show no large discrepancy compared to each other [12]. For this reason, it is expected that the losses in BKD will also not be significant and will not affect the measured integrated heat flux in a noticeable manner.

- **No heat is lost from the coolant water to the outside world.**
  This assumption implies that all heat flowing from the gases to the chamber is stored in the coolant water in the form of a temperature raise and thus enthalpy change, while no heat is transferred from the warm water to the outer wall of the chamber that could reduce its overall enthalpy change.

  To estimate the heat loss, convective heat transfer to the air is neglected as there is no air flow expected around the chamber, but mostly stationary air. As for conduction, this is expected to be negligible as the steel chamber case has a coefficient of conductivity which is 10 times lower than that of the material used on the inner wall of the chamber and the coolant channels (copper with conductivity of 30W/mK compared to an inconel alloy with conductivity of 330W/mK) while at the same time having a wall thickness which is much larger than that of the cooling channels [19]. The radiative heat losses from the chamber to the outside world can be estimated in an absolute worst case analysis for simplicity. First, the emissivity ϵ of the chamber material is assumed 1 for simplicity, while in reality it will be closer to 0.7 although some uncertainty exists due to the lack of

information on the chamber for this research. Second, as a worst case scenario, the chamber outer surface area is estimated by taking the outer diameter of the chamber as its maximum of 0.219m, while the actual diameter varies in size throughout the length of the combustion chamber, often being much smaller. Having a length of 0.22m, the total worst case radiating chamber surface area A is calculated to be 0.151m^2. Note that a larger absolute surface area can exist through folds in the surface, although these will have a large viewfactor to other chamber surfaces and will not radiate more heat to the outside world. Next, a worst case wall temperature T_w is chosen, being the maximum of measured coolant water outlet temperature and an outside ambient temperature $T_{ambient}$ is chosen to be 273.15K, being the minimum operating temperature of the test bench (due to coolant water freezing). Taking the Stefan-Boltzmann constant as $5.67 \cdot 10^{-8}$ W/(m^2 K^4), the total radiative heat flux out of the chamber can be calculated as Equation 53. This calculation results in an estimated worst case heat loss of less than 110W, while the lowest possible heat flow of the chamber as can be calculated with parameter ranges presented in Table 15 is more than 500kW. Finally, as the losses amount to less than 0.02% of the measured integrated heat fluxes, this assumption is deemed valid.

$$Q = \sigma \cdot \epsilon \cdot A \cdot (T_w^4 - T_{ambient}^4) = 5.67 \cdot 10^{-8} \cdot 1 \cdot 0.151 \cdot (368^4 - 273.15^4) = 109.6W \tag{53}$$

6.2 Assumptions in Stable Integrated Heat Flux Preduction

In this section, a sensitivity analysis regarding the prediction for integrated heat fluxes during stable combustion is performed. This analysis serves the purpose of determining the sensitivity of the model and the sensitivity of its predictions with respect to inaccuracies in model assumptions. As the model that implements the Bartz equation has been deemed not usable in Section 2.2.2, assumptions made for this section are not further elaborated as they have no effect on results of this thesis work. However, some assumptions that do effect other parts are moved and elaborated in their respective parts. Futhermore, the model described in Section 4.2 is analysed. This model predicts the integrated heat flux based on a manually found relation between stable integrated heat flux data and relevant controlled parameters.

- **The controlled operating conditions of P_c, ROF and T_{H2} can be combined in a power relation given as Equation 45 that predicts integrated heat flux.**
  This assumption implies that no other variables need to be taken into account to achieve accurate integrated heat flux predictions, while the shape of this equation suffices in complexity to represent the heat flux.

  Although other semi-empirical relations as the Bartz equation or other Nusselt equations are taking into account many more parameters such as viscosity and thermal conductivity, these are designed to be generally applicable in as many cases as possible [1]. As the relation made in this research is not meant to be generally applicable and will be recalibrated for each test run, the inclusion of more parameters is not necessarily needed to achieve good predictions. This can be stated as with the recalibrations in place, relations show a mean deviation of less than 5% as shown in Table 15, which is the wanted accuracy as posed in the research goals. This model has been verified per test run, as its coefficients have been recalibrated per test run and are not generally applicable.

- **The calculated acoustic pressure amplitudes represent the magnitude of the combustion instabilities.**
  This assumption implies that combustion instabilities are correctly characterised and can thus be correctly identified based on the criteria that their magnitude is larger than 5% of the chamber pressure as defined in literature [1].

  The method to calculate instability magnitudes is adopted from preceding research on the topic of combustion instabilities [16]. This method is valid for deriving amplitudes of sinusoidal waves. As the pressure oscillations during unstable combustion are known to be sinusoidal waves with a frequency corresponding to the Eigenfrequency of the instabilities, this method is expected to return correct amplitudes, especially during combustion instabilities. However, it was found that the acoustic pressure sensors experience saturation at pressure magnitudes of 30 bar, at which point the measurements are capped off. Due to this capping off, the shape of the waves is misformed and values of more than 30bar are not measured, causing wave amplitudes that are no longer correctly derived and potentially to be seriously underestimated using the RMS method. As there is no

way to reconstruct the real waves without capping off, there is no way to estimate the loss in magnitudes as calculated with the RMS. However, as this is the method utilised by all peers and as no experimental data is present to correct for the data capping off, these potential miscalculations are chosen to be accepted. Besides, as the increase integrated heat flux is found to converge around 15bar as shown in Figure 48, an underprediction of combustion instabilities of for example 35bar as 20bar magnitudes will not change the results by more than 5%, thus even potential miscalculation of magnitudes will not invalidate results of this research.

Besides, changing the threshold in magnitude to define combustion instabilities can effect results of the model that constructs the experimental relations. For example changing this limit to a lower value causes datasets to shrink as data which would otherwise be considered useful are now considered unstable. If the limit would be made larger, it could be that experimental heat flow values are used to fit the function which are not representative for stable combustion as they are affected by combustion instabilities. This would cause the found relation to be less useful to predict data for stable combustion. No numerical examples can be given to quantify these effects as they have not been further investigated, as changing the limit is not expected to improve results and the limit is generally agreed upon in literature [1].

- **The exclusion from the integrated heat flux measurements of time periods at which there are combustion instabilities or transient operating conditions with some time margin, ensures the presence of non-varying and thus steady integrated heat flux measurements.**
  This assumption implies that the steadiness of heat flux measurements corresponds to steadiness in operating conditions and acoustic pressures. Besides, it assumes that transients in operating conditions and combustion instabilities occur simultaneously or with a relatively small time margin, with changes in integrated heat flux.

  To investigate the validity of this assumption, one can visually inspect the time series of both events as presented earlier in Figure 32, Figure 33 and Figure 34. It can be seen that time periods of unsteady combustion are largely removed, with removal of time periods at which operating condition transients and instabilities occur. However, there are some smaller time periods at which there are still unsteady or slowly changing integrated heat flux values due to the threshold values at which transients are identified. Luckily, heat flux prediction relations found with these data sets were accurate enough for the wanted purpose, showing a mean deviation below the imposed maximum inaccuracy of 5%, as shown in Table 15 and thus they are considered sufficient for usage in this research.

  Besides, the mentioned threshold values have been optimised manually by reducing and increasing the thresholds and evaluating their effect on the resulting remaining dataset. Varying the thresholds around the found optimal values resulted in either data sets that included more transients and were thus less representative of steady combustion or datasets that showed removal of steady data due to the oversensitive filtering algorithm. In both cases, the datasets were less useful for finding the relation, thus it was chosen to accept these remaining transients.

- **The relation found between operating conditions and integrated heat flux values can be used to predict values of stable integrated heat flux during periods of combustion instabilities.**
  This assumption implies that the relation between operating conditions and steady integrated heat flux is constant throughout the whole test run and can thus be extrapolated to periods where no steady experimental integrated heat flux values are available.

  Although larger deviations are present in predicted heat flow with the experimental values during periods of stable combustions and reaching up to 20% for short time periods, almost all of these occur during periods of transient operating conditions as can be seen for each test run in Appendix C, while the mean deviations always remain below 5% for all test runs as shown in Table 15. For this reason, it not unreasonable to expect the prediction to deviate with a mean of less than 5% from ideal values of integrated heat flux during time periods of interest, being those of steady combustion.

6.3 Assumptions in Heat Flux Change Prediction

In this section, a sensitivity analysis regarding the prediction for changes in integrated heat fluxes during unstable combustion is performed. This analysis serves the purpose of determining the sensitivity of the model and the sensitivity of its predictions with respect to inaccuracies in model assumptions.

- **The experimental curves obtained for BKH regarding acoustic pressure amplitudes and LOX core lengths can be applied to BKD, while only scaling the acoustic pressure with the ratio of acoustic velocities over the relevant injectors.**
  This assumption implies LOX core break-up for shear coaxial injection with comparable operating conditions is dependent only on the LOX core length for stable combustion and transverse velocities imposed on the LOX core.

  Considering the LOX core shortening estimates, the difference in momentum flux ratios between BKH and BKD is not expected to influence the break-up characteristics as a function of acoustic pressure amplitudes. This can be said, since even while varying BKH operating conditions as shown in Table 2, the resulting best fits are visually similar as shown in Figure 36. This similarity is also expected to apply to BKD, while it is expected that at least the trend of LOX core shortening with increasing acoustic pressure amplitudes applies. This has also been validated using numerical FEM solutions [15]. Besides, it can be seen in Figure 36 that, at least for the curves for supercritical LOX injection, all curves converge to L/D values between 7 and 9. This variation has been implemented in a verification calculation and resulted in a change in prediction of increase in integrated heat flux of no more than 0.4%. This potential error cannot be remedied with available data and is thus accepted.

  As for the transverse velocities effecting the LOX core break-up, it is expected that it is the changes in transverse momentum (scaling with transverse velocities) of the gases, rather than the transverse pressure oscillations that affect the LOX core break-up [18]. This can be visualised as a physical transverse 'shaking' of the LOX core in the combustion chamber, which rips apart the core and forces mixing with the coaxially injected hydrogen. As combustion instabilities of the same magnitude do not correspond to transverse velocities of the same magnitude, it was deemed necessary to correct the input to the BKH curves so that the resulting LOX core length will represent BKD more accurately.

- **The stable LOX core length predictions based on the momentum flux ratio accurately represent the LOX core length during stable combustion.** This implies that experimental relations calculated using BKH experimental data also apply to BKD, for which the curves are used to predict the LOX core length.

  The predicted stable LOX core lengths are based on experimental relations determined for BKH, with only momentum flux ratios as input parameter [36]. In literature there are multiple semi-empirical correlations available for calculating the LOX core length during stable combustion, all depending on injector geometries and chamber operating conditions [46]. However, as the injector geometry of BKH and BKD are identical and the range of operating conditions are similar, the experimental curves as modified to fit BKH experimental data are preferred over complex semi-empirical correlations. These return LOX core lengths that correspond to the numerically found solutions [15] and thus the assumption is validated. However, it is also known that the LOX core length is slightly shorter than the combustion length, as some combustion still occurs further in the chamber than where complete mixing has occurred. However, as no concrete distances for this can easily be calculated, it is chosen to keep LOX core length as combustion length.

  This assumption in particular can effect change in integrated heat flux with combustion instabilities. In case the stable LOX core length is increased from 0.09 to 0.11m, the change in integrated heat flux with combustion instabilities increases by 8%, while lowering the stable LOX core length from 0.09 to 0.07m causes the predicted change to decrease with 6%. These estimates do not vary by more than 1% over a combustion instability magnitude ranging anywhere above 5bar, below which there is often no reported change in heat flux depending on the stable LOX core length. Thus, if the estimated LOX core length is too short, the potential increase in integrated heat flux due to LOX core shortening is decreased and limited. The opposite is true for LOX core lengths which are estimated too long during stable combustion. If final values in change of integrated heat flux deviate from experimentally determined values, this is a likely cause of discrepancy.

- **BKH transverse velocities are purely 2D and magnitudes can be estimated using a 2D standing wave formula.**
  This implies that no 3D effects take place in BKH, which largely simplifies the transverse velocity calculation.

  This assumption has been verified by comparing calculated transverse velocity magnitudes at different acoustic pressure magnitudes, with numerical solutions presented in literature [18]. Found discrepancies emain below 0.1% and thus this assumption is deemed valid.

- **The switch between standing waves and rotating waves in BKD is instantaneous and discontinuous.**
  This implies that transverse velocity fields in BKD can be assumed to correspond to purely rotating waves when pressure magnitudes are above 10bar and purely standing waves when below 10bar.

  This assumption was made after inspecting pressure sensor data as elaborated in Section 2.3.2 and although in most cases this is true, the switch is not instantaneous. However, as very little data is present for instabilities in the 10bar range, the considered acoustic pressure magnitudes fall well within the standing or rotational ranges with very little data point being close to the switching range. For this reason, the non-continuous switch will not have any significant effect on the results and can thus be made without invalidating the model. If the threshold is changed from 10bar to 15 bar, only the integrated heat flux within this 10-15bar region will change while showing an increase of maximum 5% over the relevant range of operating conditions as defined in Table 4. For this reason and considering the threshold lays somewhere in this 10-15bar region, this assumption does not have a large influence on the final results of the model.

- **The combustion profile of the outer injectors is representative for the heat flux profile to the combustor walls.**
  This implies that the outer 24 injectors dominate the heat flux profile, while the inner flames with different combustion profiles do not have to be taken into account.

  Considering the outer flames are longer than the inner flames, it is expected that the uncombusted gasses of the outer flames 'shield' the combustor walls from the inner flame and any heat released because of its combustion. As there is no information on the real profile of heat flux into the combustor walls, there is no experimental data available to validate this assumption. However, the difference in length between inner and outer flames is estimated less than 10mm during the strongest combustion instabilities, as shown in Figure 44. For this reason, in the worst case, when the stable flame length is around 90mm (as is the case for most test runs), the outer unstable flame length is around 25mm, the initial heat flux is its lowest possible value of 0MW/m^2 and the final value is 35MW/m^2, being a representative value as can be calculated with the Bartz equation, as performed in the example calculation in Section 4.1, the relative increase in heat flux would increase from 21% to 25%, as calculated with methods described in Section 5.2.1. As the relative increases seen in experimental data are much larger (+40%), this error could explain some of the deviation in prediction with respect to the experimental observations, although not completely. As the main deviation is expected to be due to other effects however, it is chosen to keep this assumption.

- **The LOX core length represents the combustion length, from which an axial distribution of local heat flux can be derived.**
  This implies that there is completed combustion at the same instance as there is a break-up of the LOX core and thus mixing of the gases.

  It is likely that the LOX core is shorter than the length at which completed combustion occurs. However, as no practical measure of this difference exists, there is no arguable way to implement this. As a consequence, the estimated stable combustion length can be slightly shorter than the real combustion length. At the same time, it is expected that this effect is less during large amplitude transverse combustion instabilities, due to the increased mixing effect it has on the combustion gases through imposing transverse moments on the flow as has been visualised in video footage for BKH [17]. For this reason, the combustion length during combustion instabilities will also be underestimated, although not as much as during stable combustion. The combination of these two factors will likely cause an underprediction of decrease in combustion length and thus an underprediction of relative increase in integrated heat flux. Although no attempt is made at quantifying and implementing the error in flame length in this work, due to the lack of verifiable estimations, a quick estimate is made of how much the estimated integrated flame length can change. First, the

flame length at stable conditions is taken as 90mm, as is the average as estimated for the LOX core length, while the flame is actually 110mm long, being the flame length as sometimes whitnessed in numerical solutions [15]. Acoustic pressure oscillations with magnitude of 25 bar are applied, resulting in an estimated integrated heat flux that raises from around 21% to around 29% for the two respective flame lengths, under chamber conditions of 80bar and ROF of 6. Similar results were obtained for other operating conditions.

6.4 Conclusion on Sensitivity Analysis

As a conclusion it can be put that although this research uses best available methods and approximations for almost all aspects of the model, these approximations are often unverified as individual components and can thus cause inaccuracies in the final result of this model. These inaccuracies have been approximated in as far as possible and showed that there are no risks to the validity of the results of the model as the predicted increases will still be in the same order of magnitude. However, the number of approximations make it very hard to find the accuracy of the final result of predicted increases in integrated heat flux.

It has also been found that the most influential approximation is that of the LOX core stable length prediction. A change in this from 0.09 to 0.11m has been shown to cause a potential difference in predicted integrated heat flux increase of up to 8% and is thus the parameter with the most influence on final predictions. Other assumptions introduce potential inaccuracies, but these are of lesser magnitude.

7 Experimental Analysis and Results

In this section, the third research question, which asks how a model can be validated for a more general case, is answered. To do this, the results obtained while predicting the integrated heat fluxes during stable combustion are combined with the model constructed to predict changes in heat flux with high frequency acoustic pressure magnitudes. This is done in multiple ways, each aimed at validating the model, as to prove that the theory behind it can be backed up by experimental data. First, deviations of the fitted integrated heat flux functions with experimental data are assumed as changes in heat flux not related to chamber operating conditions, but due to combustion instabilities. This change in integrated heat flux is compared with the model in Section 7.2 to see if deviations match those predicted by the model and can thus be explained. Next, indirect results obtained from analysing the heat flux predictions of the Bartz equation and evaluating which heat flux anomalies correspond to time periods with known combustion instabilities is also done. These manually identified anomalies are also compared to the model in an effort to validate the model in Section 7.3. Results of the experimental analysis are presented in Appendix D for all available test runs.

7.1 Model Comparison with Literature

In Section 2.2.4 which reports on known effects of combustion instabilities, it has been found that increases in heat fluxes are often observed during periods of combustion instabilities. These increases are mostly reported as local increases of heat fluxes near the injector face plate.

The reported local increases of heat flux reach magnitudes between 3 and 10 times the heat fluxes during stable combustion. When modifying the model to allow for analysis of local heat fluxes and their relative changes as was explained in Section 5.2.1 and depicted in Figure 49, it was found that the model can predict local increases of heat flux of up to 800% or 8 times the stable local heat fluxes. This is considered a nice consolidation between the constructed model and literature, thus the model is considered validated in as far as possible with the reported observations in literature.

7.2 Model Comparison with Correlated Heat Flux Prediction

In order to apply the integrated heat flux time series found for multiple experimental test runs to the model constructed in Section 5, some steps are necessary. In Section 4.2, a correlation is found between experimentally determined integrated heat fluxes and the operating conditions in the combustion chamber. To find a measure for deviations in heat flux, the experimentally determined heat flux is subtracted from the predicted heat flux with the correlation and normalised with respect to the predicted stable heat flow to obtain the relative integrated heat flux change. Any positive deviation of integrated heat fluxes (an increase) is represented by a positive percentage of relative integrated heat flux increase. An example of this result is indicated in Figure 50, where large deviations (+30%) in heat flux already seem to visually correspond to large 1T acoustic amplitudes.

In order to better depict this correspondence, deviations in heat flux are plotted over the acoustic pressure amplitudes at each respective point in time in order to create a plot and to enable detecting any trend. The resulting plot for test run L1 is presented in Figure 51, as this run contains the longest and most pronounced combustion instabilities and thus returns the most data points in unstable conditions. In order to narrow down deviations in predicted heat flux to actual changes in heat flux however, some smart data filtering was applied.

First, the acoustic pressure data is bandpass filtered to show only magnitudes of pressure oscillations between 9-12kHz, being the frequency range in which the 1T instability mode can occur as defined in Section 2.3. This can be done for the given test runs as it is known that the 1T mode is the major instability mode affecting the gases, while other frequencies such as the low frequency oscillations only contribute to noise in the sensor data without affecting the flow and thus the heat flux. Secondly, periods of transient operating conditions are identified with methods elaborated on in Section 4.2.2 and removed from the dataset, while periods with combustion instabilities are kept. This is done, as transient conditions are of no interest to this research. It can be noted that there is still a small vertical column of data points at an acoustic pressure amplitude of 0bar and a horizontal spread of data points at a relative

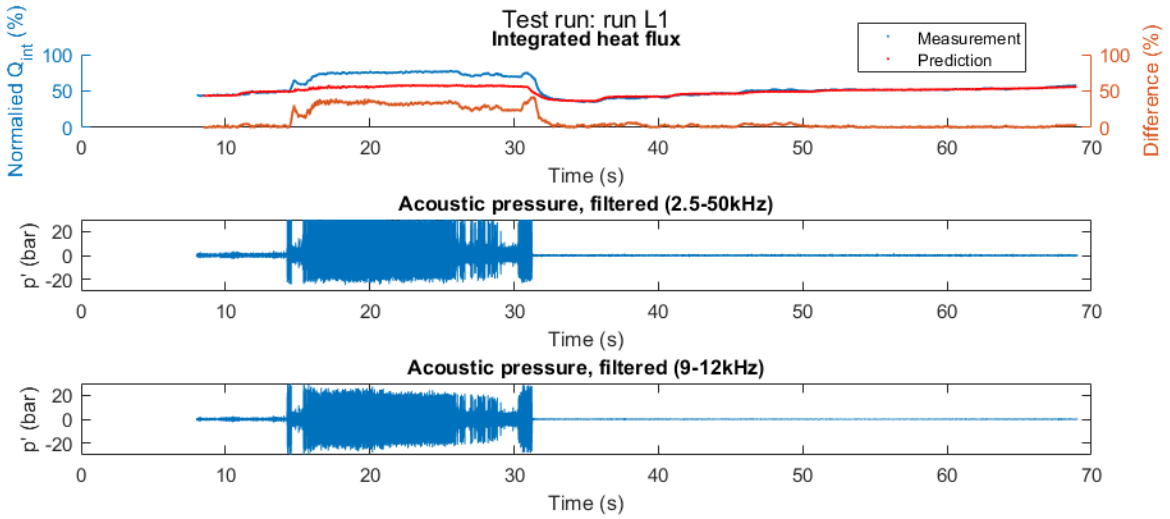

Figure 50: Relative integrated heat flux increase.

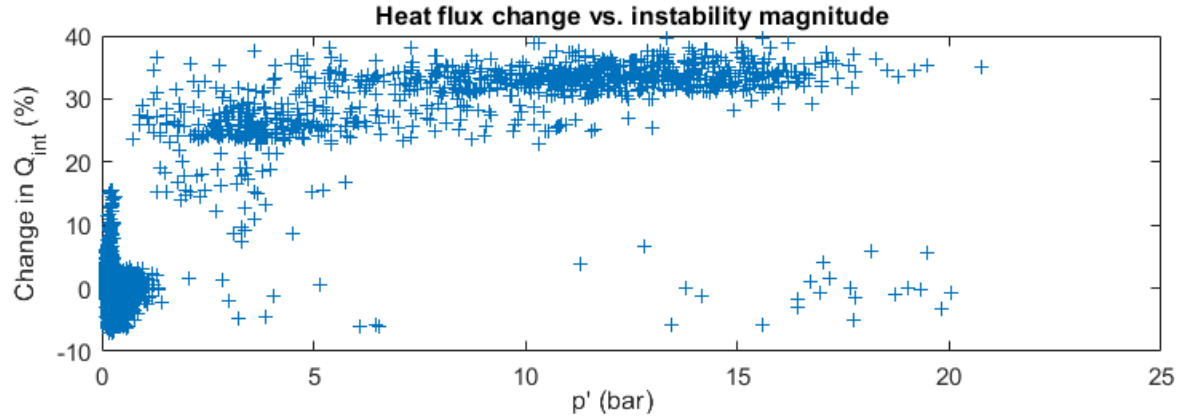

Figure 51: 1T filtered acoustic pressure amplitudes for test run L1, excluding transient time periods.

heat flux increase of 0%. Both can be explained by a time lag and spread of the integrated heat flux with respect to the combustion instabilities as explained in Section 4.2.2. Another explanation is due to inaccuracies in integrated heat flux prediction with respect to the experimental data, where a small deviation does not necessarily mean there is an actual increase or change in integrated heat flux. None of these effects and thus outlying data points disprove the validity of any model, although they cannot be easily isolated without removing much of the experimental data. For this reason they are kept in the data set with resulting model misfit being accepted.

If other acoustic modes were present with the same order of magnitude in oscillatory energy, the model would have to be expanded to also include these effects (if present). However, as there are no BKH or other experimental test data available that includes effects of other acoustic chamber modes on heat flux, implementing any potential effects would be difficult if not impossible with current knowledge. Besides, it has been mentioned in literature that other modes (longitudinal modes) usually do not accompany heat flux increases of the same order of magnitude and as no other instability modes have been detected in Section 3.1, there is expected to be no error of the current model with given test runs for this reason [6].

To compare the model constructed in Section 5.2 to this prepared dataset allows for validation of the model. In order to do this, the acoustic pressure amplitudes at each time step correspond to a predicted flame length, which in turn corresponds to a predicted integrated heat flux. This prediction is normalised with respect to the predicted heat flux of the model with no acoustic pressure amplitudes and a predicted 'change' in heat flux is obtained. This relative change in heat flux is plotted for each time step, together with the experimentally determined change in heat flux of these time steps, so that prediction and

experimental data can be compared. This comparison is presented in Figure 52, having model fit with R^2 value of 0.53599 to the data of this particular test run and an RSE of 9.03%. Although the magnitude of the predictions is lower than the measured values, causing the low R^2 value, its time profile shows a clear correspondence with experimentally determined increases in heat flux with predicted increases in heat flux. The model has been implemented for all available test runs, results of which are presented in Appendix D, including a discussion of each case.

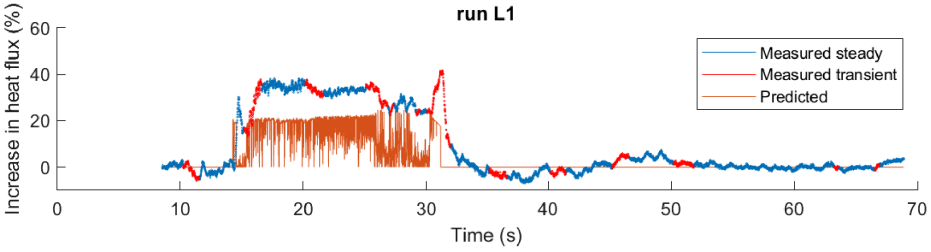

Figure 52: Experimentally determined increases in integrated heat flux compared to model, transients in operating conditions are not relevant for this research.

Finally, with presented results in Appendix D, it can be said that the model returns good predictions of trends in integrated heat flux increases over time for the run with longer (>2s) and large amplitude (>15bar) combustion instabilities. The magnitudes are generally underpredicted by around 10% for this run, although this leaves room for other effects such as thermal boundary layer destruction or increased convective flows and heat transfer due to large amplitude transverse velocity fields of same order of magnitude as the mean chamber flow. Other test runs show no observable increase in integrated heat flux, although for these runs the time duration of the combustion instability is very short (<0.5s) or the magnitude of combustion instabilities is relatively small (<10bar) and thus it is expected that these combustion instabilities did not allow for effects in integrated heat flux to be sufficiently developed to be observed. If more test data was available of long duration large amplitude combustion instabilities, it is recommended to also use this test data to further validate the model, although the described match with the available test run is considered sufficient for this research.

7.3 Model Comparison with Manually Identified Heat Flux Deviations

As automated comparison with the experimental data requires the heat flux changes to occur simultaneously with the combustion instabilities, not always a good prediction is made. However, this is no reason to disregard the model, as there are other data analysis methods available which are not automated. A second method of evaluating how well the model constructed in Section 5.1 can predict the experimentally determined increases in heat flux, is by manually identifying anomalies in experimentally determined heat flux and comparing those results with the model. To clarify, although magnitudes of heat flux predictions made using Bartz' method sometimes show large errors as mentioned in Section 2.2.2, one can use these predictions to realise the integrated heat flux to the chamber walls has a constant magnitude when operating conditions (ROF, chamber pressure and hydrogen inlet temperature) are kept constant in the test run. Thus, when a peak or drop in integrated heat flux is present when operating conditions are constant, this could be considered an deviating heat flux measurement. When this deviating heat flux detection coincides in time (plus or minus 0.5 seconds delay or spread as mentioned in Section 4.2.2) with a registered high frequency combustion instability, this indicates a causal relationship due to the lack of other factors. The magnitude of the integrated heat flux deviation can be determined based on Bartz predicted values when these predictions have low error (< 5%) at the relevant time period or can be based on experimentally determined heat flux values of the same run with the same operating conditions when a time period is present without these high frequency combustion instabilities to compare with.

An example of identified heat flux deviation is given in Figure 53, where it can be seen that operating conditions of ROF and chamber pressure are constant in the period of 12 to 15 seconds. In the hydrogen inlet temperature, there is a small peak of 2K around 14 seconds in the test run, although this increase is not significant enough to cause any heat flux increases of the observed magnitude (as derived from the Bartz equation). The heat flux shows a 22.7% relative increase over a period of 0.5 seconds. This increase occurs with a delay of about 0.5 seconds with respect to a large peak in measured acoustic pressure amplitudes at around 14 seconds.

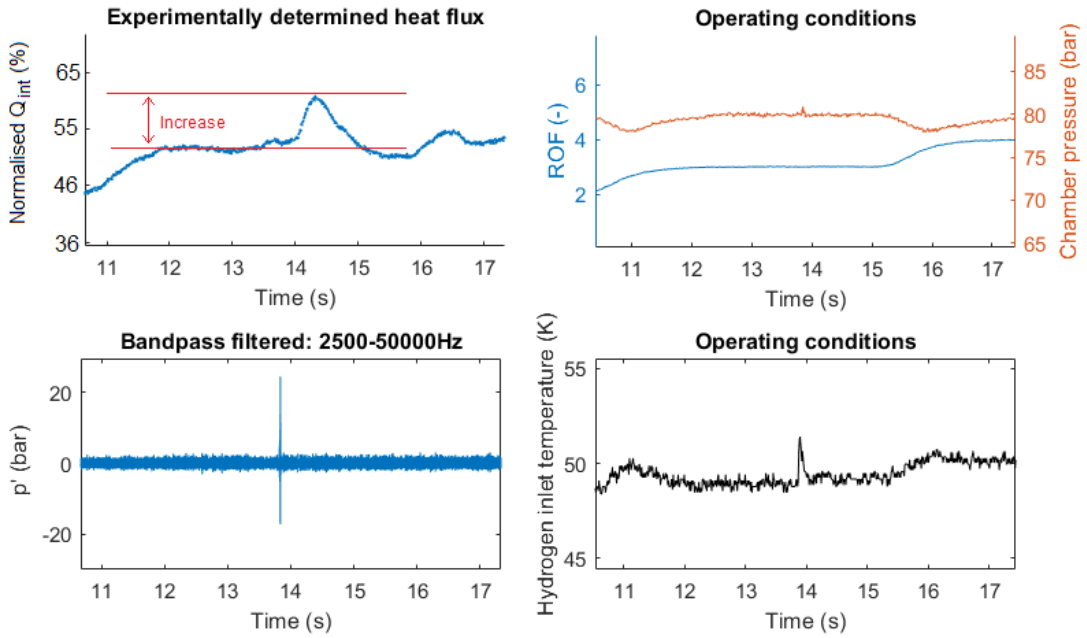

Figure 53: Manually identified heat flux deviation, increase of 22.7%.

A similar analysis is performed for all other available test runs, results of which are presented in Table 16 and can be verified with data given in Appendix C. When no combustion instabilities are present, the test run is not mentioned. Each period of unstable combustion is noted as one data point, while the acoustic pressure magnitudes are those of the filtered 1T mode, as to enable comparison with the model. In the table the acoustic pressure amplitudes, A, the duration of the instability, the observed increase in integrated heat flux, the ROF, the chamber pressure, the hydrogen state of liquidlike or gaslike, the predicted increase in integrated heat flux and the difference between prediction and observed change in integrated heat flux is shown. The state of the inlet hydrogen although supercritical, is divided into hydrogen with liquid like properties (LH) or into hydrogen with gaslike properties (GH) as elaborated on in Section 2.5.

Table 16: Results of manual heat flux increase detection.

Test run	A (bar)	Instability duration (s)	Change (%)	ROF	P_c	Hydrogen	Predicted change (%)	Misprediction (%)
L1	30	0.5	30.1	3	70	LH	22.9	7.2
L1	25	10	34.5	4	70	LH	22.9	11.6
L1	20	5	26.4	5	70	LH	22.8	3.6
L1	28	1	41.4	6	70	LH	22.9	18.5
L2	19.8	0.02	25.4	6	80	LH	22.5	2.9
G1	8	5	0	6	80	GH	10.7	10.7
G2	6	5	0	6	80	GH	7	7
G3	20.5	0.2	0	6	80	GH	21.9	21.9
G3	21	1	0	6	80	GH	21.9	21.9
G4	20.5	0.1	0	6	80	GH	21.9	21.9
G4	20.4	0.1	0	6	80	GH	21.9	21.9

It can be seen that, for the runs with liquidlike hydrogen, the prediction is generally accurate, except for one underprediction and one predicted increase in heat flux when there is no experimentally found increase. However, for the gaslike cases there is no large amplitude (>15bar) combustion instability prediction that matches the observed heat flux effects. Note that in these cases, there are no observed effects or an observed small decrease in heat flux, where the model predicts a significant increase. However, it should be noted that all of these combustion instabilities are of very short time duration (<0.3s) and although the model predicts an instantaneous increase in heat flux, in reality this increase is already observed to have a relatively slow response (>0.5s before reaching its final amplitude). For this reason and matching results found in Section 7.2, the discrepancies are not necessarily disproving the validity of the model. Also for this comparison, it is recommended that once more data is available on test cases with long duration and large amplitude combustion instabilities, these are included to provide a more complete validation of this model.

7.4 Conclusion on Experimental Analysis

In this section an attempt was made at answering the third research question, on whether the model can be validated. To do this, first the model constructed in Section 5 is applied to the available test runs so that they can be compared. Secondy, they can be compared with both literature and with experimental data obtained in Section 4.

To conclude, both the comparison with literature, which allowed for comparison with the magnitudes of predicted increases in local and integrated heat flux, and the comparison with experimental data, which allowed for verification of integrated heat flux trends over time, showed that the model holds for the relevant test cases. For this reason, the model can be considered validated with both attempted methods and the last research question has been answered.

8 Conclusions

In this section, the completed work is summarised as to provide a clear and concise overview of how and in what measure the research objective was completed. To do this, first a general conclusion is posed in Section 8.1 which concludes on the overall results of this research. Next, a more in depth conclusion for each of the research questions is given in Section 8.2. Lastly, a summary of the work performed in order to achieve these results is given in Section 8.3.

8.1 General Conclusion

The overall goal of this work was to enable prediction of heat flux changes based on magnitudes of high frequency combustion instabilities. To understand the difficulty, but also novelty of this research objective, it should be stressed that there have been no other models which were successfully validated for predicting changes in heat flux due to combustion instabilities.

This goal has been successfully achieved in the form of a newly constructed model that implements the novel theory of flame shortening during high frequency combustion instabilities. With the flame shortening comes an earlier achieved completed combustion and thus an increased localised heat flux near the injector face plate. This local increase in heat flux can reach magnitudes up to 800% of the stable heat flux. When integrating the heat flux profile to obtain the overall heat flow into the combustor walls, the obtained model predicts a maximum increase in integrated heat flux over the chamber length for BKD of around 25%, depending on the operating conditions. For this reason, the model can at least partially explain the observed changes in overall and local heat fluxes during combustion instabilities.

Not only has the model been constructed, it has also been successfully validated using both experimental data and observations reported in literature as further explained in Section 8.2.

8.2 Conclusion of Results

In this Section, the results of this research are presented. In order to do this, the research subquestions are reposed as presented in Section 1 and each is answered individually based on what has been discovered in this work. The combination of these answers should provide the fulfilment of the research goal.

How can changes in integrated heat flux due to combustion instabilities be determined? First, the integrated heat flux, as expected during stable combustion, can be predicted using both semi-empirical relations such as the Bartz equation, but also through purely experimental relations that take into account less parameters, but require to be recalibrated per test case.

In this research it has been found that the method which implemented the Bartz equation did not provide results useful for this research. This is mainly due to the lack of knowledge on gas properties as varying throughout the chamber length. The new method which implements a purely experimental correlation however, returned much more accurate results (<4% error with experimental data). This method implements an equation with a very simple shape, being dependent only on the operating conditions, being chamber pressure, ROF and injection temperature of the propellants and is thus easy to implement with limited data on gas parameters. On the downside however, it contains no parameters to represent the chamber geometry, nor parameters to represent the flow of the gas. For this reason, the found relations are not generally applicable and have to be recalibrated, not only for every combustion chamber, but also for every test run.

How can changes in integrated heat flux due to combustion instabilities be explained? Through evaluating the results of investigations that have been performed in the past regarding BKH, it has been found that a relation exists to relate combustion zone length with pressure oscillation magnitudes for BKH. This existing relation has been modified in this research and implemented in a new model constructed to apply to BKD. This combustion zone length is one parameter that affects the heat flux to the combustor walls throughout its length, following from which a measure of change in integrated heat flux with combustion instability magnitudes has been found.

How can a model be validated for a more general case? As no mention is made in literature of integrated heat flux over the chamber length, a validation is attempted based on predicted changes

in localised heat flux. The found magnitudes match what is found in literature, which reports increases anywhere between 3 and 10 times the original local heat flux. Besides, literature describes destroyed injector face plates or combustor wall melting near the injector region, while no such observations are made in aft sections of the combustor. This also matches the predicted localised increase in heat flux near the injector face and thus the constructed model can be consolidated with literature.

Secondly, when comparing to the experimentally determined changes in heat flux in BKD, the model returns good results. First of all, there is only one test run with a sustained (and thus steady) (>2 seconds) large amplitude (>20bar) combustion instability, while others show combustion instabilities which only appear instantaneously or with small magnitudes (<10bar). As for the other observations, these are not considered for the validation of the constructed model, due to the extremely short duration of the combustion instabilities, or their low amplitudes. During the steady large amplitude combustion instability, the model returns a trend in integrated heat flux which matches the increases in experimentally determined integrated heat flux very well. However, when considering the magnitude of the prediction of 22.5%, there is an underprediction in increased heat flux, as the experiment shows increases up to 37%. This is considered a good result, being a conservative prediction that leaves room for other effects which might be taking place.

For this reason, the constructed model is considered the first validated model which can not only partially predict, but also explains increases in heat flux, both overall and localised near the injector face plate. This proves a significant step forward in understanding high frequency combustion instabilities in rocket engines and their effects on the combustion.

8.3 Conclusion of Methodology

In this section, the methodology applied is summarised, as to provide a clear overview of how the results mentioned in Section 8.2 are obtained. In order to keep a clear overview, this elaboration is also split up according to the three main subquestions in this report.

Determination of changes in integrated heat flux
First, to create a measure for integrated heat flux during stable combustion, a method was constructed that would implement the Bartz equation. Data was available on the propellants as they were injected into the chamber and gas parameters could be calculated as they had achieved completed combustion at the end of the chamber. With this, the convective heat transfer to the wall could be calculated and a measure was known for the local heat flux to the combustor walls at the axial positions of the chamber which had completed combustion. However, no information was available on gas properties as the gases combusted throughout the chamber. In order to reconstruct a heat flux profile, a new method was constructed, based on numerical solutions as completed and presented in previous research. These resulted in a prediction which matched experimental data with varying accuracies as shown in Table 14, but which were not accurate enough for the wanted purpose in this research.

For this reason, a new method was created, which has not been attempted before. This method was based on a purely experimental relation which combines the operating conditions through a power function and is fitted to experimental integrated heat flux values. The data it was compared to was filtered as combustion instabilities were systematically detected and removed before fitting, along with transients in operating conditions, as these are not of interest for this research. With the preprocessed and filtered datasets, the relations are optimised to best match the experimental data and when this process is repeated for each test run, the found relations return good matches with the experimental integrated heat fluxes in both trend and magnitude as shown in Table 15. When extrapolating these relations to time periods with combustion instabilities, it becomes possible to detect magnitudes of changes in integrated heat flux in experimental data with respect to what can be expected during periods of stable combustion.

Explaining changes in integrated heat flux due to combustion instabilities
To explain changes in integrated heat flux it was investigated what effects due to combustion instabilities are known to occur and how to quantify them. It was found that in a research regarding combustion chamber BKH, strong effects regarding changes in injected LOX core length with varying amplitudes of externally excited combustion instabilities exist. These effects were quantified through experimental relations for different operating conditions and presented as results of that research. These relations were taken and implemented into a new model that converts these results to make them compatible

with the combustion chamber BKD around which the present research is centred. To do this, the LOX core relations were scaled with the ratio of transverse velocities over the injectors of BKD and BKH when combustion instabilities of equal magnitude would be applied. Besides, LOX core length during stable combustion are calculated with an experimental relation which uses the momentum flux ratio of the propellants. With both stable and unstable LOX core lengths known, their relative changes are also known. Note that a limitation of this research is that these relations are valid only for chambers with geometry of the injectors similar to those in BKD and BKH.

The LOX core length practically defines the distance from the face plate at which the propellants are mixed with each other in a manner which allows them to combust, thus representing the distance at which mixing has happened. Although there is often a delay between mixing and combustion, this delay is neglected due to lack of accurate representation without making more assumptions and a combustion profile throughout the chamber was established. This combustion profile has been assumed equal to a heat flux profile throughout the chamber, which starts at a low value and rises towards its final value when the gases have been combusted. With the established heat flux profiles, a comparison can be made between those predicted for stable combustion and those for unstable combustion for different magnitudes of combustion instabilities, while their change represents a change in heat flux. As the model only predicts shortened combustion lengths, it will thus also only predict an earlier achieved steady heat flux, returning an increased heat flux. The increases in heat flux with respect to its original distribution over the chamber length will also occur in the region close to the injector face plate, where the gases which combust deeper into the chamber will combust in earlier regions due to combustion zone shortening.

Model validation

In order to validate the model that predicts changes in heat flux experimentally, both constructed models were necessary. The experimentally determined changes in heat flux were compared to the model for changes in integrated heat flux with presence of combustion instabilities of certain magnitudes and plotted over each other while their R^2 and RSE values are calculated.

The first observation was that there seem to be many deviations in heat flux which are observed, but not predicted. However, these were identified to occur mostly during transients in operating conditions and can thus be discarded as these are of no interest for this research. A second observation was that sometimes predicted changes in heat flux are not observed, but also these can be explained. Firstly, when the combustion instabilities are of lower magnitudes (<10bar), it could be that changes in heat flux are not noticed in the noise of the experimental observations. Secondly, it could be that the combination of short duration and low amplitude of these combustion instabilities causes it to be unable to develop the predicted effects.

9 Recommendations for Future Work

The work performed in this report has fulfilled the research goal and the research questions have been answered successfully. However, there are still improvements possible in the work done, some of which could be part of future work while building on this thesis. In order to guide this future work, some recommendations are given, as listed below. These recommendations are grouped based on which segment of the research they apply: the experimental set-up, the theoretical approximations made and the expansion of the current work.

Recommended updates in the experimental set-up

- First of all, the capping off of acoustic pressure measurements at an amplitude of 30bar is a limit to this research which is expected to play a role in the underprediction of changes in integrated heat flux. This has to do with the underestimation of instability magnitudes through its RMS values, which is a valid method for any sinusoidal signal, such as the uncapped acoustic pressure data, but not for a signal for which the peaks are cut-off. In order to deal with this limit, other acoustic pressure sensors should be implemented in the measurements, which are capped at amplitudes larger than the encountered pressure oscillations. Final results however, although more correct, are not expected to change by much, as the increase in heat flux converges around 12bar as can be seen in Figure 48.
- Another recommendation is the implementation of a more complex experimental heat flux measurement set-up such as the segmented calorimetric cylindrical section in the combustion chamber or using the inverted method as explained in Section 2.2.3. This way, no assumptions need to be made about the heat flux profile throughout the chamber, while removing the largest uncertainty in the model as it will become possible to directly observe the changes in heat flux profile that cause local relative increases in heat flux.
- If a measurement for LOX core length during stable combustion was present, the relative increase in heat flux could be predicted with higher certainty. Currently, this measure is being predicted through an experimental relation determined for BKH, while an optical access or other measurement system could allow for direct experimental measurement as explained in Section 4.1.2.
- Lastly, there was a lack of large amplitude combustion instabilities with long durations, mostly due to the hard to predict nature of these self-excited combustion instabilities. For this reason, it would be beneficial to the validation of this model to also externally excite the combustion instabilities, perhaps in a fashion similar to that of BKH, so that a more systematic investigation can be performed of combustion instability in a steady environment. This would allow for a more reliable validation as elaborated on in Sections 7.2 and 7.3.

Recommended improvements in approximations made

- First of all, in this research the LOX core length is equalled to the length of the combustion zone, since no validated measures for other lengths were available as mentioned in Section 4.1.2. If a modification could be implemented to relate these two through a verified model rather than assuming they are the same, it could improve the validity of the constructed model, although it is not expected to change the found results as the model already showed agreement with CFD solutions.
- Secondly, the effects observed in integrated heat flux during transients in operating conditions have been neglected in this research as being irrelevant. However, if these effects could be included into the predictive model for heat flux during stable combustion, the predicted increases in integrated heat flux can be explained with more certainty. It should be stressed that this will not increase the accuracy of the model, but will allow it to be applied in more cases and thus result in larger heat flux data sets available for analysis as elaborated in in Section 4.2.3.
- Lastly, it is recommended that the BKH curves for acoustic pressure oscillation magnitudes and LOX core length could be recreated using BKD data rather than simply adopting the BKH curves for use in this research. If this was possible, there would be no need for the approximations made to make the BKH curves apply to BKD. These new experimental curves would allow for LOX core length determination without making assumptions which could mispredict amplitudes of the modelled effects as mentioned in Section 2.4.2. Although this might help explaining how no effects

are observed from low amplitudes combustion instabilities and it would increase the overall validity of the model, it is not expected to change the results of the model much, especially not in the large amplitude combustion instability time periods. This can be said, as the model already returns results in agreement with experimental data in these regions.

Recommended expansion of the current work

- Research that could contribute or expand the results of this work would be an analysis of the acoustic wave type during the 1T combustion instability mode. In this work, the waves are assumed to be rotating or standing, with a hard threshold being defined as an approximation which comes from limited investigation. Knowing the exact wave type during combustion instabilities would allow for better determination of the pressure field and its corresponding transverse velocity fields and would thus enable better prediction of transverse velocities over the injectors as mentioned in Section 2.3.3. However, the effect of a misprediction has been investigated and showed only minor changes in integrated heat fluxes in a small range of acoustic pressure amplitudes as elaborated on in Section 6.3.
- Research that could contribute to the results of this work, is the expansion of the relation that was constructed to relate operating conditions to measured integrated heat flux. If more parameters, such as viscosity, gas velocity, injection momentum flux ratio of the propellants or others that represent the gas flow and perhaps even the chamber heat retention could be included, more accurate predictions are expected for integrated heat flux predictions for stable combustion during periods of transient operating conditions as mentioned in Section 4.2.3. Although this will not change the conclusions of this research, it would enable better understanding of integrated heat flux trends over time and might enable larger datasets to be analysed for changes in heat flux due to combustion instabilities.
- Research that is focused on numerically solving the combustion process during the operating conditions as applied in the test runs for this research could allow more accurate definition of the stable combustion zone length and perhaps a function such as the one found for BKH could be defined for BKD to relate its length with acoustic pressure magnitudes. This could increase the validity of the models to predict relative changes in local heat fluxes, although the correctness of numerical solutions without experimental data is still debatable.

Training Required to Perform the Recommended Work

- If a researcher was to pick up this work and perform some or all of the recommendations made, some background knowledge or training can also be recommended. First of all, general knowledge on rocket engines and the combustion processes that take place in rocket engines are considered crucial. This, as to allow simple verifications of any calculation by checking its answers with known solutions such as those for combustion temperatures, chamber pressures and injection velocities, but also to allow the researcher to get a general grip on the involved matter more quickly.
- Secondly, it is recommended that the researcher has available test data regarding BKH, BKD or another experimental combustion chamber with either of the recommended upgrades to the available experimental set-up of this research. The same test data as used for this research could also be used, but it is expected to produce only limited new results.
- Other, more specific knowledge could be of an advantage, although not considered necessary from the point of view of the author.

References

[1] G. Sutton and O. Biblarz. *Rocket propulsion elements*. John Wiley & Sons, 2016.

[2] D.K. Huzel. *Modern engineering for design of liquid-propellant rocket engines*, volume 147. AIAA, 1992.

[3] B. Zandbergen. AE4-S01 - Thermal Rocket Propulsion (version 2.06). 2017, Course Reader.

[4] D. Harrje. NASA SP-194 Liquid propellant rocket combustion instability. 1972.

[5] E.M. Contright. *Apollo Expeditions to the Moon*. Number SP-350. National Aeronautics and Space Administration, Washington DC, online edition edition, 1975. Online electronic formatting by Engel, H., url: `https://history.nasa.gov/SP-350/cover.html`.

[6] G. Schmidt. *Technik der Flüssigkeits-Raketentriebwerke*. DaimlerChrysler Aerospace, 1999.

[7] E. Bergaust. *Wernher von Braun*. Stackpole Books, 2017.

[8] D. Warren and C. Langer. History in the making-the mighty f-1 rocket engine. In *25th Joint Propulsion Conference*, page 2387, 1989.

[9] DLR - Geschichte des Standorts. `https://www.dlr.de/desktopdefault.aspx/tabid-2039/2510_read-3894/`. Accessed: 2018-10-15.

[10] J. Melcher and R. Morehead. Combustion stability characteristics of the project Morpheus liquid oxygen/liquid methane main engine. In *50th AIAA/ASME/SAE/ASEE Joint Propulsion Conference*, 2014.

[11] G. Jones, C. Protz, and J. Bullard, B.and Hulka. Local Heat Flux Measurements with Single and Small Multi-element Coaxial Element-Injectors. 2006.

[12] J.R. Hulka and G.W. Jones. Performance and stability analyses of rocket thrust chambers with oxygen/methane propellants. *46th AIAA/ASME/SAE/ASEE Joint Propulsion Conference and Exhibit*, (AIAA 2010-6799), 01 2010.

[13] W. Anderson and V. Yang. *Liquid rocket engine combustion instability*. American Institute of aeronautics and astronautics, 1995.

[14] A. Urbano, Q. Douasbin, L. Selle, G. Staffelbach, B. Cuenot, T. Schmitt, S. Ducruix, and S. Candel. Study of flame response to transverse acoustic modes from the LES of a 42-injector rocket engine. *Proceedings of the Combustion Institute*, 36(2):2633–2639, 2017.

[15] M. Schulze and T. Sattelmayer. Flamedynamics in Supercritical H2/O2 Rocket Combustion Systems. *SFB TRR40 Annual Report 2015*, 2015.

[16] J. Hardi. *Experimental investigation of high frequency combustion instability in cryogenic oxygen-hydrogen rocket engines.* PhD thesis, 2012.

[17] J. Hardi, H. Martinez, M. Oschwald, and B. Dally. LOx jet atomization under transverse acoustic oscillations. *Journal of propulsion and power*, 30(2):337–349, 2014.

[18] J. Hardi and M. Oschwald. Cryogenic oxygen jet response to transverse acoustic excitation with the first transverse and the first combined longitudinal-transverse modes. *Progress in Propulsion Physics*, 8:75–94, 2016.

[19] S. Gröning. *Untersuchung selbsterregter Verbrennungsinstabilitäten in einer Raketenbrennkammer*. PhD. Dissertation, Fakultät für Maschinenwesen der Rheinisch-Westfälischen Technischen Hochschule Aachen, 2017.

[20] W. Armbruster, S. Gröning, J. Hardi, M. Oschwald, and D. Suslov. High-Frequency combustion instability with H2 injection coupling in a LOX/H2 rocket combustor. *Thermoacoustic Instabilities in Gas turbines and Rocket Engines: Industry meets Academia*, 2016.

[21] G. Schmidt, G. Langel, and H. Zewen. Development status of the Ariane 5 upper-stage AESTUS engine. In *29th Joint Propulsion Conference and Exhibit*, page 2131, 1993.

[22] Matthieu M Masquelet. *Simulations of a sub-scale liquid rocket engine: Transient heat transfer in a real gas environment*. PhD thesis, Georgia Institute of Technology, 2006.

[23] M. L. Dranovsky. *Combustion instabilities in liquid rocket engines: testing and development practices in Russia*. American Institute of Aeronautics and Astronautics, 2007.

[24] T.B. Govaert. Analysis of the influence of high frequency combustion instabilities on heat transfer in a sub-scale LOX/H2 rocket thrust chamber. Internship report DLR-LA-RAK-HF-RP-096, German Aerospace Centre (DLR), Lampoldshausen, Germany, December 2018.

[25] F-1 Engine (Davidson Center). online: `http://heroicrelics.org/ussrc/engines-f-1-dcse/index.html`.

[26] W. Armbruster, J. Hardi, and M. Oschwald. Experimentelle untersuchung selbsterregter verbrennungsinstabilitäten in einer LOX/H2 raketenbrennkammer. 2017.

[27] W. Armbruster, J. Hardi, D. Suslov, and M. Oschwald. Experimental investigation of self-excited combustion instabilities with injection coupling in a cryogenic rocket combustor. *Acta Astronautica*, 151:655–667, 2018.

[28] National Aeronautics and Space Administration. Chemical equilibrium with applications program. software, Version relase: May 21, 2004.

[29] E.W. Weisstein. Bessel Function of the First Kind. MathWorld–A Wolfram Web Resource. Accessed online (18 Feb 2019): `http://mathworld.wolfram.com/BesselFunctionoftheFirstKind.htm`.

[30] J. S. Hardi, R. Kaess, F. Tonti, P. N. Blanco, S. Soller, M. Oschwald, A. Gernoth, and M. De Rosa. Study of the Influence of Operating Conditions on LOX/H2 Thrust Chamber Acoustic Eigenmodes. ESA TRP Report SP2018˙00093, ESTEC European Space Agency, 2018.

[31] M. Schulze, M. Schmid, D. Morgenweck, S. Köglmeier, and T. Sattelmayer. A conceptional approach for the prediction of thermoacoustic stability in rocket engines. In *49th AIAA/ASME/SAE/ASEE Joint PropulsionConference*, page 3779. 2013.

[32] J. Cornelisse, H. Schoyer, and K. Wakker. Rocket propulsion and spaceflight dynamics. *London: Pitman, 1979*, 1979.

[33] D.R. Bartz. A simple equation for rapid estimation of rocket nozzle convective heat transfer coefficients. *Journal of Jet Propulsion*, 27:49–51, 1957.

[34] National Insitute of Standards and Technology. `https://www.nist.gov/`. Accessed: 2018-10-18.

[35] M. Oschwald. Raumfahrtantriebie II - Verbrennungsinstabilitäten. 03-06 November 2015, Lecture Presentation.

[36] S. Babu. Dependence of liquid oxygen core length on transverse acoustic amplitude for shear coaxial injection in a rocket combustion chamber. Master thesis, IIT Kharagpur, Department of Aerospace Engineering, May 2019.

[37] A.M. Cardenas. *Influence of Enhanced Heat Transfer driven by Pulsating Flow on the Damping Characteristics of Resonator-Rings*. PhD thesis, Technische Universität München, 2014.

[38] J. Dec, J. Keller, and V. Arpaci. Heat transfer enhancement in the oscillating turbulent flow of a pulse combustor tail pipe. *International journal of heat and mass transfer*, 35(9):2311–2325, 1992.

[39] J. Dec and J. Keller. Pulse combustor tail-pipe heat-transfer dependence on frequency, amplitude, and mean flow rate. *Combustion and flame*, 77(3-4):359–374, 1989.

[40] U.H. Kurzweg. Enhanced heat conduction in fluids subjected to sinusoidal oscillations. *Journal of Heat Transfer*, 107(2):459–462, 1985.

[41] L.D. Landau and E.M. Lifshitz. *Fluid Mechanics*, volume 6 of *Course of Theoretical Physics*. Pergamon Press, 2 edition, 1959. Translated from Russian by J.B. Sykes and W.H. Reid.

[42] S. Beinke, D. Banuti, J. Hardi, M. Oschwald, and B. Dally. Modelling Flame Response of a Co-axial LOx/GH2 Injection Element to High Frequency Acoustic Disturbances. In *6th European Conference for Aeronautical and Space Sciences (EUCASS), Krakow, Poland, 3AF, Krakow, Poland*, 2015.

[43] S. Beinke, F. Tonti, S. Karl, J. Hardi, M. Oschwald, and B. Dally. Modelling Flame Response of a Co-axial LOx/GH2 Injection Element to High Frequency Acoustic Forcing. In *7th European Conference for Aeronautics and Aerospace Sciences (EUCASS) 2017*, 2017.

[44] J.S. Hardi, S.C.L. Webster, and M. Oschwald. Response of a reacting cryogenic oxygen jet to transverse acoustic forcing. In *Conference: Space Propulsion 2016*, number SP2016˙3124712. Institute of Space Propulsion, German Aerospace Center (DLR), May 2016.

[45] M. Sliphorst. Simple Models for Heat Transfer Estimation in Rocket Engine Combustion Chambers. Master's thesis, Delft University of Technology, 2004. Thesis completed in collaboration with EADS.

[46] R.D. Woodward, S. Pal, R.J. Santoro, and K.K. Kuo. Measurement of core structure of coaxial jets under cold-flow and hot-fire conditions. *Recent advances in spray combustion: Spray atomization and drop burning phenomena.*, 1:185–209, 1996.

[47] B.A. Younglove. Thermophysical properties of fluids. I. Argon, ethylene, parahydrogen, nitrogen, nitrogen trifluoride, and oxygen. Technical report, National Standard Reference Data System, 1982.

[48] S. Gröning, J. Hardi, D. Suslov, and M. Oschwald. Injector-driven combustion instabilities in a hydrogen/oxygen rocket combustor. *Journal of Propulsion and Power*, (0):560–573, 2016.

[49] M. Oschwald. Manuskript zur Vorlesung - Raumfahrtantriebe I. 2018, Course Reader.

[50] T.A. Davidson. A Simple and Accurate Method for Calculating Viscosity of Gaseous Mixtures. Report of Investigations 9456, United States Department of the Interior - Bureau of Mines, Montgomery, April 1993.

[51] F.J. Krieger. Calculation of the Viscosity of Gas Mixtures. Research Memorandum RM-649, U.S. Air Force, The RAND Corporation, California, July 1951. working paper.

[52] V. Zhukov and D. Suslov. Measurements and modelling of wall heat fluxes in rocket combustion chamber with porous injector head. *Aerospace Science and Technology*, 48:67–74, 2016.

[53] A. Woschnak. *Untersuchung des Wärmeübergangs in regenerativ gekühlten Schubkammern kryogener Raketentriebwerke*. Shaker, 2009.

[54] H. Ivancic, B. abd Riedmann and M. Frey. Validation of turbulent combustion models for 3D-simulations of liquid H2/O2 rocket combustors. In *Space Propulsion Conference. Bordeaux, France*, 2012.

[55] D.W. Davis. On the behavior of a shear-coaxial jet, spanning sub-to supercritical pressures, with and without an externally imposed transverse acoustic field. Technical report, Pennsylvania State University, 2006.

Appendix A: Derivation of Hydrolox Propellant Mass Fraction Approximation

In order to calculate the mole fractions of gas components in the combusted hydrolox gas mixture, a simple approximation can be used. To do this, first it is assumed that gases are combusted in an ideal way with no resulting side-products. In the case of BKD, the fuel is hydrogen (H_2) and the oxidiser is oxygen (O_2), while their combustion product is water (H_2O). It also assumes that the unreacted molecules remain in their original form. First of all, the chemical reaction of the combustion of oxygen and hydrogen is looked at, as shown in Equation A.1. Note that it is assumed that there are more hydrogen than oxygen molecules, as is always the case for test runs in BKD.

$$n_{h2} \cdot H_2 + O_2 \rightarrow 2 \cdot H_2O + (n_{h2} - 2) \cdot H_2 \tag{A.1}$$

The molecular weights of the injected hydrogen and oxygen are known, respectively given as 2g/mol, 32g/mol [34]. With these and Equation A.1, the oxidiser to fuel ratio (ROF) can be expressed as a function of the mole ratios, as shown in Equation A.2 and Equation A.3. In order to achieve a combustion with no remaining hydrogen, or the stoichiometric combustion, the total number of remaining hydrogen moles must equal zero, meaning that n_{h2} is defined. With this criterion, the stoichiometric ROF can be defined as shown in Equation A.3

$$ROF = \frac{32}{2n_{h2}} \tag{A.2}$$

$$ROF_{stoichiometric} = \frac{32}{2 \cdot 2} = 8 \tag{A.3}$$

Now, it can be stated that the total number of moles on the right hand side is the sum of the number of moles per component. This is given in Equation A.4.

$$n_{tot} = 2n_{o2} + (n_{h2} - 2n_{o2}) = n_{h2} \tag{A.4}$$

Finally, the mole fraction of water and hydrogen can be given as a ratio of their respective number of moles to the total number of moles as shown in Equation A.5 and Equation A.6.

$$x_{H_2O} = \frac{2}{n_{h2}} = \frac{\frac{32}{2n_{h2}}}{\frac{32}{2 \cdot 2}} = \frac{ROF}{ROF_{stoichiometric}} \tag{A.5}$$

$$x_{H_2} = 1 - x_{H_2O} \tag{A.6}$$

This approximation has been tested and compared to values calculated with CEA for a range of ROF between 3 and 6 as these are relevant for this thesis work. For ROF of 3, the error in calculated mole fractions is very small, being 0.281% for hydrogen and 0.089% for water. For a ROF value of 6 the prediction in hydrogen mole fraction also has small errors of only 0.17%, while the water mole fraction has larger deviations of 11.145%. It can be concluded that the method is especially applicable for lower ROF values, while for higher ROF values there is a larger deviation in calculated water mole fraction with respect to the real situation. This is mostly due to the presence of other combustion products at higher ROF values.

Appendix B: Derivation of Transverse Velocity Fields

In literature, the transverse velocity fields have been described, although no full derivations and full solutions were readily available [B.1]. For this reason it was decided to re-derive the analytical solution for the transverse velocity field over a cross section of the combustion chamber for the 1T mode. For this purpose, a split has been made between standing and rotating waves. This is necessary, because the time dependent shape of their pressure fields and thus also of the velocity fields differs, as explained in Section 2.3. The derivation for these two velocity fields is given below, starting with standing waves and then for rotating waves. Resulting pressure and velocity fields match results described in literature [B.1] and are thus considered valid for application in this research work.

Standing Waves

The total force F acting on a volume in a fluid can be given as the surface integral of the pressure, p, over the entire surface bounding the volume as shown in Equation B.1.

$$F = \oint p df \tag{B.1}$$

This surface integral can also be written as a volume integral, as defined in Equation B.2 where ∇p represents the pressure gradient. Now, when considering only a unit volume, the integral can be dropped and it can be seen that the total external force acting on any unit volume of the fluid is equal to $-\nabla p$.

$$\oint p df = -\int \nabla p dV \tag{B.2}$$

Next, the equation of motion of this unit volume can be written down, where ρ is the mass per unit volume and the acceleration is given as dV/dt

$$-\nabla p = \rho \frac{dV}{dt} \tag{B.3}$$

This equation can be rewritten in function of the velocity of that volume element as shown in Equation B.4. Finally the velocity of that unit volume can be written as Equation B.5 by integrating both sides over time. Note that a constant resulting from the integration on the velocity side of the equation is not included, due to the periodic nature of the transverse gas movements during the investigated wave.

$$\frac{dV}{dt} = -\frac{1}{\rho}\nabla p \tag{B.4}$$

$$V = \int -\frac{1}{\rho}\nabla p dt \tag{B.5}$$

Lastly, when further considering the 1T acoustic wave, the pressure distribution over the length of the combustion chamber is known to be uniform, meaning there is only a cross sectional variation in pressure and thus of velocity. Since the pressure distribution over the chamber cross section is easiest written in polar coordinates as explained in Section 9, the velocity integral is also written in polar coordinates to facilitate further derivations.

$$V(\theta, r_\theta, t) = \int -\frac{1}{\rho}\nabla p(\theta, r_\theta, t) dt \tag{B.6}$$

Now that the velocity field is described in function of the pressure distribution over a chamber cross section, a focus can be put on the standing wave and its velocity field. As explained in Section 9, the pressure field of this wave can be given as Equation B.7.

$$p'(\theta, r_\theta, t) = \frac{A(t)}{J_1(\pi\alpha_{01})} J_1\left(\frac{2\pi\alpha_{01} r_\theta}{D_c}\right) \cdot cos(\theta) cos(\omega t) \tag{B.7}$$

The gradient of this pressure field has to be taken in both radial and angular spatial directions, requiring a split up in radial and angular velocity components. For this reason, the velocity components are derived separately, starting with the angular component. It should be noted that the density term is simplified to be the bulk density in the flow and is assumed constant throughout the considered cross section [19].

$$V_\theta(\theta, r_\theta, t) = \int -\frac{1}{\rho} \cdot \nabla_\theta \left(\frac{A(t)}{J_1(\pi\alpha_{01})} \cdot J_1\left(\frac{2\pi\alpha_{01} r_\theta}{D_c}\right) \cdot cos(\theta) cos(\omega t)\right) dt \tag{B.8}$$

$$V_\theta(\theta, r_\theta, t) = \frac{A(t)}{\rho J_1(\pi\alpha_{01})} \cdot J_1\left(\frac{2\pi\alpha_{01} r_\theta}{D_c}\right) \cdot \int \frac{1}{r} sin(\theta) cos(\omega t) dt \tag{B.9}$$

$$V_\theta(\theta, r_\theta, t) = \frac{A(t)}{r\omega\rho} \cdot \frac{1}{J_1(\pi\alpha_{01})} \cdot J_1\left(\frac{2\pi\alpha_{01} r_\theta}{D_c}\right) \cdot sin(\theta) sin(\omega t) \tag{B.10}$$

$$V_\theta(\theta, r_\theta, t) = \frac{A(t)}{r2\pi f\rho} \cdot \frac{1}{J_1(\pi\alpha_{01})} \cdot J_1\left(\frac{2\pi\alpha_{01} r_\theta}{D_c}\right) \cdot sin(\theta) sin(\omega t) \tag{B.11}$$

The radial component is derived similarly as demonstrated below.

$$V_r(\theta, r_\theta, t) = \int -\frac{1}{\rho} \cdot \nabla_r \left(\frac{A(t)}{J_1(\pi\alpha_{01})} \cdot J_1\left(\frac{2\pi\alpha_{01} r_\theta}{D_c}\right) \cdot cos(\theta) cos(\omega t)\right) dt \tag{B.12}$$

$$V_r(\theta, r_\theta, t) = -\frac{A(t)}{\rho J_1(\pi\alpha_{01})} \cdot \frac{dJ_1\left(\frac{2\pi\alpha_{01} r_\theta}{D_c}\right)}{dr_\theta} \cdot cos(\theta) \int cos(\omega t) dt \tag{B.13}$$

$$V_r(\theta, r_\theta, t) = -\frac{A(t)}{\omega\rho} \cdot \frac{1}{J_1(\pi\alpha_{01})} \cdot \frac{dJ_1\left(\frac{2\pi\alpha_{01} r_\theta}{D_c}\right)}{dr_\theta} \cdot cos(\theta) sin(\omega t) \tag{B.14}$$

$$V_r(\theta, r_\theta, t) = -\frac{A(t)}{2\pi f\rho} \cdot \frac{1}{J_1(\pi\alpha_{01})} \cdot \frac{dJ_1\left(\frac{2\pi\alpha_{01} r_\theta}{D_c}\right)}{dr_\theta} \cdot cos(\theta) sin(\omega t) \tag{B.15}$$

In order to obtain the total magnitude of the transverse velocity of the fluid at any point in the evaluated cross section, both components can be added together as Equation B.16.

$$V(\theta, r_\theta, t) = \sqrt{V_r(\theta, r_\theta, t)^2 + V_\theta(\theta, r_\theta, t)^2} \tag{B.16}$$

Rotating Waves

In order to derive the transverse velocity field for a rotating wave, the derivation presented for standing waves to relate velocity fields to pressure distribution still applies. For this reason, the derivation presented below will start from Equation B.6, although this time the pressure distribution is given by Equation B.17.

$$p'(\theta, r_\theta, t) = \frac{A(t)}{J_1(\pi\alpha_{01})} J_1\left(\frac{2\pi\alpha_{01} r_\theta}{D_c}\right) \cdot cos(\theta + \omega t) \tag{B.17}$$

Again, the velocity field is split into an angular and radial component. Derivation for the angular component is shown first.

$$V_\theta(\theta, r_\theta, t) = \int -\frac{1}{\rho} \cdot \nabla_\theta \left(\frac{A(t)}{J_1(\pi\alpha_{01})} \cdot J_1\left(\frac{2\pi\alpha_{01} r_\theta}{D_c}\right) \cdot cos(\theta + \omega t) \right) dt \tag{B.18}$$

$$V_\theta(\theta, r_\theta, t) = \frac{A(t)}{\rho J_1(\pi\alpha_{01})} \cdot J_1\left(\frac{2\pi\alpha_{01} r_\theta}{D_c}\right) \cdot \int \frac{1}{r} sin(\theta + \omega t) dt \tag{B.19}$$

$$V_\theta(\theta, r_\theta, t) = -\frac{A(t)}{r\omega\rho} \cdot \frac{1}{J_1(\pi\alpha_{01})} \cdot J_1\left(\frac{2\pi\alpha_{01} r_\theta}{D_c}\right) \cdot cos(\theta + \omega t) \tag{B.20}$$

$$V_\theta(\theta, r_\theta, t) = \frac{A(t)}{r2\pi f\rho} \cdot \frac{1}{J_1(\pi\alpha_{01})} \cdot J_1\left(\frac{2\pi\alpha_{01} r_\theta}{D_c}\right) \cdot cos(\theta + \omega t) \tag{B.21}$$

The radial component is then derived as shown below.

$$V_r(\theta, r_\theta, t) = \int -\frac{1}{\rho} \cdot \nabla_r \left(\frac{A(t)}{J_1(\pi\alpha_{01})} \cdot J_1\left(\frac{2\pi\alpha_{01} r_\theta}{D_c}\right) \cdot cos(\theta + \omega t) \right) dt \tag{B.22}$$

$$V_r(\theta, r_\theta, t) = -\frac{A(t)}{\rho J_1(\pi\alpha_{01})} \cdot \frac{dJ_1\left(\frac{2\pi\alpha_{01} r_\theta}{D_c}\right)}{dr_\theta} \cdot \int cos(\theta + \omega t) dt \tag{B.23}$$

$$V_r(\theta, r_\theta, t) = -\frac{A(t)}{\omega\rho} \cdot \frac{1}{J_1(\pi\alpha_{01})} \cdot \frac{dJ_1\left(\frac{2\pi\alpha_{01} r_\theta}{D_c}\right)}{dr_\theta} \cdot sin(\theta + \omega t) \tag{B.24}$$

$$V_r(\theta, r_\theta, t) = -\frac{A(t)}{2\pi f\rho} \cdot \frac{1}{J_1(\pi\alpha_{01})} \cdot \frac{dJ_1\left(\frac{2\pi\alpha_{01} r_\theta}{D_c}\right)}{dr_\theta} \cdot sin(\theta + \omega t) \tag{B.25}$$

In order to combine the velocity vectors to obtain the velocity magnitude at each point in the cross section, the same method applies as for the standing wave, given again as Equation B.26.

$$V(\theta, r_\theta, t) = \sqrt{V_r(\theta, r_\theta, t)^2 + V_\theta(\theta, r_\theta, t)^2} \tag{B.26}$$

References

[B.1] S. Gröning. *Untersuching selbsterregter Verbrennungsinstabilitäten in einer Raketenbrennkammer.* PhD. Dissertation, Fakultä für Maschinenwesen der Rheinisch-Westfälischen Technischen Hochschule Aachen, 2017.

Appendix C: Overview of Available Testrun Data.

In this appendix, an overview is given of all experimental test runs performed with combustion chamber BKD of which data has been made available for this research. These test runs are summarised in Table C.1, while an overview of the operating conditions and relevant data is given per test. This consists of the calculated experimental integrated heat flux, the prediction of the integrated heat flux for the given combination of operating conditions as optimised based on available test data, the acoustic pressure amplitudes as bandpass filtered for chamber acoustics (from 2500 Hz as it was noticed that lower frequencies are not representative of chamber acoustics, to 50000 Hz as limited by the sampling rate of the measurement sensors), the acoustic pressure amplitudes but bandpass filtered for the frequency range known to contain the 1T chamber mode for reference, the ROF, chamber pressure and hydrogen inlet temperature. Besides, coolant water data is given in the form of pressure, temperature and mass flow trends over time. Although no quantitative data is given, these trends allow insight into how significant and how quickly they change over the test runs. This test data is property of the German Aerospace Center is is not publicly available for other research.

Test runs are grouped according to similarities in their test sequence and are presented in the following sections.

Table C.1: Summary of available experimental test runs.

Test runs with liquidlike H_2	Test runs with gaslike H_2
L1	G1
L2	G2
L3	G3
L4	G4

L1 and L2

This test sequence contains two test runs wherein the hydrogen temperature is kept relatively low as to achieve liquidlike properties for the injected fuel. Both runs show large amplitude (25+ bar) acoustic pressure peaks, of which for both test runs the frequency is mostly corresponding to the 1T frequency range for given operating conditions. Especially interesting is test run L1, where the combustion instability persists throughout different operating conditions and for longer durations of time, being the only available test run where this is the case. It can also be seen how the hydrogen inlet temperature shows an increase towards the end of the test run. This is not due to heating of the injector plate, rather due to the pressure decrease in the hydrogen storage tanks towards the end of the test runs after outflow of most of its contents. This hydrogen temperature phenomenon is also visible in all other test runs but will not be further elaborated.

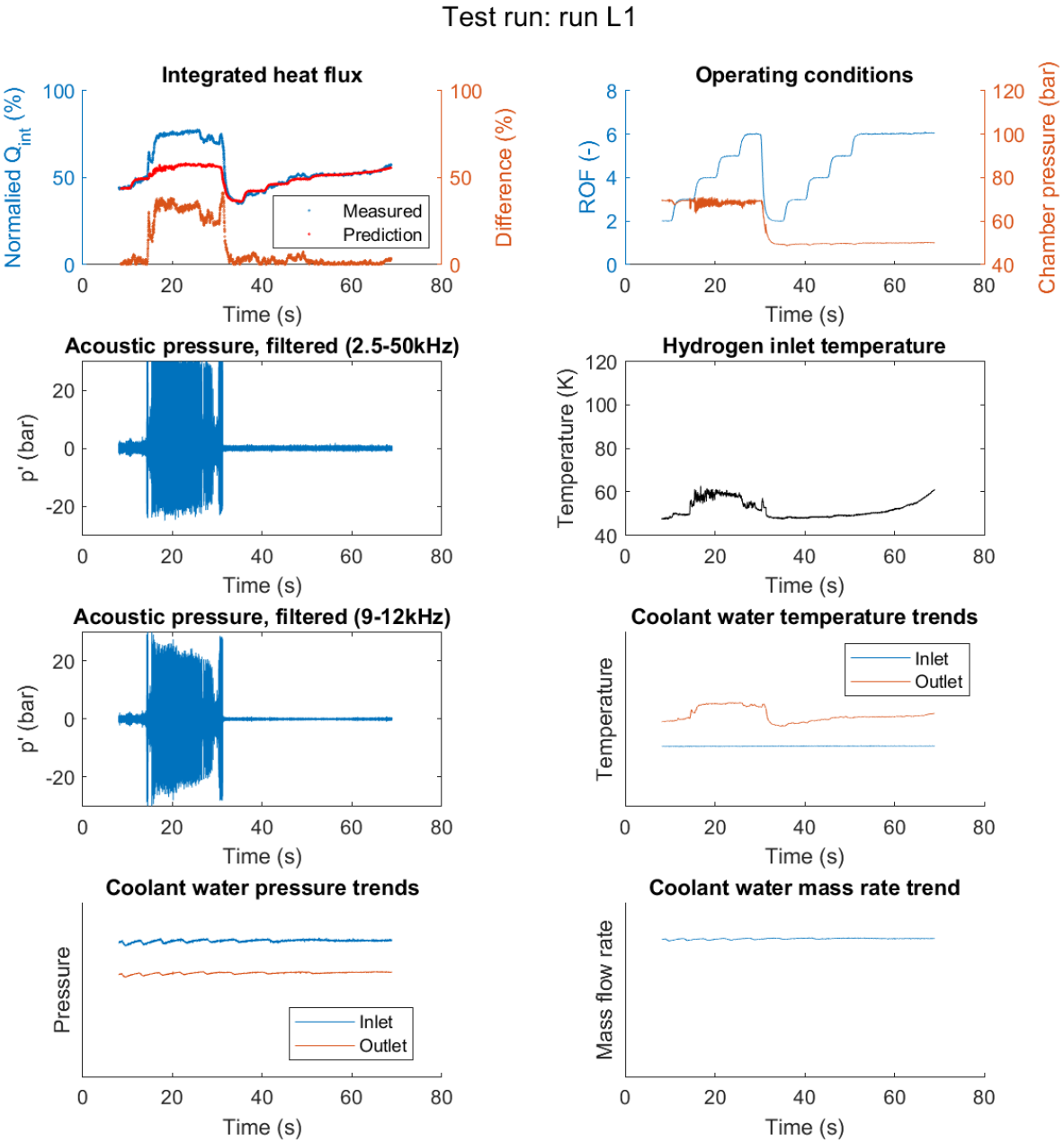

Figure C.1: Test run L1.

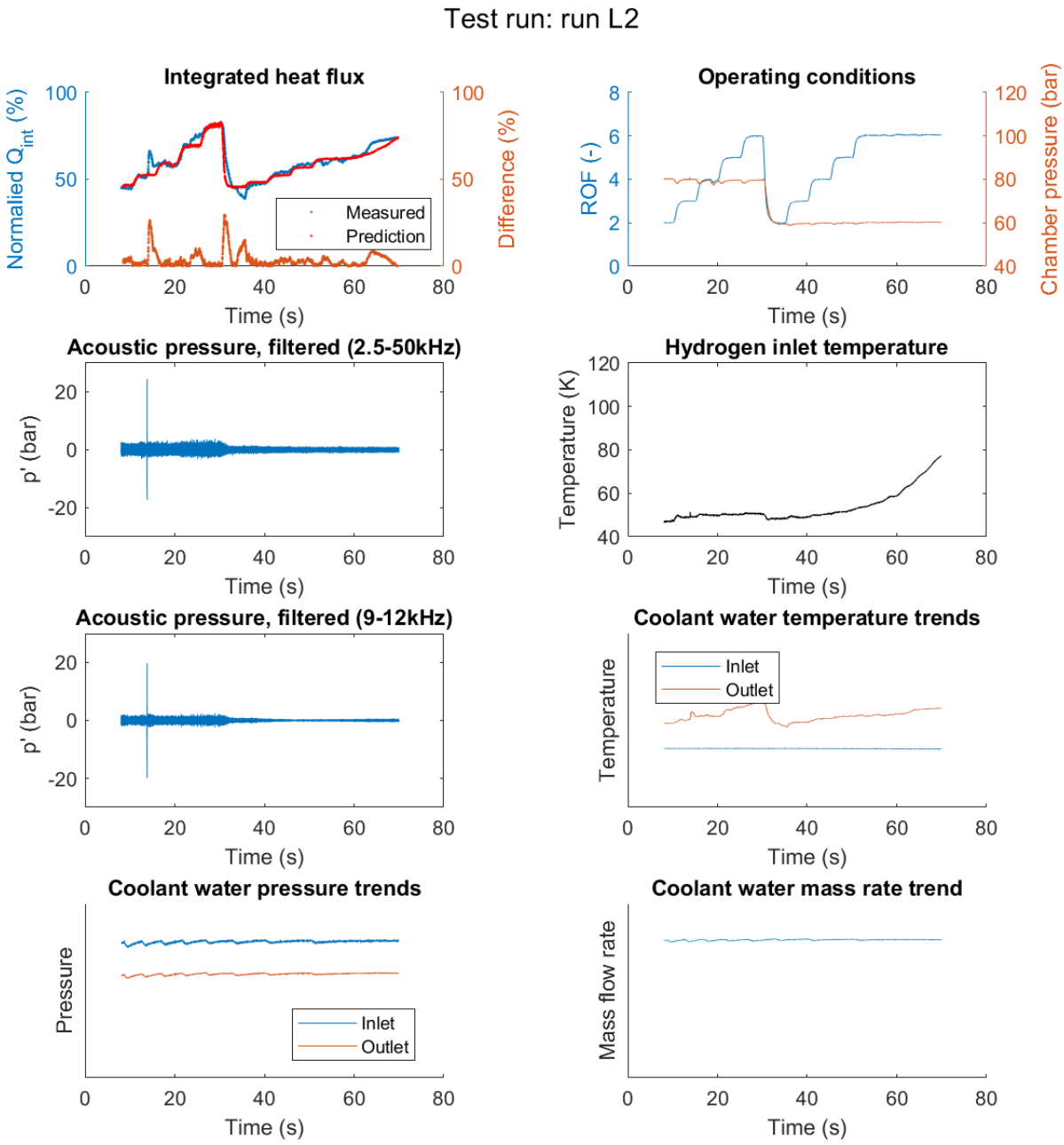

Figure C.2: Test run L2.

L3 and L4

Also in this test sequence the hydrogen temperature is kept relatively low as to achieve liquidlike properties for the injected fuel. Testrun L3 shows no high frequency combustion instabilities as acoustic pressures never reach amplitudes above 1.5bar, while test run L4 shows instabilities with varying amplitudes. It should be noted that the heat flux prediction, especially in the first ROF ramping time period for run L4 shows a bad match with the experimental data. This mismatch of prediction and experimental data does not coincide with a combustion instability, although it occurs immediately after a large amplitude (25+ bar) combustion instability, suggesting some kind of disturbed flow. However, as this mismatch occurs with an offset in time and because the heat flux does not seem to have any consistent offset, these effects are difficult to explain and predict in a reliable way. For these reasons, the correlation cannot be used with confidence and this test run is discarded from further analyses.

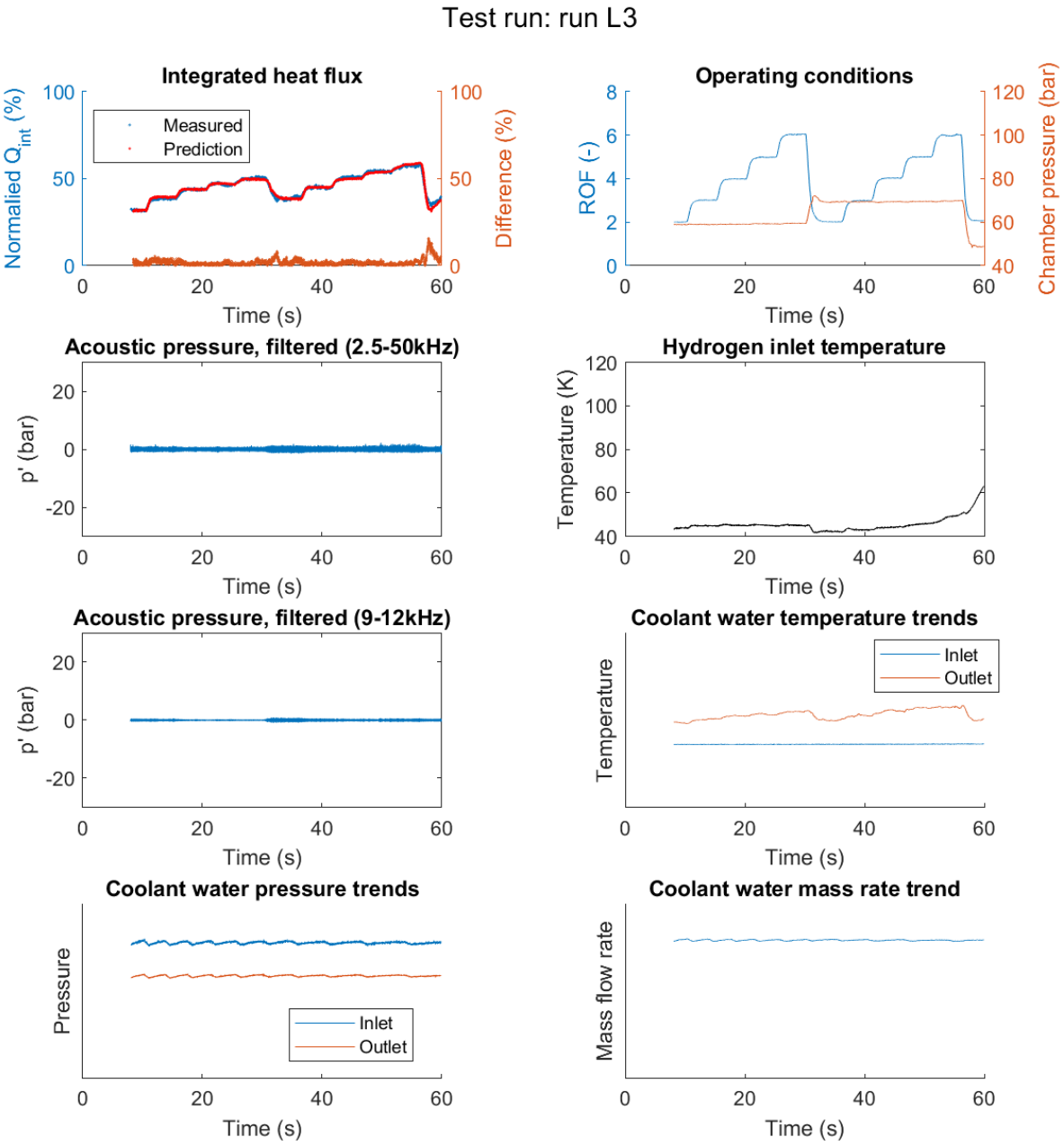

Figure C.3: Test run L3.

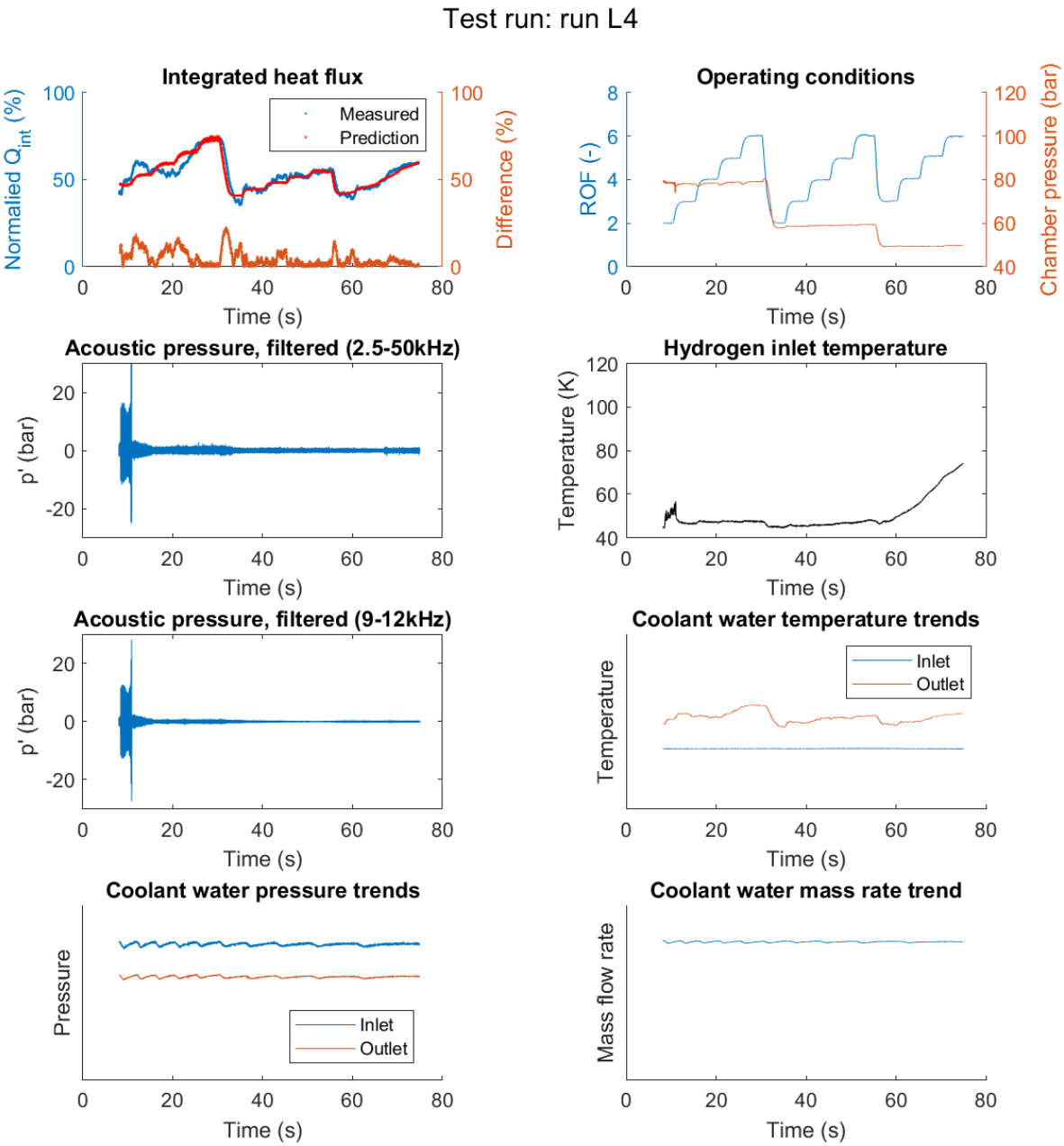

Figure C.4: Test run L4.

G1 and G2

In these test runs the hydrogen temperature is kept relatively high as to achieve gaslike properties for the injected fuel. Both test runs show combustion instabilities with relatively limited amplitude ($\tilde{1}0$ bar). It should be noted that the heat flux prediction, especially in the first ROF ramping time period for run G1 shows a bad match with the experimental data. In the time period of this mismatch, the experimentally determined heat flux seems to show a downwards slope during intervals of constant operating conditions and no combustion instabilities. This unexplained downwards slope is also present at periods in time that do not coincide with a combustion instability, suggesting another unknown effect is taking place. For this reason the correlated prediction is deemed unreliable for test run G1, although the one for test run G2 is kept. For both runs there is a period with a 10+ bar combustion instability, which seems to correspond to a decrease in heat flux of about 6%.

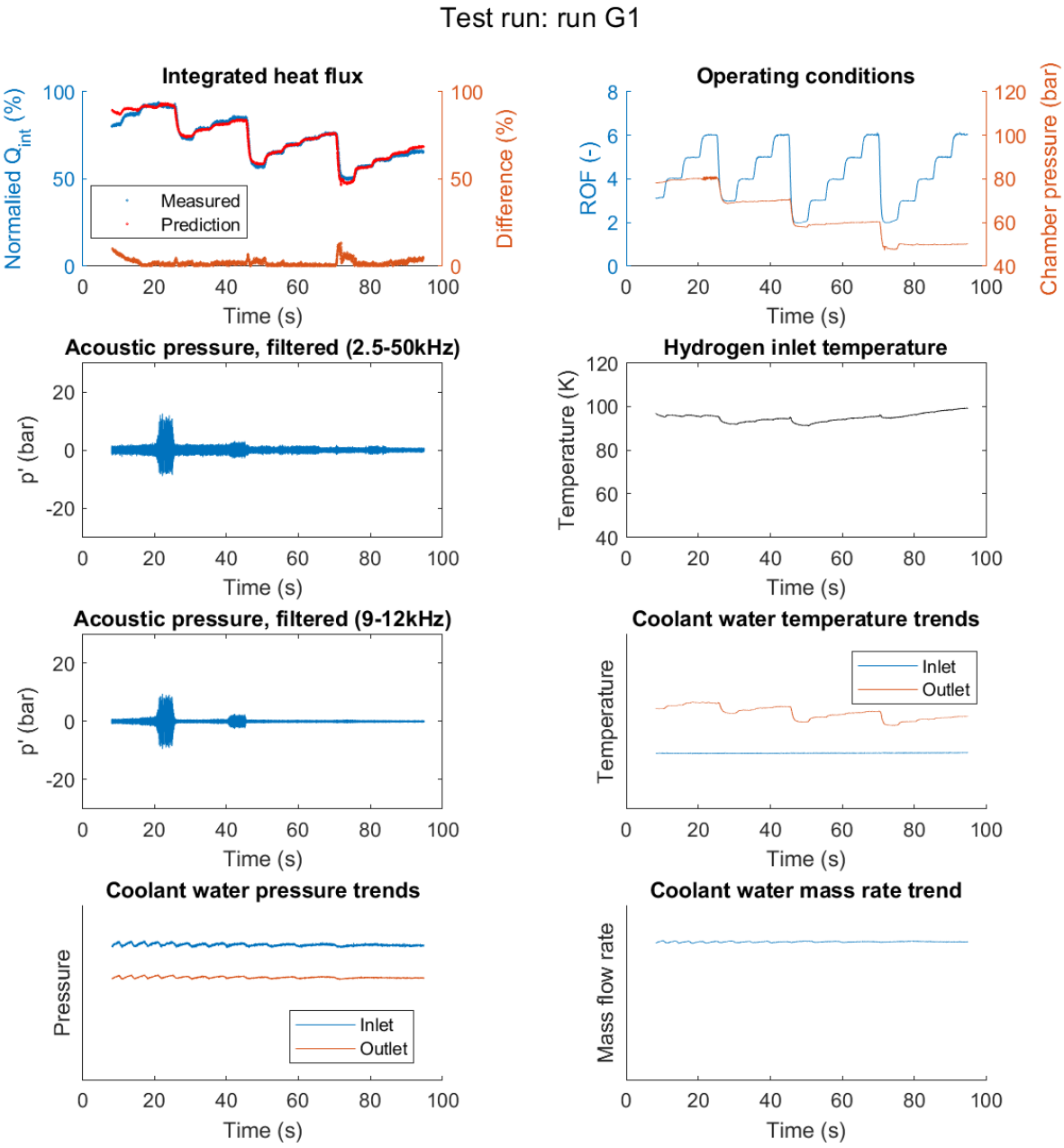

Figure C.5: Test run G1.

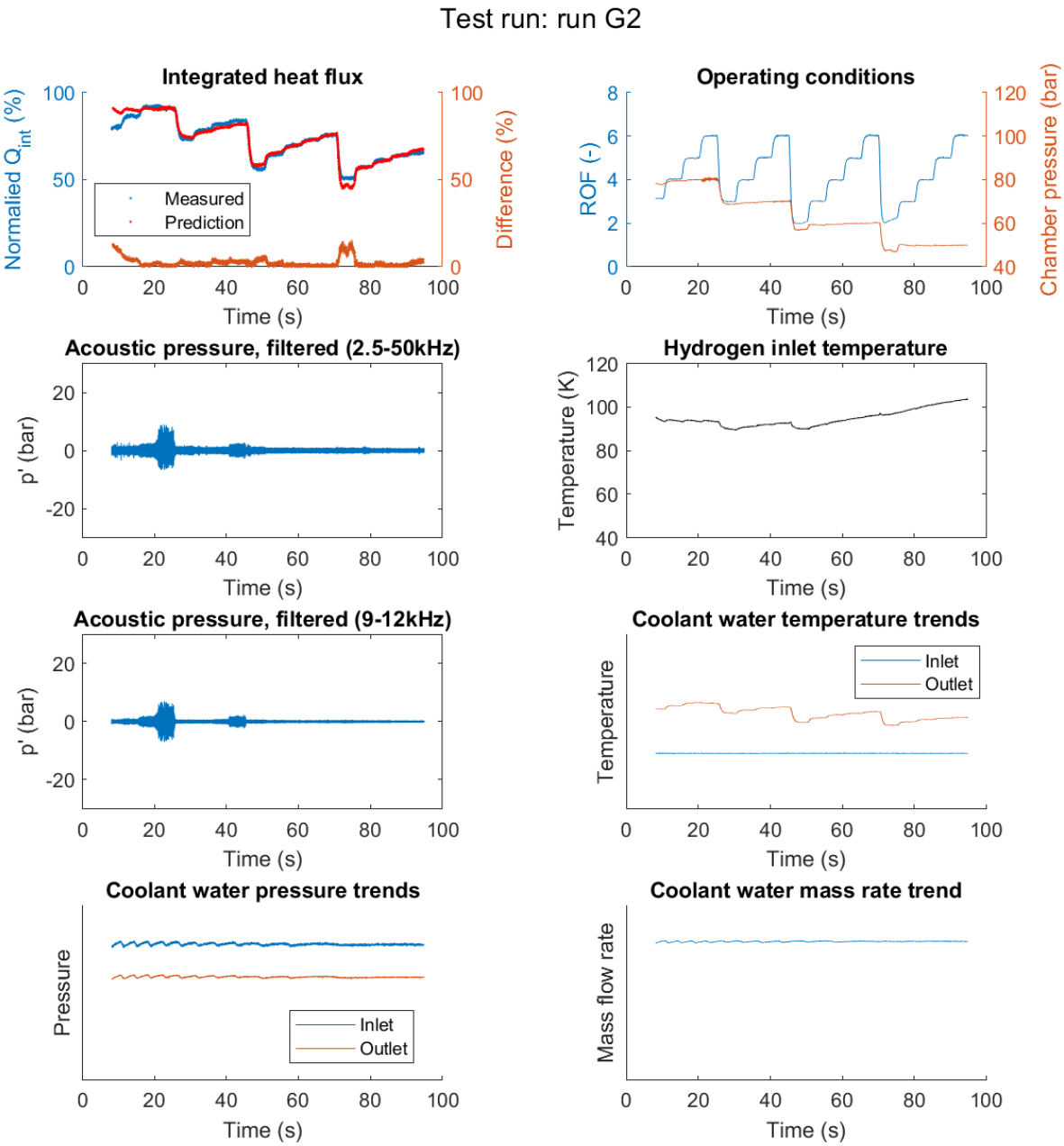

Figure C.6: Test run G2.

G3 and G4

This test sequence also contains two test runs wherein the hydrogen temperature is kept relatively high as to achieve gaslike properties for the injected fuel. Both runs show large amplitude (25+ bar) acoustic pressure peaks, of which for both test runs the frequency is mostly corresponding to the 1T frequency range for given operating conditions. Notable is that no significant (+5%) changes in heat flux seem to be present, even during large acoustic pressure amplitudes.

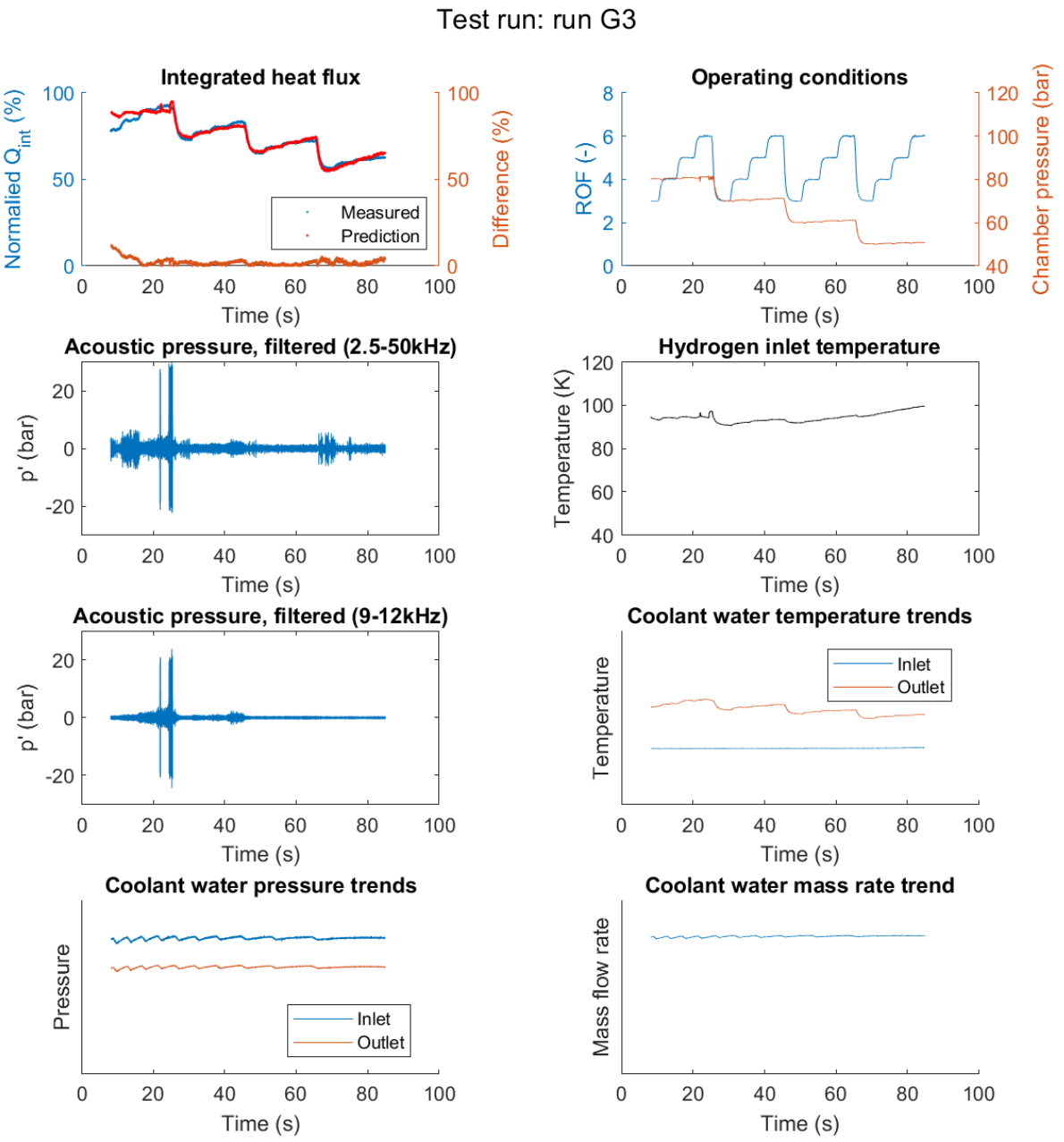

Figure C.7: Test run G3.

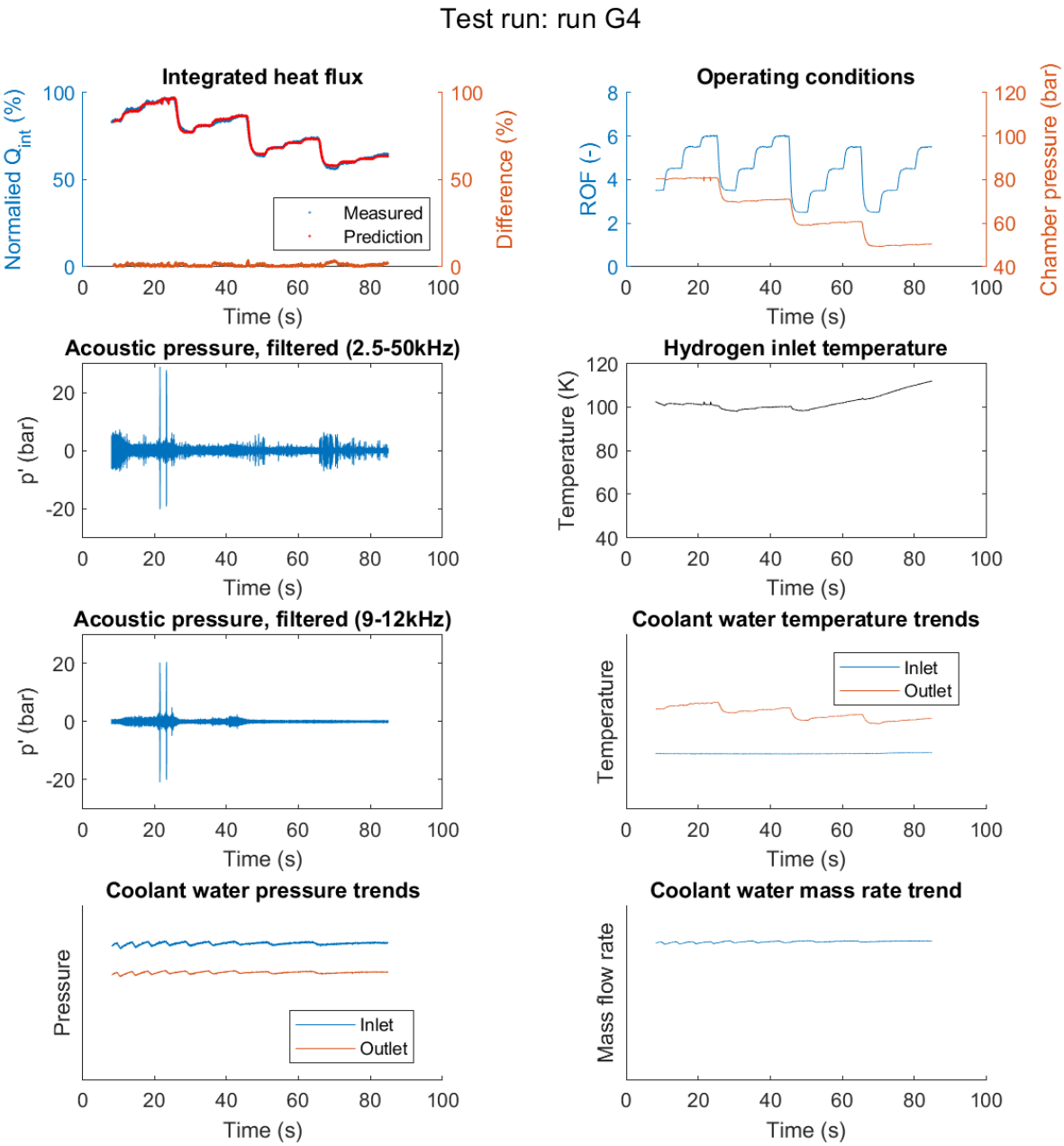

Figure C.8: Test run G4.

Appendix D: Overview of Model Predictions per Test Run.

In this appendix, an overview is given of the results of the models constructed in this thesis work for all experimental test runs performed with combustion chamber BKD of which data has been made available for this research. For each run, these results consist of a comparison of observed and predicted increases in integrated heat flux, the acoustic pressure data together with its calculated amplitude, the operating conditions ROF and chamber pressure so that transients can be observed and an attempted measure fit of the model prediction with the observed changes in integrated heat flux. Test runs are grouped according to similarities in their test sequence and are presented in the following sections.

L1 and L2

Considering test run L1 is the only test run in which large amplitude combustion instabilities occur for longer durations, this is the most representative run for comparison with the model. It can also be seen that the model predicts the observed increase of heat flux in the correct time periods, although the predicted amplitudes are too small. This underprediction however, can be at least partly explained through an underprediction of combustion zone length during stable combustion. This underprediction comes from the assumption that LOX core length can be equalled to the combustion zone length, while in reality the combustion zone could be longer. It should also be noted that an underprediction is logical, as it leaves room for other effects which might occur such as destruction of thermal boundary layers. As for test run L2, there seems to be a large increase in observed heat flux shortly after the combustion instability takes place. Although the model does predict an increase in heat flux, it predicts this earlier than the observed increase and thus there is no match between prediction and observation in the accuracy plot. The other large increase in heat flux which appears to be observed experimentally does not occur during any combustion instabilities, but coincides with large transients in pressure and ROF measurements and are thus not considered for this research.

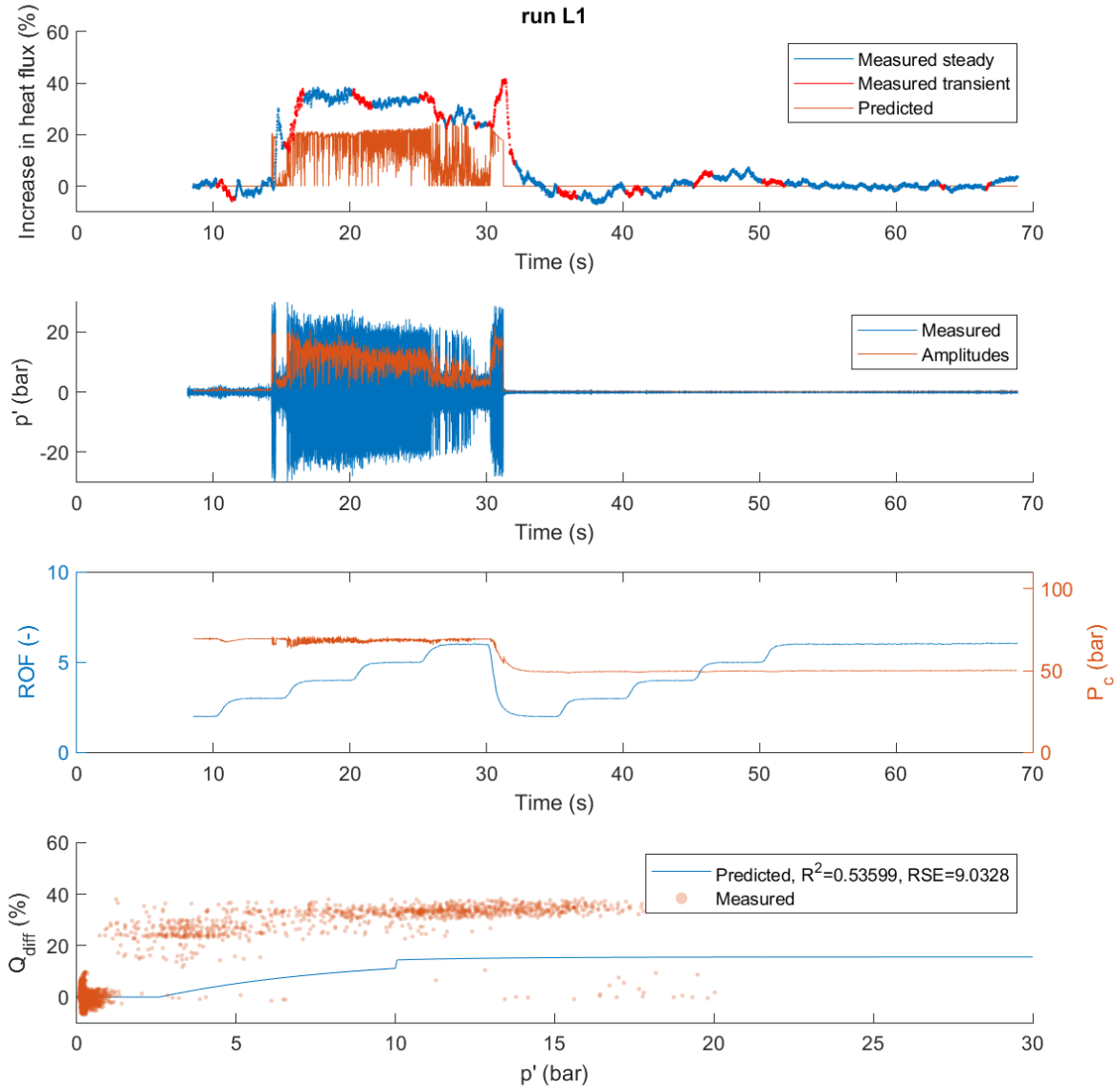

Figure D.1: Model comparison to test run L1.

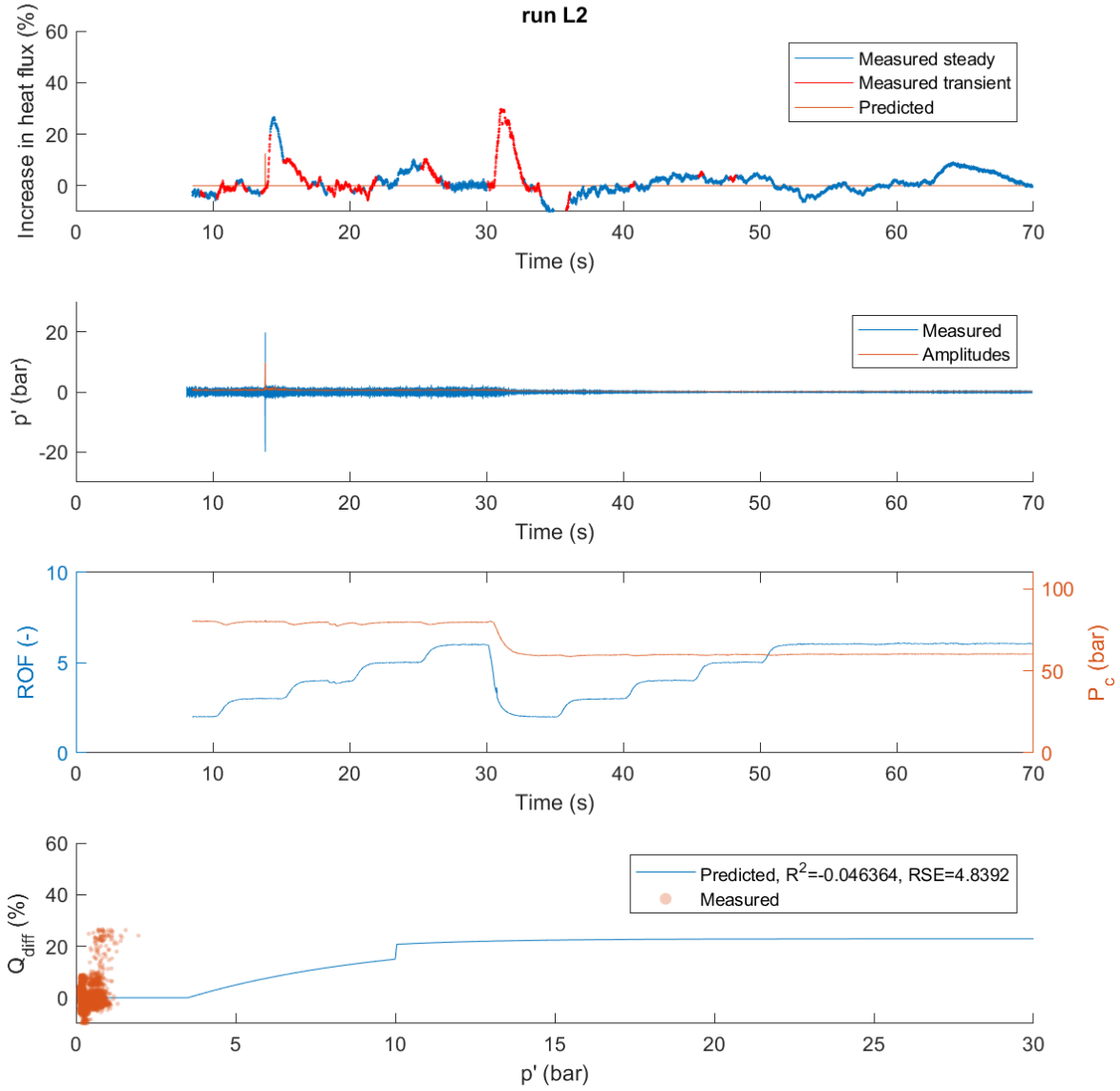

Figure D.2: Model comparison to test run L2.

L3 and L4

In test run L3 there are no combustion instabilities present and also no predicted increase in heat flux. Wherever there are changes in operating conditions however, there does seem to be a slight predicted drop in integrated heat flux, although these drops are not physical but mispredictions in stable integrated heat flux. In test run L3 there are combustion instabilities at the beginning of the test run. However, because of this there seems to be an extended period of mispredicted stable integrated heat flux as shown in Appendix C. As elaborated in Appendix C, this run is excluded from analyses for this reason and thus not considered for further comparison with the model.

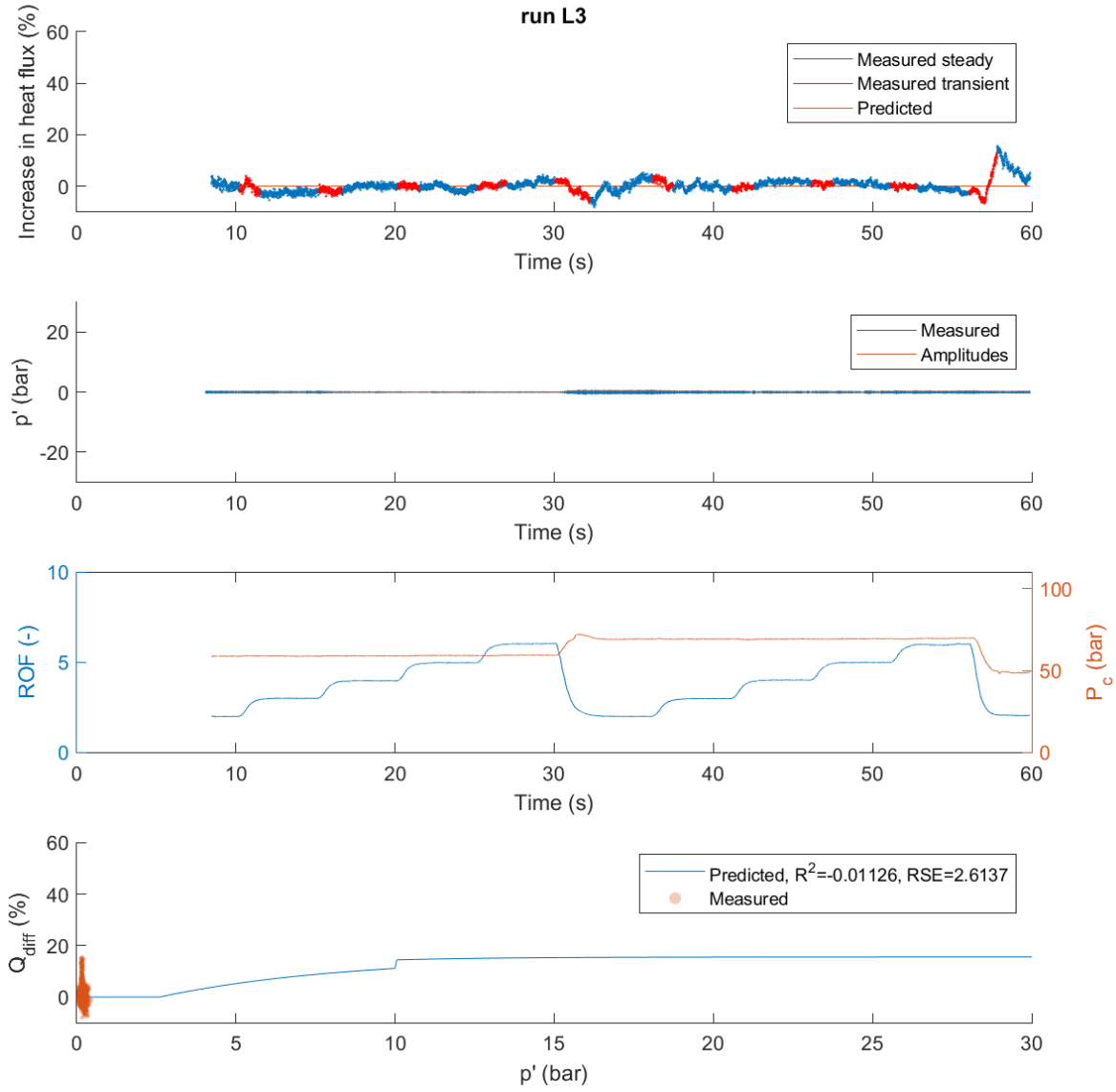

Figure D.3: Model comparison to test run L3.

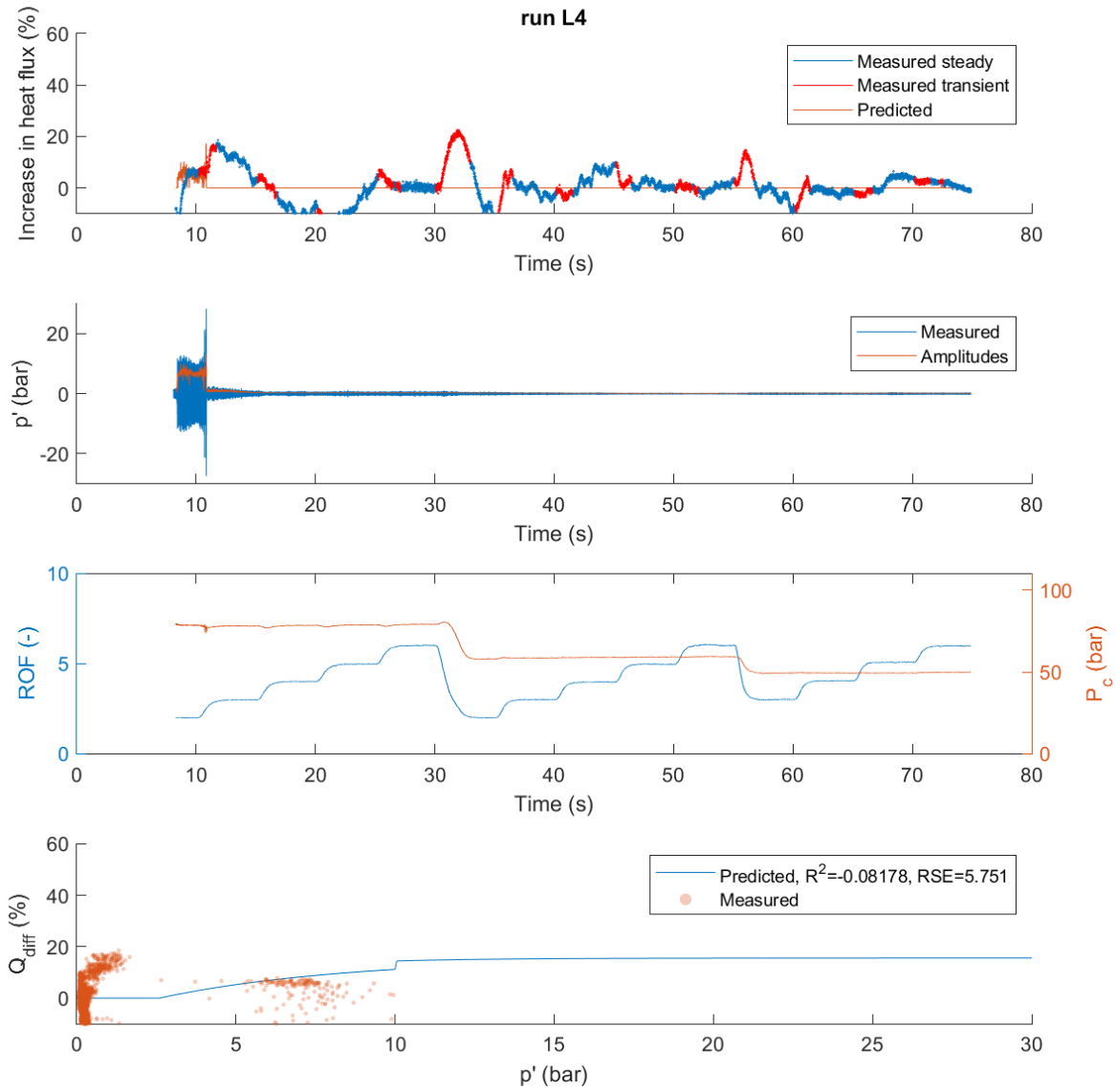

Figure D.4: Model comparison to test run L4.

G1 and G2

When considering test run G1, there is one period of low amplitude combustion instabilities, which corresponds to a prediction of a small increase in integrated heat flux. However, no increase is observed in the experimental data and thus there is no match with the model. Other observed increases in heat flux are again coinciding with large transients in operating conditions and are not considered.

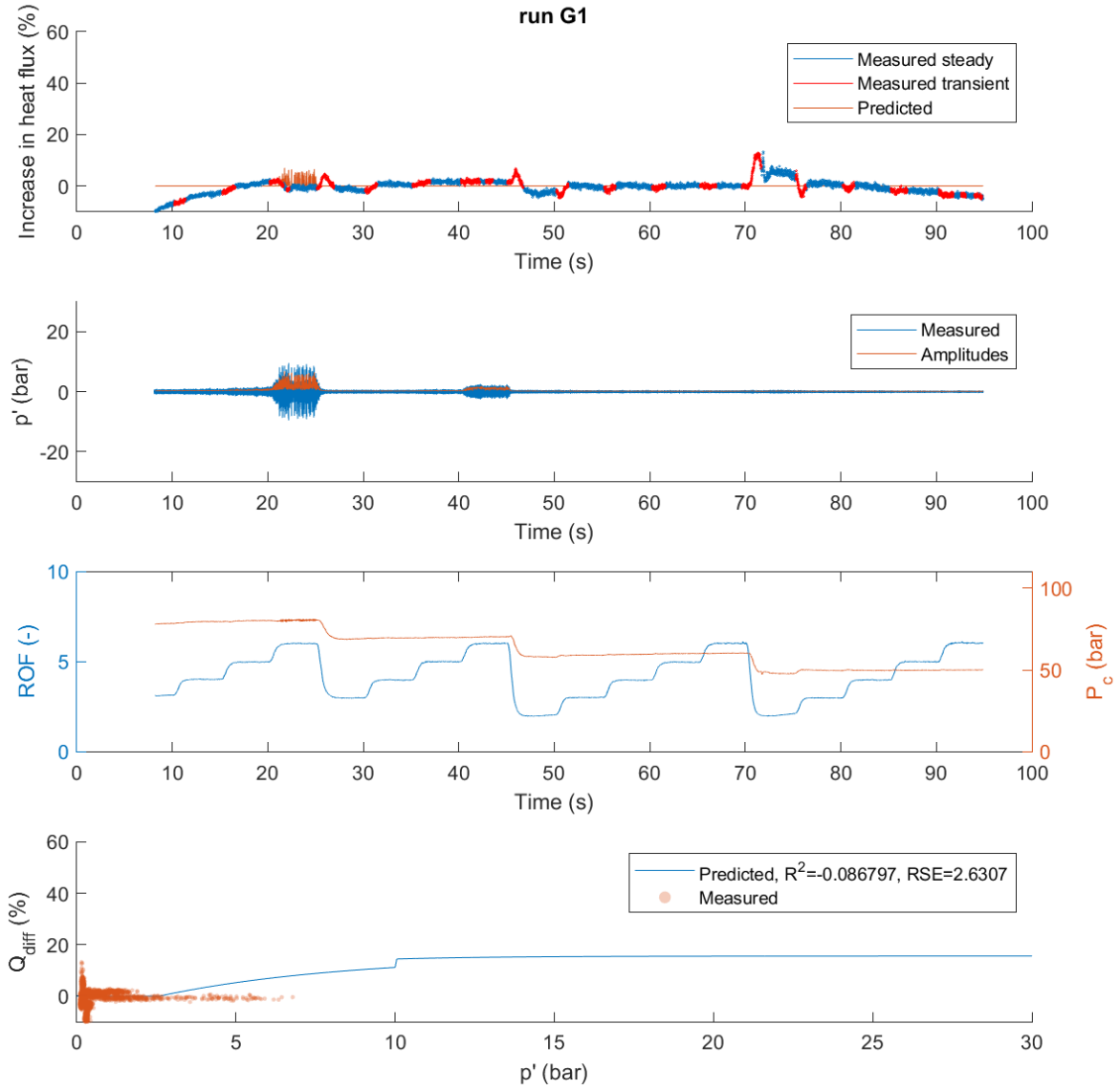

Figure D.5: Model comparison to test run G1.

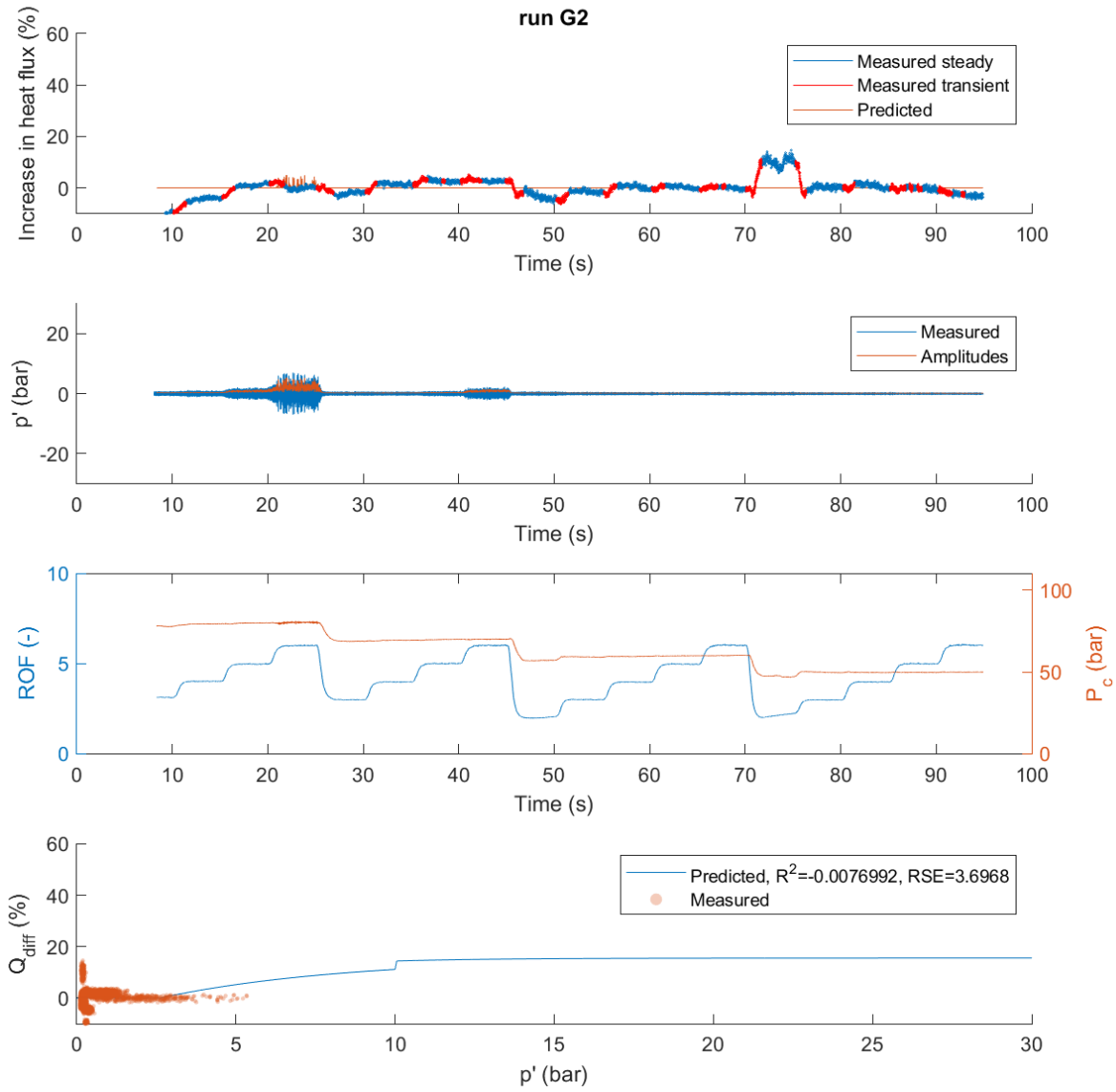

Figure D.6: Model comparison to test run G2.

G3 and G4

For test run G3, there are some large amplitude combustion instabilities, although they only exist for short time periods. For this reason, it is expected that the combustion instabilities did not exist for long enough for heat flux changes to develop in the chamber, but either way no significant changes in heat flux can be observed at periods of large amplitude combustion instabilities. Thus, the model and observations do not match each other. Note that also in this case, observed increases in heat flux occur at the same time as large transients in operating conditions and are thus not considered for comparison. The same explanation applies to test run G4, where the combustion instabilities are of even shorter duration.

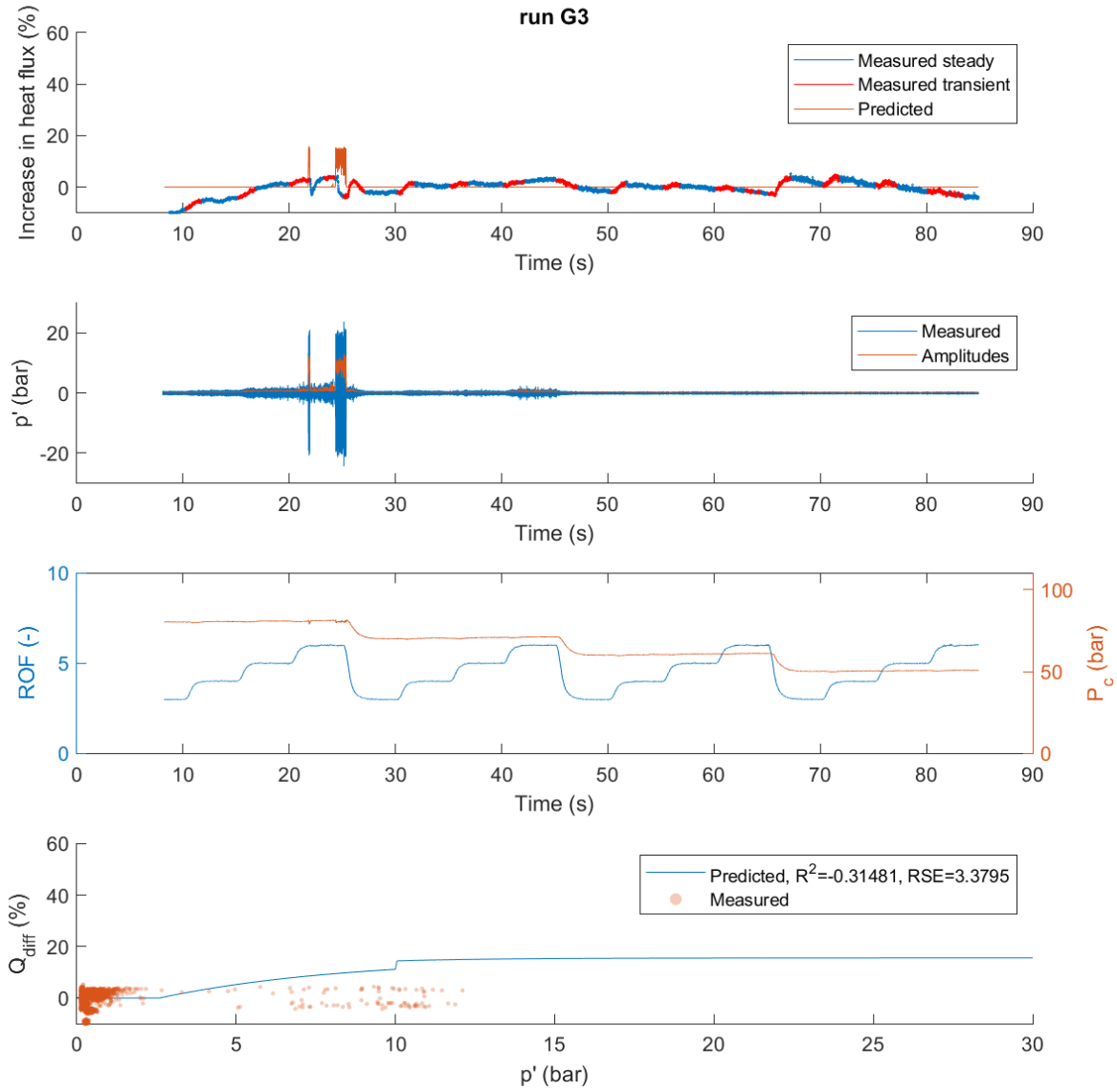

Figure D.7: Model comparison to test run G3.

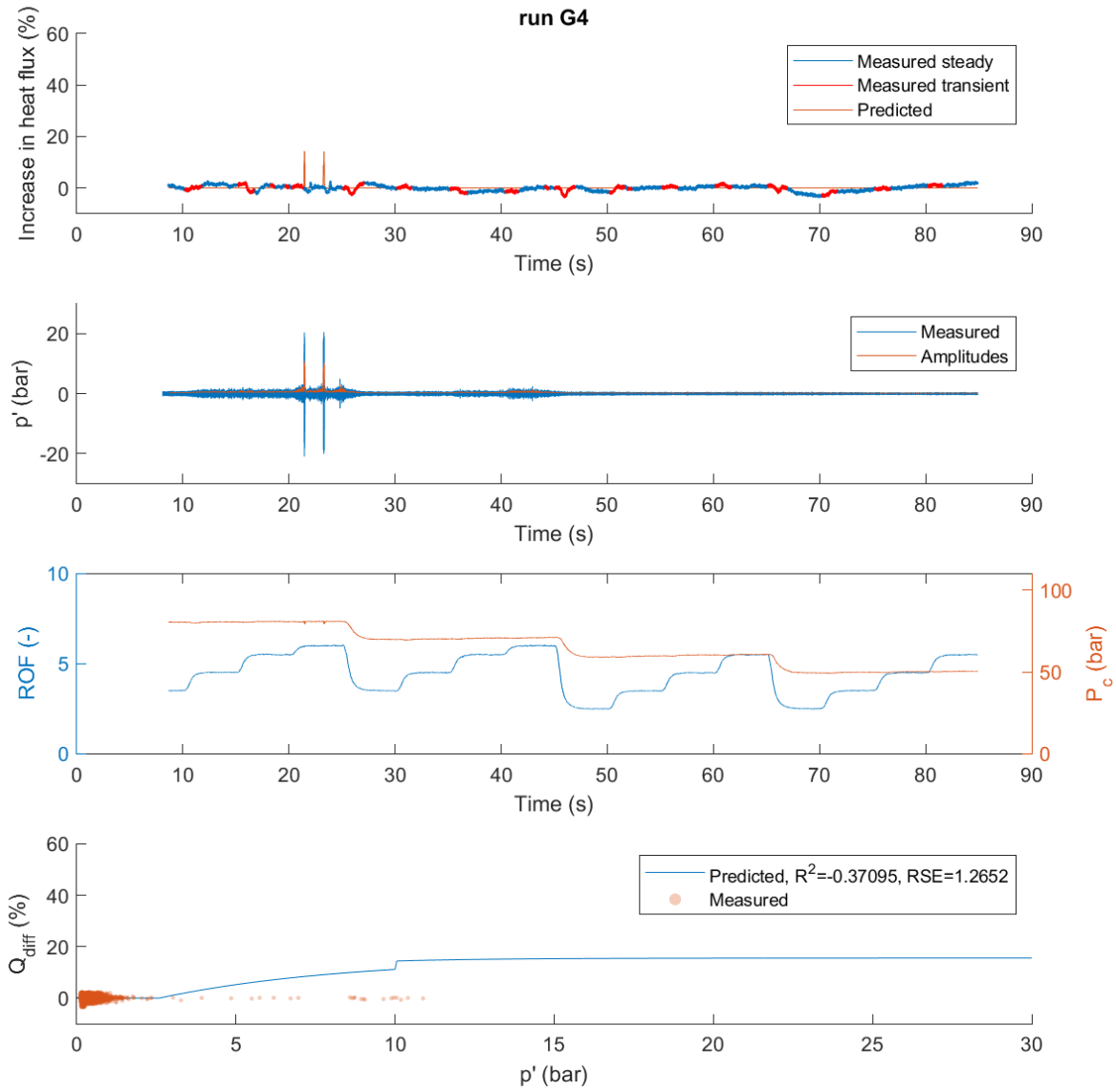

Figure D.8: Model comparison to test run G4.

Appendix E: Overview of Injected Propellant Properties

In this appendix, an overview is given of the trends in injected propellant properties during the test runs. It should be noted that no values are given, rather only the trends with which they change in time, as to provide possibility for verifying calculated heat flux trends without giving up all test data.

L1 and L2

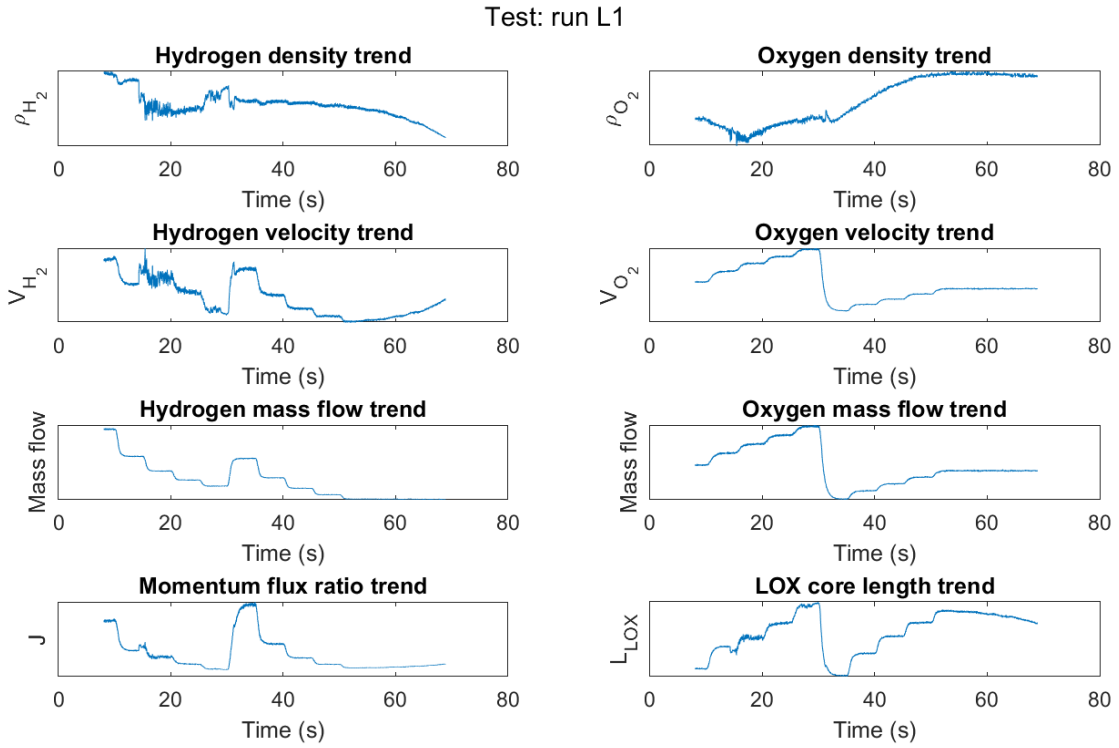

Figure E.1: Trends in injected propellant properties of test run L1.

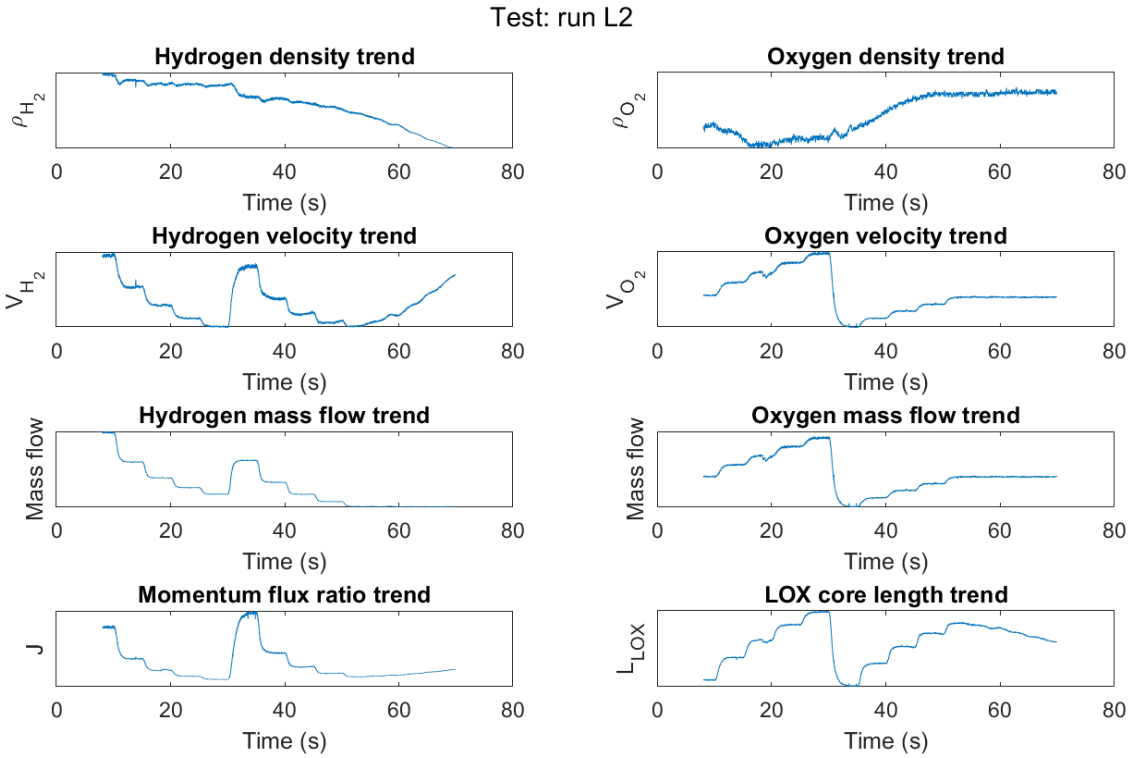

Figure E.2: Trends in injected propellant properties of test run L2.

L3 and L4

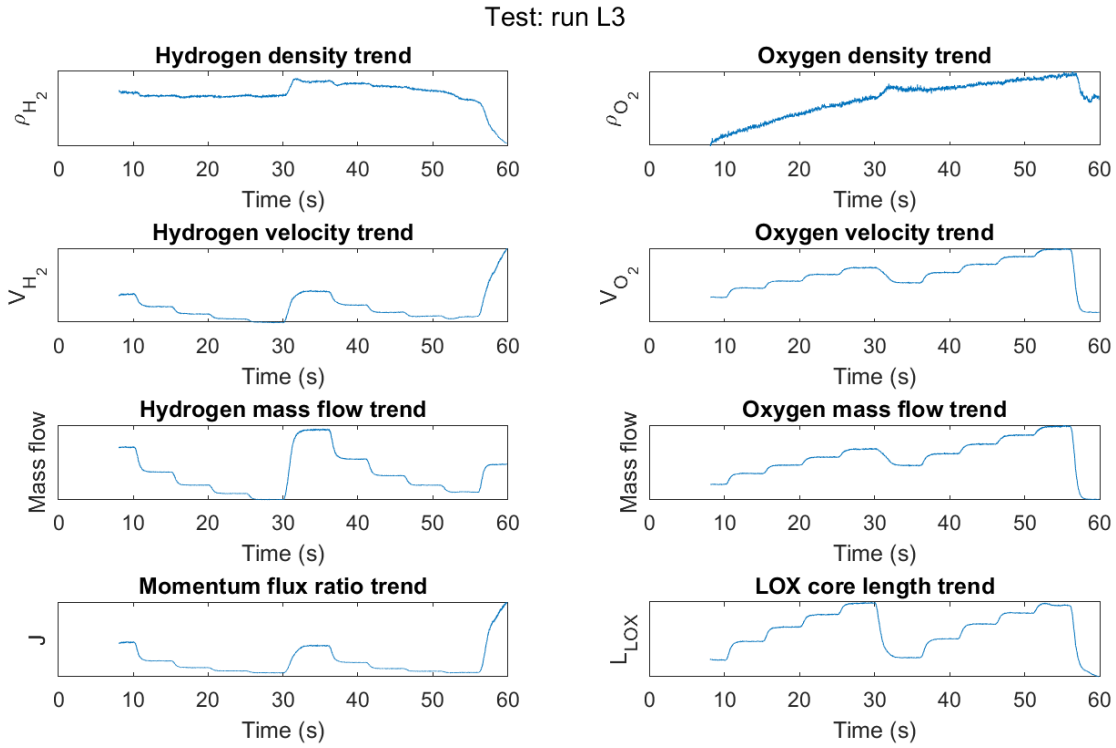

Figure E.3: Trends in injected propellant properties of test run L3.

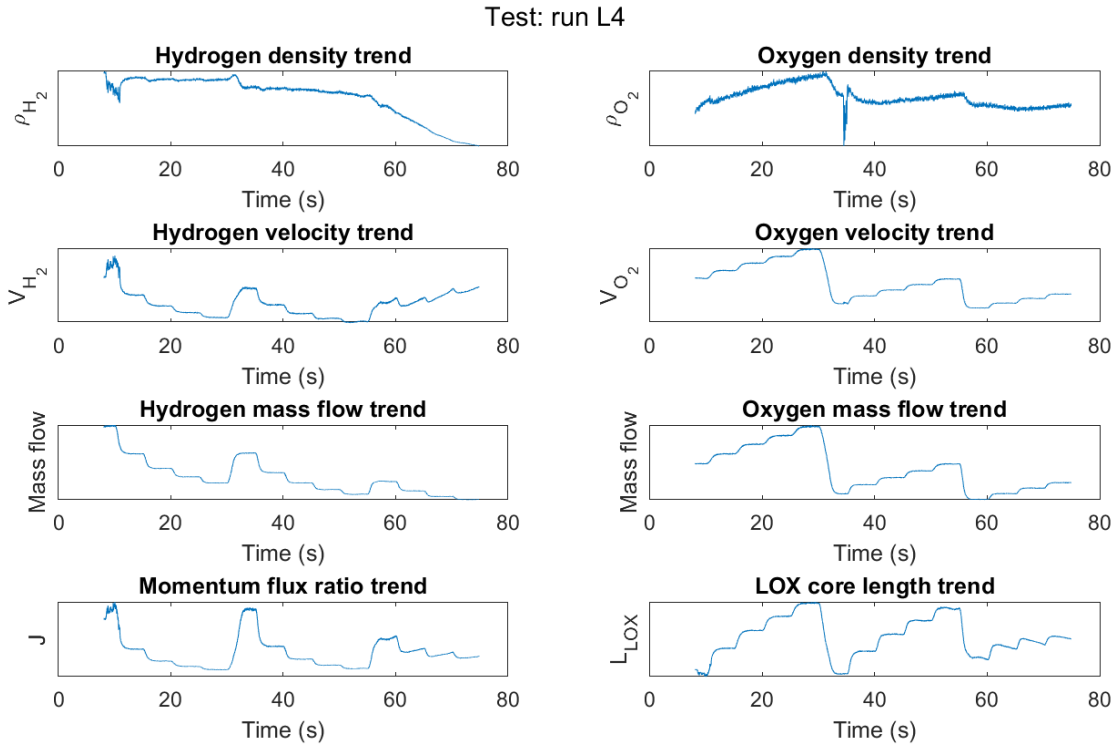

Figure E.4: Trends in injected propellant properties of test run L4.

G1 and G2

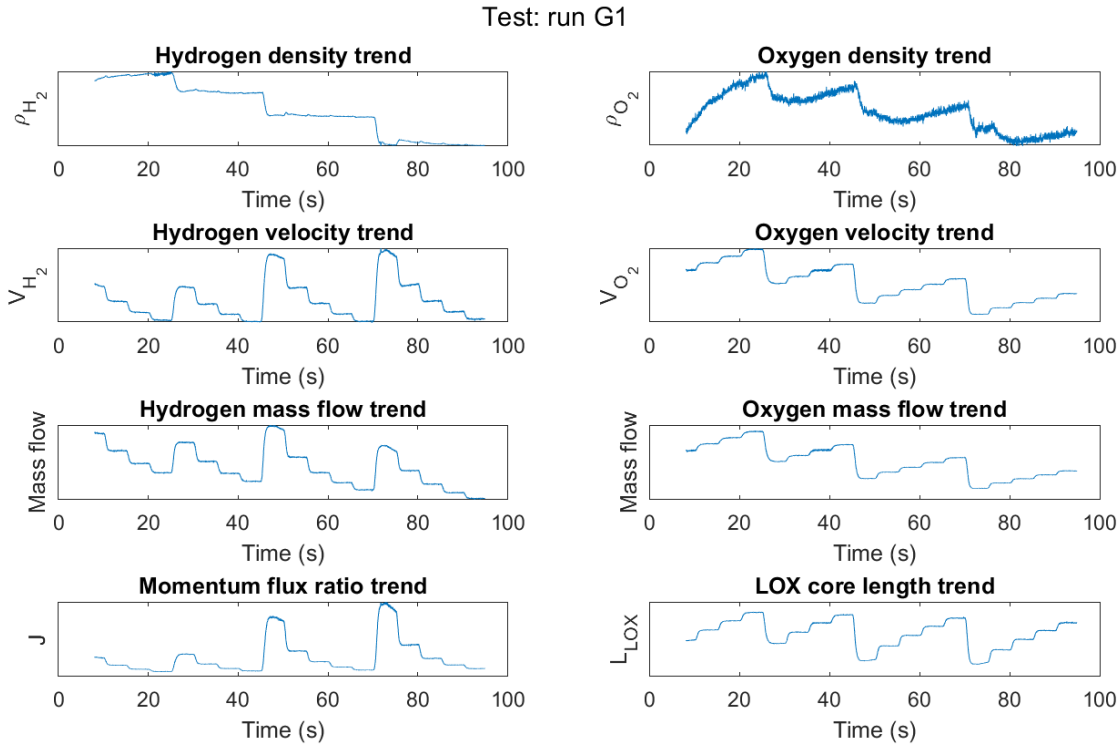

Figure E.5: Trends in injected propellant properties of test run G1.

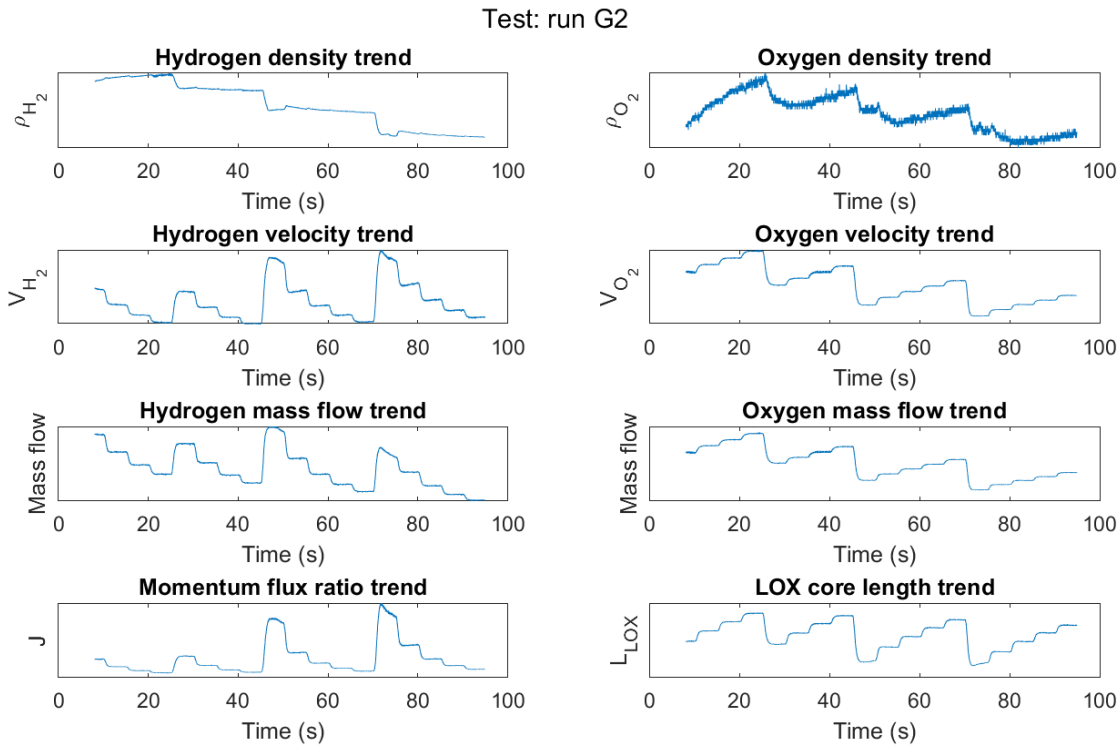

Figure E.6: Trends in injected propellant properties of test run G2.

G3 and G4

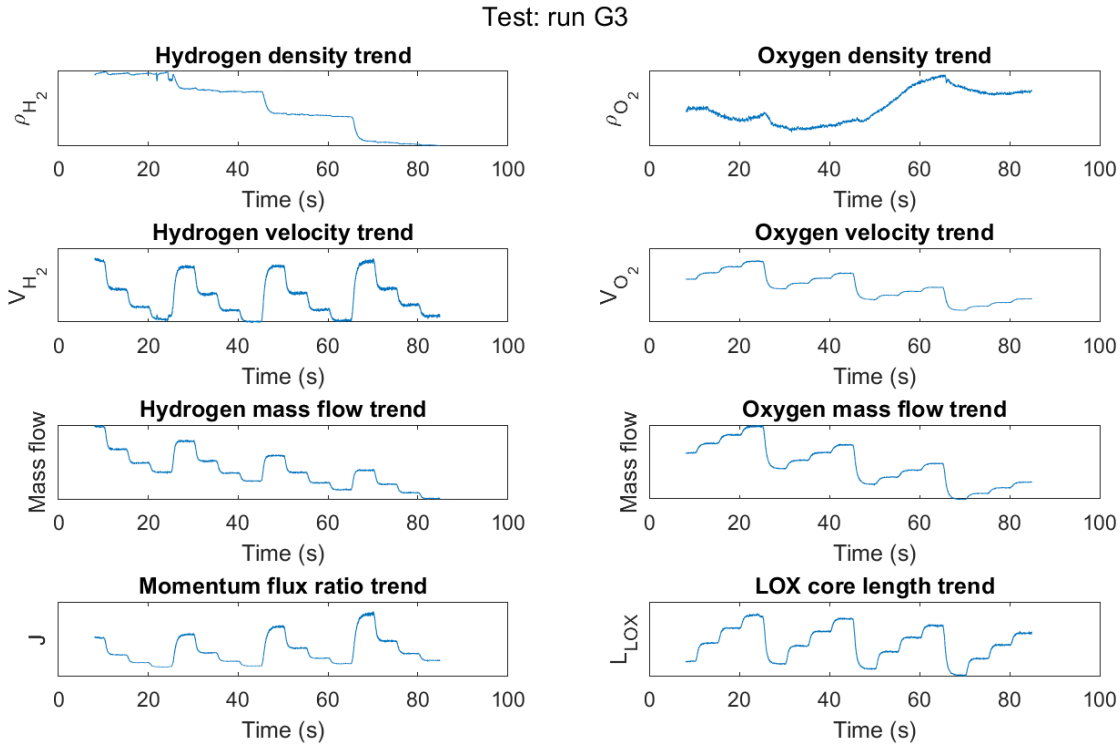

Figure E.7: Trends in injected propellant properties of test run G3.

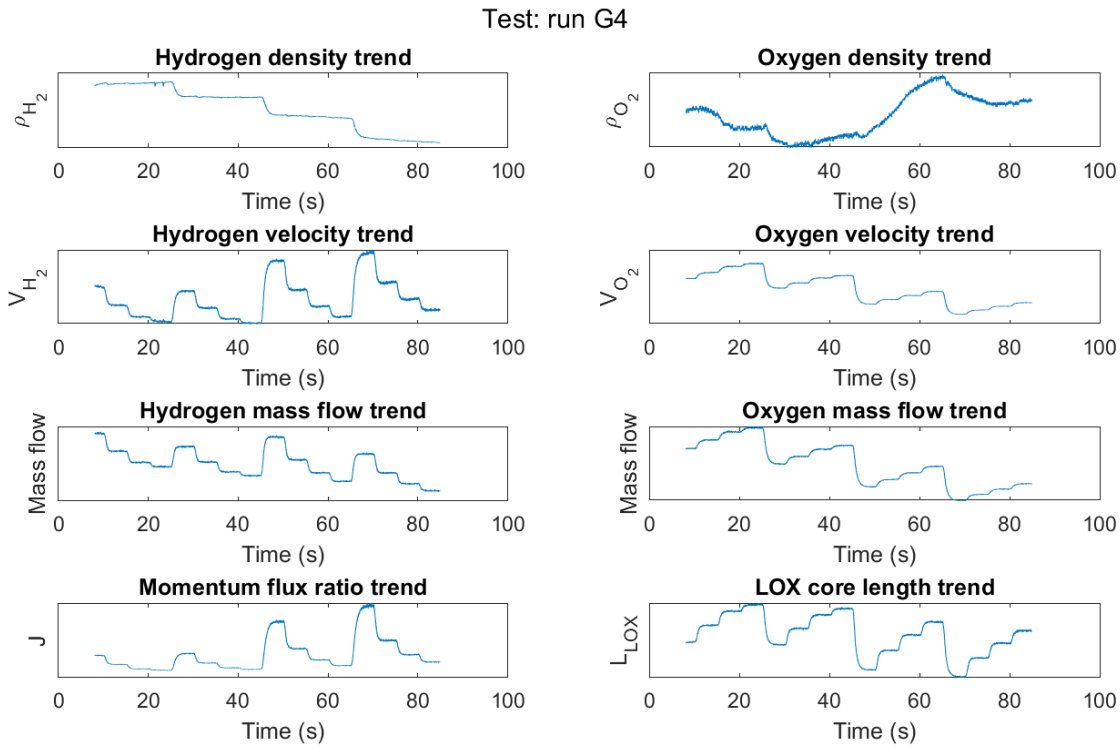

Figure E.8: Trends in injected propellant properties of test run G4.